Large Lepton Asymmetry and the Cosmic QCD Transition

Dissertation

submitted to the

Faculty of Physics,

Bielefeld University

by

Mandy Maria Wygas

December 2018

Supervisor and 1. assessor: Prof. Dr. Dietrich Bödeker
2. assessor: Prof. Dr. Dominik J. Schwarz

Für Anne

Abstract

The lepton asymmetry of the universe is just weakly constraint and might be orders of magnitude larger than the baryon asymmetry. In this thesis, we investigate how a lepton asymmetry influences the cosmic trajectory through the phase diagram of Quantum Chromodynamics (QCD). Therefore, we develop a technique to determine the temperature evolution of chemical potentials during the QCD epoch of the early universe at arbitrary lepton flavor asymmetries. We will rely on an ideal quark gas approximation at high temperatures, $T > 150$ MeV, and a hadron resonance gas model at low temperatures, $T < 250$ MeV. Higher-order perturbative corrections are (partially) included in the ideal quark gas approximation. To interpolate between these approximations, we will for the first time use lattice QCD susceptibilities to properly account for strong interaction effects close to the QCD transition temperature T_{QCD}. We therefore use a Taylor series ansatz of the QCD pressure up to second order in the chemical potentials. With this technique we investigate the impact of equally and unequally distributed lepton flavor asymmetries on the cosmic trajectory. We conclude with an estimate on the reliability of our technique via using a Taylor series of the QCD pressure.

Gedruckt auf alterungsbeständigem Papier °° ISO 9706

Published work

Parts of the methods and results discussed in Chapters 6 and 7 of this thesis have been published under [1]:

> M. M. Wygas, I. M. Oldengott, D. Bödeker and D. J. Schwarz,
> "Cosmic QCD Epoch at Nonvanishing Lepton Asymmetry,"
> *Phys. Rev. Lett.* **121** (2018) 201302,
> `arXiv:1807.10815 [hep-ph]`.

The main work of this publication was done by myself. The results are based on a code first developed by [2], which has been corrected by Dr. Isabel Oldengott and myself. I updated and corrected the particle properties and enlarged the number of included hadron resonances according to the summary tables of the Particle Data Group [3] (see also App. A.4 for a list of the included hadron resonances and their properties). I implemented the possibility of using lattice QCD results in the code and furthermore extended the calculation of the entropy density to nonvanishing chemical potentials. The text was written by myself and afterwards edited by my collaborators.

Contents

I think physicists are the
Peter Pans of the human race.
They never grow up,
and they keep their curiosity.
— Isidor Isaac Rabi

1 Introduction

One of the basic pillars of modern physics is the Standard Model of particle physics (SM) which describes all elementary particles and their fundamental interactions, i.e., the electromagnetic, weak and strong interaction. Only the gravitational interaction is not described within the SM. Even though the SM is remarkably complete and consistent with a tremendous amount of experimental findings, the SM fails to describe one fundamental interaction and there are still some phenomena which cannot be explained within the SM.

The existence and the origin of the matter-antimatter asymmetry in the present universe is one of the biggest unresolved puzzles of particle physics and cosmology. Without the existence of a matter-antimatter asymmetry no matter structures could have formed and the universe would have ended in an annihilation catastrophe resulting in nothing but radiation. However, we experience in our daily life that there is more matter than antimatter, because everything around us is made of matter. The baryon asymmetry, defined as the baryon net number density per entropy density, $b = (\mathrm{n}_B - \mathrm{n}_{\bar{B}})/s$, of the universe is well known and tightly constrained to be $b = (8.71 \pm 0.04) \times 10^{-11}$ [3]. Nevertheless, the SM fails to explain the baryon asymmetry by many orders of magnitude [4] and physics beyond the SM is needed. The lepton asymmetry $l = n_L/s$ is the key parameter to better understand the origin of the matter-antimatter asymmetry. The idea of leptogenesis [5] is to create a lepton asymmetry which due to efficient electroweak sphaleron processes is partially converted to a baryon asymmetry yielding $l = -(51/28)b$ [6]. However, there also exist models that predict a lepton asymmetry today, which is orders of magnitude larger than the baryon asymmetry [7–16].

Observationally, the total lepton asymmetry of the universe $l = \sum_\alpha l_\alpha$, $\alpha \in \{e, \mu, \tau\}$, is only weakly constrained. The charge neutrality of the universe [17] links the asymmetry in the charged leptons to the tiny baryon asymmetry. Thus, a large lepton asymmetry would be manifested in the neutrino asymmetries nowadays. However, neutrinos cannot be detected directly due to their weakly interacting na-

ture.[1] Constraints on the neutrino asymmetry can only be inferred indirectly by measurements and analyses of big bang nucleosynthesis and the cosmic microwave background. They yield $|l| \lesssim 0.012$ [18, 19]. These analyses are, however, blind to individual lepton flavor asymmetries, which are likely to be equilibrated at the times of those cosmological epochs [19–21].

Another important, yet not well understood event in the early universe is the cosmic quantum chromodynamics (QCD) transition[2] from freely propagating quarks and gluons to in hadrons confined ones at $T_{\mathrm{QCD}} = 156.5 \pm 1.5$ MeV at vanishing baryon chemical potential μ_B [22]. For vanishing temperature and large baryon chemical potential effective models of QCD predict a first-order phase transition [23]. This first-order phase transition [24] has to end in a second-order critical endpoint [25, 26] as for high temperatures and low baryon chemical potential it has been shown by lattice QCD calculations that the QCD transition for the SM is an analytic crossover [27, 28]. But due to the infamous sign problem in lattice QCD, calculations for nonvanishing chemical potentials are very difficult [26, 29–31].

The standard cosmic trajectory, i.e., the evolution of the chemical potentials in the early universe through the phase diagram of strongly interacting matter, is commonly assumed to pass T_{QCD} at vanishing baryon chemical potential and to proceed to the order of the nucleon mass at lower temperatures, whereby standard means $l \simeq \mathcal{O}(b)$. For large lepton asymmetries $|l| \gg b$ it has been shown that the baryon and electric charge chemical potential become on the order of the lepton asymmetry $\mu_B \sim \mu_Q \sim lT$ at $T \gtrsim T_{\mathrm{QCD}}$ [2, 32]. Assuming an overall electric charge neutrality and a fixed baryon asymmetry, a lepton asymmetry in the electrically charged leptons induces an electric charge asymmetry in the quark sector and thus quark chemical potentials. Quark chemical potentials induce nonvanishing baryon and electric charge chemical potentials, as quarks carry baryon number and electric charge. Thus, large primordial lepton asymmetries shift the cosmic trajectory to higher electric charge and baryon chemical potential and thus the order of the QCD transition in the early universe might be changed. This could have observable consequences via the production of relics [33–37]. Understanding the impact of a lepton asymmetry on the evolution of the universe at various epochs is therefore of

[1] Additionally, neutrinos represent another example for the incompleteness of the SM. Neutrino masses and oscillations cannot be explained within the SM. Furthermore, it is still unknown if neutrinos are Dirac or Majorana particles. In this thesis, we will assume Dirac neutrinos, such that neutrinos and antineutrinos are distinct particles and a neutrino asymmetry can be defined.

[2] Throughout this thesis, we will refer to a transition as a change from one state of matter to another state of matter irrespective from its kind, i.e., whether it is a true first- or second-order phase transition or an analytic crossover.

crucial importance.

In this thesis we will discuss how the cosmic trajectory through the QCD phase diagram is influenced by the presence of nonvanishing lepton asymmetries. The effect of lepton asymmetries on the evolution of chemical potentials has been first considered for massless particles by [32]. First calculations of the cosmic trajectory in the QCD phase diagram have been performed in [38]. In [2] the evolution of chemical potentials at large lepton asymmetries has been studied in the approximations of an ideal quark gas and of a hadron resonance gas. We extend and advance the approach of [2] in the following way: We will present a novel technique of determining the cosmic trajectory by using lattice QCD results for conserved charge susceptibilities [1]. Thus, for the first time, we are able to properly take into account strong interaction effects close to T_{QCD}. Approximate relations between lepton asymmetries and chemical potentials in terms of susceptibilities have been studied in the context of sterile neutrinos production by [39, 40]. Furthermore, we enlarged the number of hadron resonances used in [2] and we improved the calculation by self-consistently including the effect of nonvanishing particle chemical potentials also in the entropy density.

The thesis is structured as follows: In Chapter 2 we will review some general aspects of cosmological evolution that are important for our work. The thermodynamical basics needed for our technique, i.e., the grand canonical ensemble, thermodynamic variables, particle asymmetries and phase transitions, will be introduced in Chapter 3. Constraints and possible production mechanisms of large lepton asymmetries will be discussed in Chapter 4. Aspects of QCD and in particular the QCD phase diagram will be explained in Chapter 5. The basic of our novel technique, i.e., the Taylor series ansatz of the QCD pressure, will be discussed in Chapter 6. The main idea of our technique and results for the cosmic trajectory at nonvanishing lepton flavor asymmetries will be elaborated on in Chapter 7. In Chapter 8 the applicability range of our technique using a Taylor series ansatz of the QCD pressure is examined in detail.

Throughout the whole thesis natural units and Einstein summation convention are used, i.e., $c = \hbar = k_B = 1$ and repeated indices are summed over, unless otherwise stated.

2 Cosmological Motivation

In this Chapter we will give an overview on aspects of the cosmological evolution that are important for the thematic classification of the work performed in this thesis. We first give a brief overview on the properties of the universe today in Sec. 2.1 and continue with the evolution of the universe in Sec. 2.2. We will conclude with a discussion on interaction rates and maintaining of thermal equilibrium in the early universe in Sec. 2.3 which is a prerequisite for our technique of determining the cosmic trajectory.

2.1 The Universe today

The most convenient model to describe the evolution of the universe is the ΛCDM (Lambda Cold Dark Matter) model of cosmology. It describes the evolution of an expanding universe with cold dark matter (CDM), i.e., particles which were nonrelativistic at the time of decoupling and at most interact weakly with the SM particles, a cosmological constant Λ which is associated with dark energy (DE), and zero spatial curvature $k = 0$.[3] The present universe is homogeneous and isotropic at large spatial scales, which forms the *cosmological principle*. This principle guarantees that observations from Earth are representative for the whole universe and thus can be used to test cosmological models.

The expansion rate of the universe is described by the Hubble parameter H, which is defined through the Friedmann equation

$$H^2(t) \equiv \left(\frac{\dot{a}(t)}{a(t)}\right)^2 = \frac{8\pi}{3} G\rho - \frac{k}{a^2} \ , \tag{2.1}$$

with the gravitational constant G, which is related to the Planck mass via $M_{Pl} = G^{-1/2} = 1.2 \times 10^{19}$ GeV [3]. The distance between two far away objects is proportional to the scale factor $a(t)$ and $\dot{a}(t) = \mathrm{d}a(t)/\mathrm{d}t$ denotes the derivative with respect to time. The total energy density of the universe can be parametrized by $\rho = \rho_m + \rho_{\mathrm{rad}} + \rho_\Lambda$, with the energy densities of nonrelativistic matter, relativistic matter (radiation), and cosmological constant (dark energy), respectively. The contribution due to spatial curvature $k = 0, \pm 1$ can be defined as $-k/a^2 = (8\pi G/3)\rho_k$.

[3] There exists of course a variety of different other models like, e.g., modified gravity models to describe the evolution of the universe or Massive Compact Halo Objects (MACHOs) to describe DM. However, they seem to be disfavored by observations of the Bullet Cluster [41].

With the Planck mission the present values of the cosmological parameters can be determined by measurements of the cosmic microwave background (CMB) temperature and polarization anisotropies. The present value of the Hubble parameter is $H_0 = 100h\frac{\text{km}}{\text{s·Mpc}} = (67.4 \pm 0.5)\frac{\text{km}}{\text{s·Mpc}}$ [42], with the scale factor for the Hubble expansion rate h and the subscript 0 of a quantity indicating its present value. The age of the universe can be estimated by the inverse of the Hubble parameter: $H_0^{-1} \approx 1.38 \times 10^{10}$ yrs. The present energy density, also called critical energy density, is given by [3]

$$\rho_c = \frac{3H_0^2}{8\pi G} \approx 4.8 \times 10^{-6} \frac{\text{GeV}}{\text{cm}^3} \ . \tag{2.2}$$

The relative contributions of the different constituents to the energy density are parametrized by the density parameters $\Omega_i = \rho_i/\rho_c$. Observations yield the present numerical values [42]:

$$\begin{aligned} \Omega_m &= 0.3153 \pm 0.0073 \ , \\ \Omega_{\text{rad}} &= (5.38 \pm 0.15) \times 10^{-5} \ , \\ \Omega_\Lambda &= 0.6847 \pm 0.0073 \ , \\ \Omega_k &= 0.001 \pm 0.002 \ . \end{aligned} \tag{2.3}$$

Thus, the impact of relativistic particles and the spatial curvature is negligible today and we will set $k = 0$ in the following. The nonrelativistic matter can be subdivided into the sum of baryons, i.e., ordinary matter, and dark matter, $\Omega_m = \Omega_b + \Omega_{\text{DM}}$. The numerical values today are given by [42]

$$\Omega_b h^2 = 0.00224 \pm 0.0001, \quad \Omega_{\text{DM}} h^2 = 0.120 \pm 0.001 \ . \tag{2.4}$$

The origin and content of dark energy and dark matter, which constitute the main part of the energy content of the universe today, is one of the major puzzles in cosmology and particle physics. As they cannot be described within the framework of the SM and general relativity, this requires physics beyond the SM. Several models have been developed to describe dark energy and dark matter (cf. e.g. the reviews in [3]).

The baryon density parameter can be related to the baryon abundance, i.e., the ratio of baryon net number density to photon number density [43]:

$$\begin{aligned} \eta_B \equiv \frac{n_B}{n_\gamma} &= 273.8 \times 10^{-10} \Omega_b h^2 \\ &= (6.133 \pm 0.027) \times 10^{-10} \ . \end{aligned} \tag{2.5}$$

The specific baryon asymmetry, i.e., the ratio of the baryon asymmetry to the entropy density s, can be obtained as (cf. Sec. 3.3)[4]

$$b = \frac{n_B}{s} = \eta_B \frac{n_\gamma}{s} = (8.71 \pm 0.04) \times 10^{-11} \ . \tag{2.6}$$

In absence of baryon number violating interactions, the baryon asymmetry b in the early universe was of the same order of magnitude as now. Thus, models of cosmological evolution can be tested by their predictions of b. Additionally, even though the size of the baryon asymmetry cannot be explained within the SM, it is one of the most important parameters of cosmology. Without any baryon asymmetry in the early universe no structure formation would have been possible as all particles and antiparticle would have annihilated.

2.2 Evolution of the Universe

The evolution of the expanding universe can be described within the *Hot Big Bang Theory* which is depicted in Fig. 2.1. If we extrapolate back the observed properties of the universe, there was a singularity, which is referred to as Big Bang. However, Hot Big Bang Theory has its problems. Some are due to the very special initial conditions which are needed. They are: why is the universe as large, warm, spatially flat, homogeneous and isotropic as it is and why is the entropy that large? One elegant solution is the inflationary scenario. The idea is that the Big Bang is followed by an epoch of exponential expansion (*inflation*). So, initially small and causally disconnected regions inflated to very large size, which also may be orders of magnitude larger than the size of the observable part of the universe. This epoch would then be followed by post-inflationary reheating, where the energy of the inflaton field is transferred to energy of conventional matter. Then the universe heated up and the *radiation dominated era* of cosmological expansion started, which can be probed directly.

If Grand Unification, i.e., the unification of electromagnetic, weak, and strong force, is realized in nature and if such temperatures existed in the early universe, then there was the corresponding phase transition at $T_{\mathrm{GUT}} \sim 10^{16}$ GeV. But it could also be possible that the maximum temperature of the universe was below T_{GUT} and the Grand Unification phase did not exist. This is in fact the case in some models of inflation, where the reheating temperature is below T_{GUT} (cf. e.g. [44]).

[4] As a standard scenario and for simplicity here the contribution of chemical potentials to the entropy density is neglected and $s \cong 7.04 n_\gamma$ after electron-positron annihilation is used (cf. Sec. 3.3).

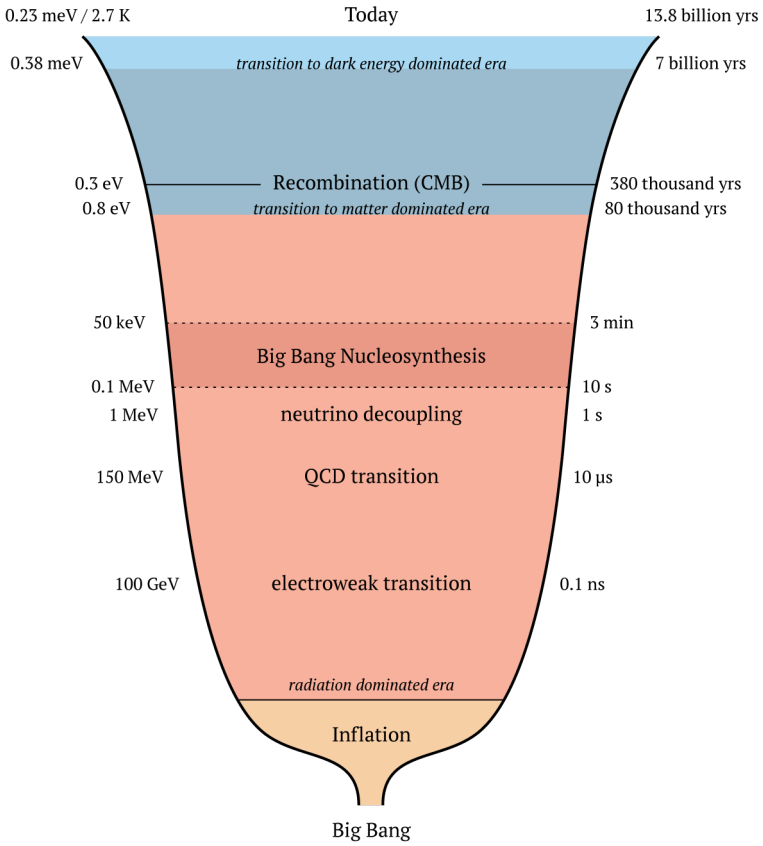

Fig. 2.1: Stages of the evolution of the universe (inspired by [44]).

At about $T_{\mathrm{EW}} \sim 100$ GeV the *electroweak transition* takes place and results in the present phase of broken electroweak symmetry, Higgs condensate and massive W- and Z-bosons. Lattice results show that the electroweak transition in the SM is an analytic crossover and no real phase transition [45–48]. At these temperatures all particles propagate freely in the cosmic plasma. The subsequent *QCD transition* (or smooth crossover) is the transition from freely propagating quarks and gluons to hadronic matter, where they are confined in colorless bound states. The transition temperature is determined by the energy scale of strong interactions and is about $T_{\mathrm{QCD}} \sim 150$ MeV. A very important consequence of this confinement is the huge change in the effective relativistic degrees of freedom $g_{*s}(T)$, (cf. Sec. 7.4 and [49]). As $g_{*s}(T)$ enters the equation of state, i.e., the fundamental relationship among thermodynamic parameters of a system in thermal equilibrium, it influences the expansion rate of the universe by changing the energy density. The nature of this transition, whether it is of first or second order or if it is a smooth crossover, is of great cosmological interest, as local inhomogeneities might be produced and be detectable today.

Matter effects suppress neutrino flavor oscillations in the early universe until $T_{\rm osc} \sim 10$ MeV. At $T \sim 1$ MeV *neutrinos decouple* from the cosmic plasma and propagate freely through the universe (cf. Sec. 2.3). After decoupling the neutrinos are not in thermal contact with the surrounding plasma. When the temperature drops below the mass of the electron, electrons and positrons annihilate and their energy density is transferred to the photons and the effective relativistic degrees of freedom change. This yields the neutrino temperature today $T_\nu = (4/11)^{1/3} T_\gamma$. Thus, there also exists a *Cosmic Neutrino Background* ($C\nu B$) with $T_\nu = 1.9$ K, which in principle could be measured today, but is out of reach with current experimental possibilities.

The neutrino density, or to be more specific, the effective number of neutrino species $N_{\rm eff}$ in the early universe affects the expansion rate through its contribution to the total energy density and also affects the proton-to-neutron ratio (cf. Sec. 4.1). Thus, $N_{\rm eff}$ is an important parameter for the following phase of *Big Bang Nucleosynthesis* (BBN). The onset of BBN is roughly determined by the scale of the binding energies in nuclei ($1 - 10$ MeV) but is delayed by high energetic photon interactions to $T \sim 0.1$ MeV. Before BBN protons and neutrons were free in the cosmic plasma, during BBN neutrons and protons were captured into nuclei. As a result, light nuclei up to lithium-7 were formed in the primordial plasma. Heavier elements were not synthesized until stellar evolution. The BBN epoch lasted from temperatures $T_{\rm BBN} \sim 50$ keV $- 100$ keV and it is the earliest epoch studied directly so far [50].

Going down in temperature, shortly before recombination at about $T_{\rm rm} \sim 0.8$ eV is the *transition from the radiation to matter dominated era* of cosmological expansion. During *Recombination* at $T_r \sim 0.3$ eV free electrons and nuclei combined to form neutral atoms, mainly hydrogen. Before recombination photons scattered off free electrons in the baryon-electron-photon plasma and afterwards the ordinary matter was in the state of a neutral gas, which was transparent to photons and they decoupled. The relic photons provide a snapshot – the *cosmic microwave background* – of the universe at this time. The CMB shows a very high degree of isotropy besides small temperature fluctuations, which mirrors that the universe was highly homogeneous at recombination. These small CMB perturbations are a result from quantum fluctuations of the inflaton. These inflaton perturbations led to structure formation: first stars, then galaxies and clusters of galaxies.

The effect of lepton asymmetries on BBN and the CMB and the resulting constraints on primordial lepton asymmetries will be discussed in detail in Sec. 4.1.

At about $T \sim 0.38$ meV the *transition from the matter to dark energy dominated* era, i.e., to the accelerated expansion of the universe, occurred.

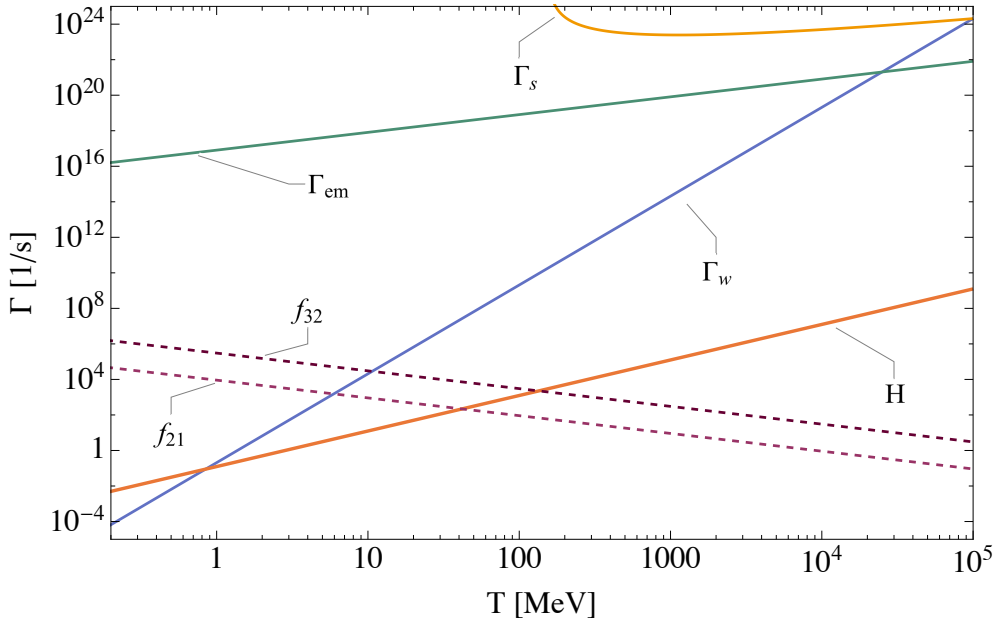

Fig. 2.2: Hubble rate H and weak (Γ_w), electromagnetic (Γ_{em}), and strong (Γ_s) interaction rates for relativistic particles as functions of the temperature of the early universe. Γ_s is plotted for the relativistic quark-gluon plasma at constant $n_f = 4$. Also shown are the neutrino oscillation frequencies f_{21} and f_{32}. Adapted from [33].

2.3 Interaction Rates

For this thesis, it is of great interest at which times or temperatures during the evolution of the universe different particle interactions are in thermal, i.e., in kinetic and chemical equilibrium (cf. Sec. 3.2), and when they fall out of equilibrium. As long as particle interactions occur faster than the Hubble time $t_H = 1/H$ they stay in equilibrium. We will show, in general thermal equilibrium is a good approximation for particle interactions in the early universe.

For a rough estimation of the order of the typical interaction rates and the sake of simplicity, we consider only massless, relativistic particles in the early universe. The Hubble rate in the relativistic matter dominated epoch ($T \gtrsim 0.8$ eV) is according to the Friedmann equation given by

$$H = \frac{T^2}{M_{\mathrm{Pl}^*}} \simeq 1.66\sqrt{g_{*s}}\frac{T^2}{M_{\mathrm{Pl}}} \sim \frac{T^2}{M_{\mathrm{Pl}}} \,, \tag{2.7}$$

with the effective Planck mass $M_{\mathrm{Pl}^*} = \sqrt{\frac{90}{8\pi^3 g_{*s}}} M_{\mathrm{Pl}} \approx \frac{0.6}{\sqrt{g_{*s}}} M_{\mathrm{Pl}}$.

Approximating weak interactions by Fermi theory, which is a good approximation at low temperatures and breaks down at $T \gtrsim m_W/3$, with the W-boson mass m_W,

we get for the order of the weak interaction rate

$$\Gamma_w \sim G_F^2 T^5 \ , \tag{2.8}$$

with the Fermi coupling constant $G_F = 1.1663787(6) \times 10^{-5}$ GeV^{-2} [3].

The order of the electromagnetic interaction rate is given by

$$\Gamma_{\rm em} \sim \alpha_{\rm em}^2 T \ , \tag{2.9}$$

with $\alpha_{\rm em} = e^2/(4\pi)$ the fine-structure constant, while the strong interaction rate is roughly given by

$$\Gamma_s \sim \alpha_s^2(T) T \ . \tag{2.10}$$

The running strong coupling constant $\alpha_s(T)$ in perturbative QCD (pQCD), i.e., considering a quark-gluon plasma, can be determined according to the renormalization group equation (RGE)

$$\mu_R^2 \frac{{\rm d}\alpha_s}{{\rm d}\mu_R} = \beta(\alpha_s) = -\left(b_0 \alpha_s^2 + b_1 \alpha_s^3 + \dots\right) \ , \tag{2.11}$$

with μ_R the unphysical renormalization scale. $b_0 = (33 - 2n_f)/(12\pi)$, with n_f the number of light quark flavors with $m_q \ll \mu_R$, is referred to as the 1-loop β-function coefficient, b_1 is the 2-loop β-function coefficient, and so on (for more details see the review on *Quantum Chromodynamics* in [3]). At 1-loop the RGE can be solved analytically:

$$\alpha_s(Q^2) = \frac{\alpha_s(\mu_R^2)}{1 + b_0 \alpha_s(\mu_R^2) \ln\left(\frac{Q^2}{\mu_R^2}\right)} \ . \tag{2.12}$$

Experimentally the strong coupling constant is determined at fixed energy scale, usually the Z-boson mass m_Z. The current world average value is $\alpha_s(m_Z^2) = 0.1181 \pm 0.0011$ [3]. We used this value and Eq. (2.12) to get a rough estimate for the behavior of the strong interaction rate.

In Fig. 2.2 the evolution of these interaction rates is depicted. We see that thermal equilibrium holds for relativistic SM particles until $T \sim 1$ MeV when the weak interaction rate drops below the Hubble rate and neutrinos decouple.

For comparison, in Fig. 2.2 we also show the neutrino oscillation frequencies

$$f_{ij} \sim \frac{\Delta m_{ij}^2}{4\pi T} \ , \tag{2.13}$$

with $\Delta m_{ij}^2 \equiv (m_i^2 - m_j^2)$ and the numerical values $\Delta m_{21}^2 = (7.53 \pm 0.18) \times 10^{-5}$ eV^2 and $\Delta m_{32}^2 = (2.51 \pm 0.01) \times 10^{-3}$ eV^2 (normal mass ordering) [3]. We see that neutrino oscillations are suppressed until $T_{\rm osc} \sim 10$ MeV due to faster weak interactions.

3 Thermodynamics

Thermodynamics addresses macroscopic properties of macroscopic systems and transitions between equilibrium states. The work demonstrated in this thesis is build on thermodynamic principles. For this reason, we will elaborate on the significant thermodynamic concepts used throughout this thesis and their application to the physics of the early universe. We will introduce the grand canonical ensemble and its applicability to the early universe in Sec. 3.1. In Sec. 3.2 we will discuss thermodynamic variables and their dependence on chemical potentials in detail. We will give definitions on the particle asymmetries in the early universe in Sec. 3.3. Then in Sec. 3.4 we will shortly introduce the basic behavior of thermodynamic variables at phase transitions, which will be important for this thesis.

3.1 Grand Canonical Ensemble

Statistical mechanics describes physical properties of systems which consist of numerous particles, like gases, fluids, and solids. It relates microscopic particle properties to the macroscopic description of a system, i.e., averaged characteristics: temperature, pressure, total energy, heat capacity, conductivity, susceptibilities, etc. The grand canonical ensemble is used to describe an ensemble of particles which are in thermal equilibrium with a large reservoir or itself if the system is large enough. The thermodynamic variables of the grand canonical potential are chemical potential μ, temperature T, and volume V. The chemical potential is the energy needed for adding a particle to the equilibrated system.

As already mentioned, thermal equilibrium is a good approximation for particles in the early universe until $T \simeq 1$ MeV, see Fig. 2.2. Therefore, we can use the grand canonical ensemble to describe conserved charges and their fluctuations in the early universe. The corresponding partition function reads

$$Z = \exp\left(-\frac{\Omega}{T}\right) = \mathrm{Tr}\left\{ \exp\left[\beta\left(\sum_a \mu_a N_a - \mathcal{H}\right)\right]\right\}, \tag{3.1}$$

with Ω the grand canonical potential, N_a the conserved net charges with corresponding chemical potentials μ_a, $\mathcal{H}$ the Hamiltonian describing the SM particles and their interactions conserving N_a, and $\beta = 1/T$. For temperatures below the electroweak transition $T_{\mathrm{EW}} \sim 100$ GeV and above neutrino oscillations $T_{\mathrm{osc}} \sim 10$ MeV no B and L violating processes in the SM have been observed so far. Thus, the Hamiltonian $\mathcal{H}$ in the partition function is the full SM Hamiltonian $\mathcal{H}_{\mathrm{SM}}$.

3.2 Thermodynamic Variables

Particle Number, Energy, and Pressure

The distribution function of an ideal gas is defined as a density function in the phase space of the corresponding particle. Because of the homogeneity and isotropy of the universe, the distribution function of a particle in the universe cannot be a function of space $\mathbf{r}$ or the direction of the momentum $\mathbf{p}$. Thus, it is of the form

$$f = f(|\mathbf{p}|, t) \ . \tag{3.2}$$

Considering particle masses m and degrees of freedom g, one can derive the following quantities:

$$\text{number density} \quad \mathrm{n} = g \int \frac{\mathrm{d}^3\mathbf{p}}{(2\pi)^3} f(|\mathbf{p}|, t) \ , \tag{3.3}$$

$$\text{energy density} \quad \epsilon = g \int \frac{\mathrm{d}^3\mathbf{p}}{(2\pi)^3} \sqrt{|\mathbf{p}|^2 + m^2} f(|\mathbf{p}|, t) \ , \tag{3.4}$$

$$\text{pressure} \quad p = \frac{1}{3} g \int \frac{\mathrm{d}^3\mathbf{p}}{(2\pi)^3} \frac{|\mathbf{p}|^2}{\sqrt{|\mathbf{p}|^2 + m^2}} f(|\mathbf{p}|, t) \ , \tag{3.5}$$

with the energy of a particle $E = \sqrt{|\mathbf{p}|^2 + m^2}$ according to special relativity. The particle degrees of freedom g are for example, $g = 2$ for massive leptons, $g = 1$ for neutrinos and $g = 6$ for quarks, counting particles and antiparticles separately.[5]

In kinetic equilibrium the distribution function of a particle is given by

$$f(E, \mu, T) = n_{F,B}(E - \mu) = \frac{1}{e^{(E-\mu)/T} \pm 1} \ , \tag{3.6}$$

where $+$ corresponds to fermions (Fermi-Dirac distribution) and $-$ corresponds to bosons (Bose-Einstein distribution). These distribution functions depend on the energy of the particle E, the temperature T and the chemical potential of the particle μ. If a particle does not carry any conserved charge, the corresponding chemical potential vanishes, $\mu = 0$. Since photons and gluons carry no conserved charges, their chemical potentials are zero, $\mu_\gamma = \mu_g = 0$. Thus, with the additional substitution

[5] We would like to emphasize that our notation for the degrees of freedom g_i differs from the one often used in textbooks g_i, like in [51]. We count particles and antiparticles separately, whereas textbooks often combine them. Thus there is a factor of 2 difference between our counting g_i and the other one $\mathrm{g}_i = 2g_i$ (i.e. $\mathrm{g}_i = 4$ for massive leptons, $\mathrm{g}_i = 2$ for neutrinos and $\mathrm{g}_i = 12$ for quarks).

$|\mathbf{p}| = \sqrt{E^2 - m^2}$, Eqs. (3.3)–(3.5) become:

$$\mathrm{n}(E,\mu,T) = \frac{g}{2\pi^2}\int_m^\infty \mathrm{d}E \frac{E\sqrt{E^2-m^2}}{e^{(E-\mu)/T}\pm 1}\ , \tag{3.7}$$

$$\epsilon(E,\mu,T) = \frac{g}{2\pi^2}\int_m^\infty \mathrm{d}E \frac{E^2\sqrt{E^2-m^2}}{e^{(E-\mu)/T}\pm 1}\ , \tag{3.8}$$

$$p(E,\mu,T) = \frac{1}{3}\frac{g}{2\pi^2}\int_m^\infty \mathrm{d}E \frac{(E^2-m^2)^{\frac{3}{2}}}{e^{(E-\mu)/T}\pm 1}\ . \tag{3.9}$$

In general, these integrals cannot be solved analytically. But for relativistic particles, i.e., $T \gg m$, and nonrelativistic particles, i.e., $T \ll m$, the formulas can be simplified.[6] For the relativistic case, i.e., $T \gg m$, we can set the mass to zero and expand in μ/T:

$$\mathrm{n} = \begin{cases} \frac{1}{\pi^2}\zeta(3)gT^3 + \frac{1}{6}gT^2\mu + \mathcal{O}(T\mu^2)\ , & \text{bosons} \\ \frac{3}{4\pi^2}\zeta(3)gT^3 + \frac{1}{12}gT^2\mu + \mathcal{O}(T\mu^2)\ , & \text{fermions} \end{cases}\ , \tag{3.10}$$

$$\epsilon = \begin{cases} \frac{\pi^2}{30}gT^4 + \frac{3}{\pi^2}\zeta(3)gT^3\mu + \frac{1}{4}gT^2\mu^2 + \mathcal{O}(\mu^3)\ , & \text{bosons} \\ \frac{7}{8}\frac{\pi^2}{30}gT^4 + \frac{9}{4\pi^2}\zeta(3)gT^3\mu + \frac{1}{8}gT^2\mu^2 + \mathcal{O}(\mu^3)\ , & \text{fermions} \end{cases}\ , \tag{3.11}$$

$$p = \epsilon/3\ , \tag{3.12}$$

where $\zeta(3) = \sum_{n=1}^{\infty}(1/n^3) \approx 1.202$ is the Riemann zeta function. In the case of vanishing chemical potential $\mu = 0$ we get for the average particle energy in kinetic equilibrium

$$\langle E\rangle = \frac{\epsilon}{\mathrm{n}} = \begin{cases} \frac{\pi^4}{30\zeta(3)}T \approx 2.701T\ , & \text{bosons} \\ \frac{7\pi^4}{180\zeta(3)}T \approx 3.151T\ , & \text{fermions} \end{cases}\ . \tag{3.13}$$

In the nonrelativistic limit $T \ll m$ and $T \ll m - \mu$, the second condition leads to a dilute system, i.e. occupation numbers $\ll 1$, which is usually satisfied in cosmology when the first condition is satisfied, disregarding systems of high density like, e.g., white dwarfs, neutron stars or other hypothetical compact stars like pion stars [52]. In this limit one can approximate

$$e^{\frac{E-\mu}{T}} \pm 1 \approx e^{\frac{E-\mu}{T}}\ , \tag{3.14}$$

[6] For bosons the chemical potential cannot be greater than the particle mass, as the distribution function given by Eq. (3.6) should be positive definite for all energies. Thus the formulas for relativistic bosons only apply for $\mu_i \ll m_i \ll T \Rightarrow \frac{\mu_i}{T} \ll 1$ and in the case that no Bose-Einstein condensate forms.

which leads to Maxwell-Boltzmann statistics for the distribution function f which is the same for bosons and fermions. With $E \approx m + \frac{p^2}{2m}$ the distribution function looks like

$$f(p, \mu, T) \approx \exp\left(-\frac{m}{T} + \frac{\mu}{T} - \frac{p^2}{2mT}\right) . \tag{3.15}$$

Thus, the thermodynamic variables read in the nonrelativistic limit $T \ll m$:

$$\mathrm{n} = g\left(\frac{mT}{2\pi}\right)^{\frac{3}{2}} e^{-\frac{m-\mu}{T}} , \tag{3.16}$$

$$\epsilon = \mathrm{n}\left(m + \frac{3T}{2}\right) , \tag{3.17}$$

$$p = \mathrm{n}T \ (\ll \epsilon) , \tag{3.18}$$

$$\Rightarrow \langle E \rangle = m + \frac{3T}{2} . \tag{3.19}$$

For a system in chemical equilibrium we can find relations between the chemical potentials of different particle species according to the reaction formulas, as

$$a + b \leftrightarrow c + d \tag{3.20}$$

$$\Rightarrow \mu_a + \mu_b = \mu_c + \mu_d . \tag{3.21}$$

In particular, in chemical equilibrium annihilation and pair production processes are in equilibrium. This means that the chemical potentials of particles and antiparticles are equal in magnitude and opposite in sign, i.e., $\mu_{\bar{i}} = -\mu_i$ due to $\mu_i + \mu_{\bar{i}} = 2\mu_\gamma = 0$. All chemical potentials can be expressed in terms of chemical potentials of conserved charges and there are as many independent chemical potentials as independent conserved charges in a system (cf. Sec. 7.1).

The net number density of a particle species, i.e., the *particle asymmetry*, is given by the number density of a particle i minus the density of its antiparticle $\bar{i}$:

$$\begin{aligned} n_i &= \mathrm{n}_i - \mathrm{n}_{\bar{i}} \\ &= \frac{g_i}{2\pi^2} \int_{m_i}^{\infty} \mathrm{d}E E \sqrt{E^2 - m_i^2} \, (f_i - f_{\bar{i}}) \\ &= \frac{g_i}{2\pi^2} \int_{m_i}^{\infty} \mathrm{d}E E \sqrt{E^2 - m_i^2} \left(\frac{1}{e^{(E-\mu_i)/T} \pm 1} - \frac{1}{e^{(E+\mu_i)/T} \pm 1}\right) . \end{aligned} \tag{3.22}$$

We obtain exact, analytic results in the relativistic (cf. Eqs. (A.11), (A.12)) and

nonrelativistic limit (according to Eq. (3.16)):

$$n_i(T,\mu_i) \overset{(T\gg m_i)}{=} \begin{cases} \frac{g_i}{6\pi^2}T^3\left[2\pi^2\frac{\mu_i}{T}-\left(\frac{\mu_i}{T}\right)^3\right] , & \text{bosons} \\ \frac{g_i}{6\pi^2}T^3\left[\pi^2\frac{\mu_i}{T}+\left(\frac{\mu_i}{T}\right)^3\right] , & \text{fermions} \end{cases} \tag{3.23}$$

$$\overset{(T\ll m_i)}{=} 2g_i\left(\frac{m_iT}{2\pi}\right)^{\frac{3}{2}}\sinh\left(\frac{\mu_i}{T}\right)\exp\left(-\frac{m_i}{T}\right) . \tag{3.24}$$

The total energy density and total pressure of a particle species,

$$\begin{aligned}\epsilon_{\text{tot},i} &= \epsilon_i + \epsilon_{\bar{i}} \\ &= \frac{g_i}{2\pi^2}\int_{m_i}^{\infty}\mathrm{d}E E^2\sqrt{E^2-m_i^2}\left(\frac{1}{e^{(E-\mu_i)/T}\pm 1}+\frac{1}{e^{(E+\mu_i)/T}\pm 1}\right) ,\end{aligned} \tag{3.25}$$

$$\begin{aligned}p_{\text{tot},i} &= p_i + p_{\bar{i}} \\ &= \frac{1}{3}\frac{g_i}{2\pi^2}\int_{m_i}^{\infty}\mathrm{d}E\left(E^2-m_i^2\right)^{\frac{3}{2}}\left(\frac{1}{e^{(E-\mu_i)/T}\pm 1}+\frac{1}{e^{(E+\mu_i)/T}\pm 1}\right) ,\end{aligned} \tag{3.26}$$

can also be solved analytically in the relativistic limit using Eqs. (A.11) and (A.12) and in the nonrelativistic limit using Eqs. (3.17) and (3.18):

$$\epsilon_{\text{tot},i} \overset{(T\gg m_i)}{=} \begin{cases} g_iT^4\left[\frac{\pi^2}{15}+\frac{1}{2}\left(\frac{\mu_i}{T}\right)^2-\frac{1}{8\pi^2}\left(\frac{\mu_i}{T}\right)^4\right] , & \text{bosons} \\ g_iT^4\left[\frac{7\pi^2}{120}+\frac{1}{4}\left(\frac{\mu_i}{T}\right)^2+\frac{1}{8\pi^2}\left(\frac{\mu_i}{T}\right)^4\right] , & \text{fermions} \end{cases} \tag{3.27}$$

$$\overset{(T\ll m_i)}{=} 2g_i\left(\frac{m_iT}{2\pi}\right)^{\frac{3}{2}}\cosh\left(\frac{\mu_i}{T}\right)\exp\left(-\frac{m_i}{T}\right)\left(m_i+\frac{3}{2}T\right) , \tag{3.28}$$

$$p_{\text{tot},i} \overset{(T\gg m_i)}{=} \epsilon_{\text{tot},i}/3 , \tag{3.29}$$

$$\overset{(T\ll m_i)}{=} 2g_i\left(\frac{m_iT}{2\pi}\right)^{\frac{3}{2}}\cosh\left(\frac{\mu_i}{T}\right)\exp\left(-\frac{m_i}{T}\right)T , \tag{3.30}$$

If we have a closer look at the behavior of the particle net number density n, energy density ϵ and pressure p, we see that they fall exponentially as the temperature drops below the mass of the particle for small chemical potentials. As the universe expands and cools down, particles and antiparticles annihilate and cannot be produced in pairs again. The annihilation temperature is roughly $T_{\text{ann}} \simeq m_i/3$ and the annihilation process is not instantaneous but takes several Hubble times (cf. [51]).

Entropy and Effective Relativistic Degrees of Freedom

We can derive an expression for the entropy S in co-moving volume with the first law of thermodynamics,

$$T\mathrm{d}S = \mathrm{d}(\epsilon V) + p\mathrm{d}V - \mu\mathrm{d}N \ . \tag{3.31}$$

Hence, we get for the entropy density

$$s = \frac{\epsilon + p - \mu \mathrm{n}}{T} \ , \tag{3.32}$$

with $n = N/V$ and where we implicitly sum over particles, antiparticles and different particle species, i.e., (using $\mu_{\bar{i}} = -\mu_i$)

$$s = \sum_i \frac{\epsilon_i + \epsilon_{\bar{i}} + p_i + p_{\bar{i}} - \mu_i(\mathrm{n}_i - \mathrm{n}_{\bar{i}})}{T} \tag{3.33}$$

$$= \sum_i \frac{\epsilon_{\mathrm{tot},i} + p_{\mathrm{tot},i} - \mu_i n_i}{T} \ . \tag{3.34}$$

Thus, we can determine the entropy density of a system with the help of the formulas for n_i, $\epsilon_{\mathrm{tot},i}$ and $p_{\mathrm{tot},i}$ using Eqs. (3.22), (3.25), and (3.26), respectively.

Considering now nonvanishing chemical potentials in the early universe in the relativistic limit, $T \gg m$, leads to the analytic result for the total entropy density

$$s(T) \overset{(T \gg m_i)}{=} \frac{2\pi^2}{45} T^3 g_{*s}(T,\mu) = \frac{2\pi^2}{45} T^3 \left(g_{*s} + \Delta g_{*s}\right) \ , \tag{3.35}$$

where $g_{*s}(T,\mu)$ counts the effective relativistic degrees of freedom, for which we sum over all relativistic bosonic and fermionic degrees of freedom

$$\begin{aligned} g_{*s} &= \sum_{i=\mathrm{bosons}} 2g_i \left(\frac{T_i}{T}\right)^3 + \frac{7}{8} \sum_{i=\mathrm{fermions}} 2g_i \left(\frac{T_i}{T}\right)^3 \ , \\ \Delta g_{*s} &= \frac{15}{4\pi^2} \sum_{i=\mathrm{bosons}} 2g_i \left(\frac{T_i}{T}\right)^3 \left(\frac{\mu_i}{T_i}\right)^2 + \frac{15}{8\pi^2} \sum_{i=\mathrm{fermions}} 2g_i \left(\frac{T_i}{T}\right)^3 \left(\frac{\mu_i}{T_i}\right)^2 \ . \end{aligned} \tag{3.36}$$

Δg_{*s} denotes a shift in the entropy density due to nonvanishing chemical potentials. The number of effective relativistic degrees of freedom itself depends on the temperature, since particle species annihilate with decreasing temperature and thus $g_{*s}(T,\mu)$ becomes smaller. At early times in the evolution of the universe all particles have a common temperature, but for temperatures $T \lesssim 1$ MeV the neutrinos decouple from the plasma and after electron-positron annihilation this leads to $T_\nu = (4/11)^{1/3} T_\gamma$.

Analogously, we can derive the effective relativistic degrees of freedom according to the total energy density, where we sum over all relativistic bosonic and fermionic particles and antiparticles:

$$\epsilon_{\mathrm{tot}} = \sum_{i=b,f} \epsilon_{\mathrm{tot},i} \tag{3.37}$$

$$\overset{(T \gg m_i)}{=} \frac{\pi^2}{30} T^4 \left(g_{*\epsilon} + \Delta g_{*\epsilon}\right) \ , \tag{3.38}$$

with the effective relativistic degrees of freedom according to Eq. (3.27),

$$\begin{aligned} g_{*\epsilon} &= \sum_{i=\mathrm{bosons}} 2g_i \left(\frac{T_i}{T}\right)^4 + \frac{7}{8} \sum_{i=\mathrm{fermions}} 2g_i \left(\frac{T_i}{T}\right)^4 \ , \\ \Delta g_{*\epsilon} &= \frac{15}{4\pi^2} \sum_{i=\mathrm{bosons}} 2g_i \left(\frac{T_i}{T}\right)^4 \left[2\left(\frac{\mu_i}{T_i}\right)^2 - \frac{1}{2\pi^2}\left(\frac{\mu_i}{T_i}\right)^4\right] \\ &\quad + \frac{15}{8\pi^2} \sum_{i=\mathrm{fermions}} 2g_i \left(\frac{T_i}{T}\right)^4 \left[2\left(\frac{\mu_i}{T_i}\right)^2 + \frac{1}{\pi^2}\left(\frac{\mu_i}{T_i}\right)^4\right] \ . \end{aligned} \tag{3.39}$$

Note that in general $\Delta g_{*\epsilon} \neq \Delta g_{*s}$ and thus $g_{*\epsilon}(T,\mu) \neq g_{*s}(T,\mu)$. For small chemical potentials and when all particles have a common temperature, $g_{*\epsilon}(T,\mu) \simeq g_{*s}(T,\mu)$ for a wide range of temperatures (cf. [49]). In total, nonvanishing chemical potentials will enhance the number of effective relativistic degrees of freedom. This will be discussed in detail in Sec. 7.4.

3.3 Particle Asymmetries in the Early Universe

As the entropy density s is conserved in co-moving volume during the expansion of the universe, it is important for describing conserved quantities like conserved number densities, i.e., charges, during the evolution of the universe. The entropy density and the number densities scale as a^{-3}. Thus, if a quantity or charge X is conserved, the specific asymmetry,

$$x \equiv \frac{n_X}{s} \ , \tag{3.40}$$

remains constant during the evolution of the universe.

Very often asymmetries, like the baryon asymmetry, are referred to in terms of the number-to-photon ratio

$$\eta_X \equiv \frac{n_X}{n_\gamma} = \frac{\mathrm{n}_X - \mathrm{n}_{\bar{X}}}{n_\gamma} \ . \tag{3.41}$$

The total photon density is according to Eq. (3.10) given by $n_\gamma = \frac{2\zeta(3)}{\pi^2} T^3$. Then with Eq. (3.35) we can express the entropy density in terms of the photon density:

$$n_\gamma = \frac{45\zeta(3)}{\pi^4 g_{*s}(T,\mu)} s \simeq \frac{1}{1.80 g_{*s}(T,\mu)} s \ . \tag{3.42}$$

Thus, the number-to-photon ratio can be related to the specific asymmetry,

$$\eta_X = \frac{n_X}{n_\gamma} = 1.80 g_{*s}(T,\mu) \frac{n_X}{s} \ . \tag{3.43}$$

For a conserved quantity its number-to-photon ratio does not remain constant because g_{*s} changes with temperature. After electron-positron annihilation ($T \sim 0.5$ MeV) $g_{*s} = 3.909$ is constant, which yields $s \cong 7.04\ n_\gamma$ at vanishing chemical potentials.

After the electroweak crossover $T_{\mathrm{EW}} \sim 100$ GeV and before neutrino oscillations start at $T_{\mathrm{osc}} \sim 10$ MeV, the baryon number B and individual lepton flavor numbers L_α are conserved, since so far no processes violating lepton or baryon number have been observed. Moreover, the electric charge is conserved and we assume charge neutrality of the universe, i.e., $Q = 0$, which seems to be reasonable due to the lack of currents on large scales (see [17] for an upper limit). With the particle net number density n_i, which is in thermal and chemical equilibrium given by Eq. (3.22), we obtain five local conservation laws for the specific lepton flavor asymmetries l_α, specific baryon asymmetry b and electric charge density q:

$$l_\alpha = \frac{n_{L_\alpha}}{s} = \frac{n_\alpha + n_{\nu_\alpha}}{s} \quad , \quad \alpha \in \{e, \mu, \tau\} \ , \tag{3.44}$$

$$b = \frac{n_B}{s} = \sum_i \frac{B_i n_i}{s} \quad , \quad B_i = \text{baryon number of species } i \ , \tag{3.45}$$

$$q = 0 = \frac{n_Q}{s} = \sum_i \frac{Q_i n_i}{s} \quad , \quad Q_i = \text{electric charge of species } i \ . \tag{3.46}$$

3.4 Phase Transitions

Phase transitions occur in various physical systems. In general, a system, e.g., matter, exhibits different phases which can be distinguished by their symmetries and by their thermal, mechanical, and electromagnetic properties. External conditions, like pressure, temperature, or electric and magnetic fields, determine which phase is existent. Changing the external conditions can lead to a phase transition in the

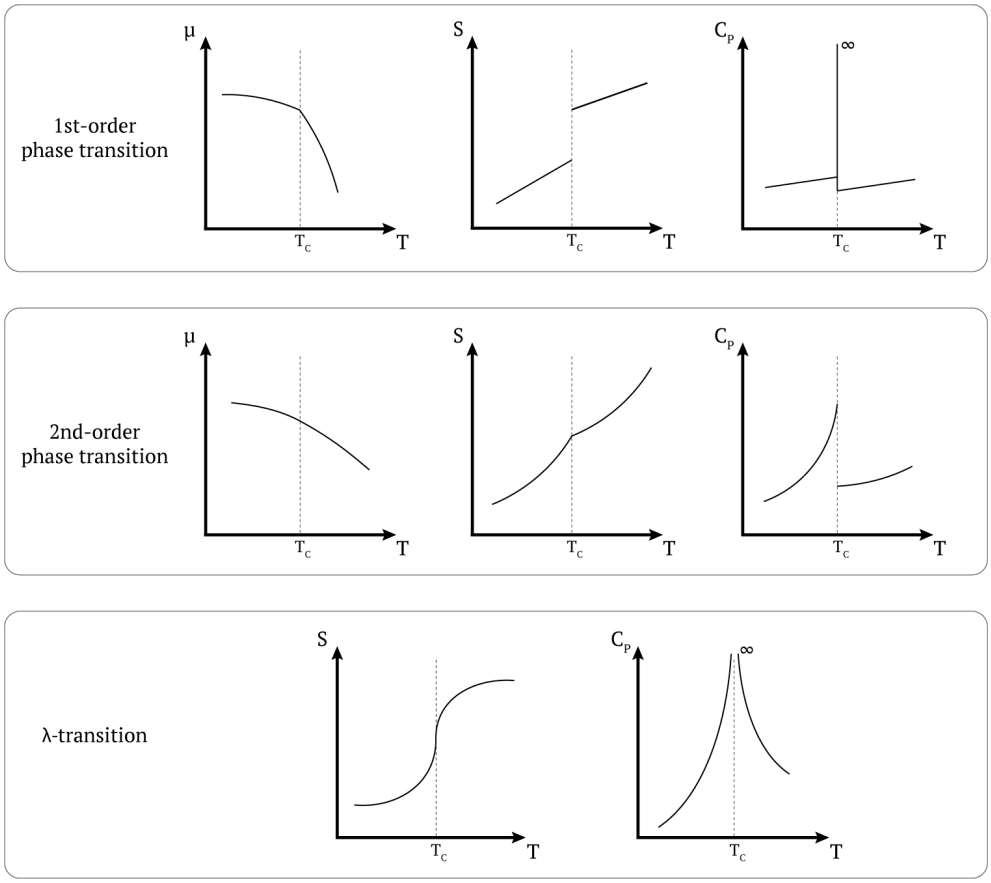

Fig. 3.1: Sketch of the behavior of the chemical potential μ, the entropy S and the heat capacity C_P for constant pressure at a first- and second-order phase transition, respectively.

physical system. At a phase transition an applicable thermodynamic potential, e.g., the Gibbs free energy G, is not an analytic function of an order parameter.

Paul Ehrenfest classified phase transition in the following way: A transition for which the n-th derivative of the thermodynamic potential is discontinuous is a n-th order phase transition, all lower derivatives are continuous. Thus, at a first-order phase transition the first derivative of the thermodynamic potential is discontinuous. At a second-order phase transition the first derivative is continuous but the second derivative is discontinuous or possesses a singularity. Another possibility to classify phase transitions is by latent heat. A first-order phase transition is a transition which involves a jump in the entropy. The entropy difference between the two phases corresponds to a thermal energy $Q = T(S_2 - S_1)$, the so called latent heat. In contrast, phase transitions which do not involve latent heat are called continuous or of second or higher order.

At an equilibrium phase transition, the distinct phases of a homogeneous, physical system have to be in thermodynamic equilibrium with each other. This means, equality in the temperature $T_1 = T_2$, the pressure $p_1 = p_2$, and the chemical potential $\mu_1 = \mu_2$ for the two phases. For simplicity, let us consider a one-component system. In this case, the chemical potential is the same as the partial Gibbs free energy: $\mathrm{d}G = V\mathrm{d}p - S\mathrm{d}T + \sum_i \mu_i \mathrm{d}N_i$ with $\mu_i = \partial G/\partial N_i|_{p,T,N_{j\neq i}}$ at constant pressure and temperature. Here μ_i and N_i with $i = 1, 2$ are the chemical potential and number of particles in phase 1 or 2, respectively. The chemical potential features the same behavior at a phase transition as the thermodynamic potential, i.e., the Gibbs free energy. Accordingly, the entropy is given by the first derivative

$$S = -\left.\frac{\partial G}{\partial T}\right|_{p,N} = -N\left.\frac{\partial \mu}{\partial T}\right|_{p,N} . \tag{3.47}$$

The second derivative can be described by the heat capacity

$$C_p = T\left.\frac{\partial S}{\partial T}\right|_{p,N} = -T\left.\frac{\partial^2 G}{\partial T^2}\right|_{p,N} . \tag{3.48}$$

Figure 3.1 shows a sketch of the behavior of the chemical potential, entropy, and heat capacity for a first- and a second-order phase transition, respectively. For a first-order phase transition the chemical potential is continuous but exhibits a kink at the transition temperature T_c. The entropy exhibits a jump, which involves the release or need of latent heat, and the heat capacity diverges. A second-order phase transition is reflected by a kink in the entropy and a jump in the heat capacity. However, more often a second-order phase transition does not exhibit a kink in the entropy but a vertical tangent at T_c. The specific heat then diverges at T_c with a characteristic λ-shaped form, which is why these transitions are called λ-transitions (see Fig. 3.1). For λ-transitions, the phase transition can already be anticipated by the behavior of C_p in the vicinity of T_c. For these cases a critical exponent can be defined which describes the divergence behavior.[7]

In the early universe the external parameter, which changes and drives phase transitions, is the expansion, or rather the decreasing temperature. In Chapter 5 the QCD transition will be discussed in some more detail. For a more detailed discussion about phase transitions in general see, e.g., Ref. [53].

[7] An example for a material which features a λ-transition is ^{4}He.

4 Large Lepton Asymmetries

In this Chapter we will elaborate on some aspects of lepton asymmetries: constraints due to BBN and CMB (Sec. 4.1) and possible production mechanisms of large primordial lepton asymmetries (Sec. 4.2).

The matter-antimatter asymmetry in the universe is an important aspect of cosmological evolution. One big problem in cosmology and particle physics is to explain the very existence of the matter-antimatter asymmetry as well as its value. It is not intuitive that the initial condition of the universe is not baryon-symmetric. In the SM particle asymmetries would have been diluted away by the inflationary expansion and washed out during the following reheating phase by the increasing entropy density in the universe. Thus primordial particle asymmetries have to be produced after the inflationary phase of the universe. The requirements for generating baryon asymmetry are given by the three Sakharov conditions [54]:

- Baryon number B violation,
- C- and CP-symmetry violation and
- interactions out of equilibrium.

If we start with a matter symmetric phase at high temperatures, the baryon asymmetry generated through C and CP violating processes and deviations from thermal equilibrium in the SM fails to explain the observed value and is about eigth orders of magnitude to small [4]. However, there are many possible mechanisms of baryon asymmetry generation. One is baryogenesis via leptogenesis [5].

The lepton asymmetry l, defined in analogy to the baryon asymmetry b, is a key parameter to better understand the origin of the matter-antimatter asymmetry. One can imagine scenarios in which asymmetries in baryons, leptons or both are generated in the first place. The idea of leptogenesis is to create a lepton asymmetry (cf. [55, 56]). Before the electroweak transition at $T_{\mathrm{EW}} \sim 100$ GeV sphaleron processes, which violate baryon and lepton number such that $B - L$ is conserved, partly convert a primordial lepton asymmetry to a baryon asymmetry. In the SM this leads to $l = -(51/28)b$ [6], which is the reason for suggesting $l \simeq \mathcal{O}(b)$. However, there might be an (almost) cancellation in the sum of different flavor asymmetries due to different signs, which does not necessarily imply $l_\alpha \simeq \mathcal{O}(b)$. The specific lepton flavor asymmetries might be orders of magnitude larger while their sum, the total specific lepton asymmetry l, is on the order of the specific baryon asymmetry. Furthermore, there exist also models that predict a large lepton asymmetry nowadays, i.e., $|l| \gg b$, and there is no preference for either sign of l (see Sec. 4.2).

4.1 Cosmological Constraints on Lepton Asymmetries

Observationally, the lepton asymmetry is only weakly constrained. The charge neutrality of the universe (see [17] for an upper limit) links the asymmetry in the charged leptons to the tiny baryon asymmetry

$$\sum_{\alpha} \frac{\mathrm{n}_{\alpha} - \mathrm{n}_{\bar{\alpha}}}{s} \sim \frac{\mathrm{n}_{B} - \mathrm{n}_{\bar{B}}}{s} \ , \ \alpha \in \{e, \mu, \tau\} \ . \tag{4.1}$$

As taus and muons annihilated during the evolution of the universe, nowadays, the asymmetry between electrons and positrons is on the same order as the baryon asymmetry. Nevertheless, a much larger lepton asymmetry could reside in the cosmic neutrino background today, which cannot be detected directly. Constraints on the neutrino asymmetry can only be inferred indirectly by measurements and analyses of BBN and CMB.

As the asymmetry in charged leptons is negligible today, the total lepton asymmetry is mainly given by the sum of the neutrino flavor asymmetries n_{ν_α}, most frequently expressed via the number-to-photon ratio

$$\eta_l \approx \sum_{\alpha} \frac{n_{\nu_\alpha}}{n_\gamma} \ . \tag{4.2}$$

For the specific neutrino asymmetries, assuming massless neutrinos, we obtain with Eqs. (3.23) and (3.35) the following relations:

$$\eta_{\nu_\alpha} = \frac{n_{\nu_\alpha}}{n_\gamma} = \frac{1}{12\zeta(3)} \left(\frac{T_{\nu_\alpha}}{T_\gamma}\right)^3 \left[\pi^2 \xi_{\nu_\alpha} + \xi_{\nu_\alpha}^3\right] \ , \tag{4.3}$$

$$l_{\nu_\alpha} = \frac{n_{\nu_\alpha}}{s} = \frac{45}{12\pi^4 g_{*s}(T,\mu)} \left(\frac{T_{\nu_\alpha}}{T_\gamma}\right)^3 \left[\pi^2 \xi_{\nu_\alpha} + \xi_{\nu_\alpha}^3\right] \ , \tag{4.4}$$

$$l_{\nu_\alpha} = \frac{45\zeta(3)}{\pi^4 g_{*s}(T,\mu)} \eta_{\nu_\alpha} \approx \frac{1}{1.80 g_{*s}(T,\mu)} \eta_{\nu_\alpha} \ , \tag{4.5}$$

with the chemical potentials expressed through the dimensionless variable $\xi_i = \frac{\mu_i}{T_i}$. In the last step in Eq. (4.5) we used $T_{\nu_\alpha}/T_\gamma \equiv T_\nu/T_\gamma = (4/11)^{1/3}$ for all neutrino flavors after electron-positron annihilation and $\zeta(3) \approx 1.20206$.

For calculating the specific lepton asymmetry from observational bounds of BBN and CMB, we take the value of $g_{*s}(T,\mu)$ after electron-positron annihilation at $T \lesssim 0.5$ MeV according to Eq. (3.36):

$$\begin{aligned} g_{*s}(\mu) &= 2 + \frac{7}{8} 6 \left(\frac{T_\nu}{T_\gamma}\right)^3 + \frac{15}{8\pi^2} \sum_{\alpha} 2 \left(\frac{T_\nu}{T_\gamma}\right)^3 \xi_{\nu_\alpha}^2 \\ &= \frac{43}{11} + \frac{15}{11\pi^2} \sum_{\alpha} \xi_{\nu_\alpha}^2 \ . \end{aligned} \tag{4.6}$$

This is a good approximation for obtaining the upper bound on the asymmetries as for higher temperatures $g_{*s}(T, \mu)$ is larger.

Strong constraints on neutrino flavor asymmetries in the early universe stem from BBN and the CMB due to the change of the effective number of neutrino species, i.e., the number of relativistic species in the universe, called N_{eff}. In the SM there are three light active neutrinos. A deviation from this value is parametrized by $\Delta N_{\text{eff}} = N_{\text{eff}} - 3$ and can be due to, e.g., light additional neutrinos or other additional relativistic particles which thermalized during the evolution of the universe. Additional relativistic species increase the energy density of radiation through an increase of the effective relativistic degrees of freedom $\Delta g_* = 7/4 \Delta N_{\text{eff}}$. In fact, neutrinos are not completely decoupled at electron-positron annihilation. This and finite-temperature effects raise the SM-value to $\Delta N_{\text{eff}}^{\text{SM}} = 0.046$ [57]. Considering also neutrino oscillations yields $\Delta N_{\text{eff}}^{\text{SM}} = 0.045$ [58]. In addition, neutrino chemical potentials increase the energy density of neutrinos according to Eq. (3.27):

$$\epsilon_{\text{tot},\nu_\alpha} = \frac{7}{4}\frac{\pi^2}{30} T_{\nu_\alpha}^4 \left[1 + \frac{30}{7}\left(\frac{\xi_{\nu_\alpha}}{\pi}\right)^2 + \frac{15}{7}\left(\frac{\xi_{\nu_\alpha}}{\pi}\right)^4\right] . \tag{4.7}$$

Comparing this to the total energy density, given in Eq. (3.38), the contribution of neutrino chemical potentials to ΔN_{eff} is

$$\Delta N_{\text{eff}}^{\xi} = \sum_\alpha \frac{30}{7}\left[\left(\frac{\xi_{\nu_\alpha}}{\pi}\right)^2 + \frac{1}{2}\left(\frac{\xi_{\nu_\alpha}}{\pi}\right)^4\right] . \tag{4.8}$$

Irrespective of the sign, neutrino chemical potentials always induce an increase in N_{eff}.

In principle, the individual neutrino flavor asymmetries might be very different in the first place. However, it has been shown that neutrino oscillations equilibrate neutrino flavor asymmetries, which implies that they are approximately equal after decoupling [19–21, 59]. As neutrino flavor oscillations are effective before BBN and CMB, these analyses are blind to former, potentially unequal individual flavor asymmetries. Nonetheless, recent analyses showed that flavor equilibrium may not be reached, depending on the neutrino mixing angles and the size of the initial neutrino flavor asymmetries, causing sizeable flavor asymmetries surviving neutrino oscillations and thus $l_\alpha \neq l/3$ [60–62].

We will use the concepts introduced here to calculate constraints on the lepton flavor asymmetries in the following. A detailed pedagogical introduction to this topic can also be found in [63].

4.1.1 Big Bang Nucleosynthesis

The standard BBN scenario is in good agreement with astrophysical observations. Thus, modifications due to neutrino asymmetries must be small enough to not change the predictions of light element abundances too much. BBN is affected by lepton asymmetries in two ways: On the one hand, the chemical potential of the electron neutrino changes the neutron-to-proton ratio at the onset of BBN [64, 65] (cf. Eq. (3.24)):

$$\frac{n_n}{n_p} \simeq \exp\left[-\frac{m_n - m_p - (\mu_n - \mu_p)}{T}\right] \simeq \exp\left[-\frac{m_n - m_p}{T} - \xi_{\nu_e}\right] , \qquad (4.9)$$

according to the equilibrium reaction $p + e \rightleftharpoons n + \nu_e \Rightarrow \mu_p + \mu_e = \mu_n + \mu_{\nu_e}$ and vanishingly small electron chemical potential.[8] Thus, the neutron-to-proton ratio will decrease for a positive chemical potential of the electron neutrino, which results in a smaller primordial abundance of ^{4}He, and vice versa. The change in the ^{4}He-abundance can be related to the change in the effective number of neutrino species $\Delta N_{\text{eff}}^{\xi_{\nu_e}} \simeq -20\xi_{\nu_e}$ [63]. On the other hand, lepton asymmetries lead to a faster expansion of the universe which can be expressed by $\Delta N_{\text{eff}}^{\xi}$, given by Eq. (4.8). This leads to an enhanced neutron-to-proton ratio during BBN and thus to a larger ^{4}He-abundance, as weak processes freeze out earlier. The first effect depends on ξ_{ν_e} and its sign, whereas the second effect depends only on the absolute value of all neutrino chemical potentials. Hence, a positive ξ_{ν_e} might lead to (partial) cancellation in the total $\Delta N_{\text{eff}} = \Delta N_{\text{eff}}^{\xi} + \Delta N_{\text{eff}}^{\xi_{\nu_e}}$.

In the absence of neutrino flavor oscillations the chemical potential of the electron neutrino can be constrained to $-0.018 \leq \xi_{\nu_e} \leq 0.008$ (68% C.L.) [19]. This leads, according to Eq. (4.4), to constraints on the specific electron neutrino lepton asymmetry $-0.002 \leq l_{\nu_e} \leq 0.001$. Assuming full equilibration of three initially different flavor asymmetries, i.e., $\eta_{\nu_\alpha} \simeq \eta_\nu/3$, due to oscillations (with a mixing angle $\sin^2\theta_{13} = 0.04$), the most stringent bound on the total neutrino asymmetry is given by $|\eta_\nu| \lesssim 0.1$ (95% C.L.) [19] and thus $|l| \lesssim 0.01$. A similar analysis leads to $-0.071 \lesssim \eta_\nu \lesssim 0.054$ (95% C.L.) and thus $-0.010 \lesssim l \lesssim 0.008$ [66]. Considering only partial equilibration weakens the bounds for ξ_μ and ξ_τ and thus for the total lepton asymmetry [62]. Furthermore, one should bear in mind that direct measurements of light element abundances are subject to sizeable systematic uncertainties as are constraints on lepton asymmetries derived thereby [18].

[8] Due to electric charge neutrality of the universe and the small baryon asymmetry we get $n_e/s = n_p/s \sim b \sim 10^{-10}$ and thus, according to Eq. (3.23), the electron chemical potential is small, $\mu_e/T \sim 10^{-10}$.

4.1.2 Cosmic Microwave Background

The CMB is influenced by large lepton asymmetries through modifications of the temperature anisotropies by a change of N_{eff}. Its value is constrained by observations to be $N_{\text{eff}} = 2.99^{+0.34}_{-0.33}$ (95% C.L.) [42]. Thus, we have $-0.34 \lesssim \Delta N_{\text{eff}} \lesssim 0.33$ and after subtracting $\Delta N_{\text{eff}}^{\text{SM}}$ we get $-0.385 \lesssim \Delta N_{\text{eff}}^{\xi} \lesssim 0.285$. According to Eq. (4.8) and assuming $\xi_{\nu_\alpha} = \xi_\nu$ for all flavors, the constraint on the chemical potential is $|\xi_\nu| \lesssim 0.465$ and for the total lepton asymmetry $|l| \lesssim 0.049$.[9] Considering a not equilibrated system, i.e., $\xi_{\nu_\mu} = \xi_{\nu_\tau} \neq \xi_{\nu_e}$, and the BBN constraint on ξ_{ν_e} mentioned in the previous Section, we get the constraints $|\xi_{\nu_{\mu,\tau}}| \lesssim 0.568 \Rightarrow |l_{\nu_{\mu,\tau}}| \lesssim 0.021$ and for the total lepton asymmetry $|l| \lesssim 0.041$. Even though this bound is more stringent on the total lepton asymmetry compared to the case of equal lepton flavor asymmetries, we get some more freedom in fine-tuning the lepton flavor asymmetries such that we can choose, e.g., $l_{\nu_\mu} = -l_{\nu_\tau}$. This might lead to an impact on cosmological evolution and possibly other observable consequences while keeping with the constraints on the total lepton asymmetry and thus on the observed N_{eff} (cf. Chapter 7).

A more sophisticated model fitting to Planck 2015 data [68] incorporates the effect of neutrino chemical potentials on ΔN_{eff} and on the ^{4}He-abundance which also influences the CMB [18]. Their constraints for equal lepton flavor asymmetries are $\xi_\nu = -0.002^{+0.114}_{-0.111}$ (95% C.L.) which imply $|l| \lesssim 0.012$. This represents the strongest constraints on the lepton asymmetry obtained from CMB data analysis so far and we will consider this constraint for our calculations.

4.2 Production Mechanisms

A possible scenario of leptogenesis can be obtained via an extension of the SM by two additional generations of massive right-handed neutrinos with degenerated masses at the GeV-scale [5]. These right-handed neutrinos are coupled to the left-handed lepton doublet whereby the active, i.e., SM, lepton number is transferred to right-handed neutrino number.[10] If one right-handed neutrino is out of equilibrium one can generate an asymmetry in the active leptons.[11]

[9] Just recently, a study appeared where the same effect was investigated but with Planck 2013 data on N_{eff} [67].

[10] Note, that the total number of active lepton number plus right-handed neutrino number is conserved in the absence of further lepton number violating processes.

[11] Additionally, the mass differences and mixing of active neutrinos can be explained within this model. If one also wants to explain DM by this model, one has to add a third right-handed (also called sterile) neutrino, with a much lighter mass in the keV-range (cf. [69] for a review).

One method to generate remnant lepton asymmetries which are larger than the baryon asymmetry, is the production of lepton asymmetries after sphaleron processes cease to be efficient [9, 10], i.e., at $T < T_{\rm sph} \sim 130$ GeV [70]. In a recent study [10], it has been shown that late-time lepton asymmetry generation requires highly degenerate right-handed neutrinos masses, $\Delta M/M \sim 10^{-11}$, and small neutrino Yukawa couplings $|h| \sim 10^{-8}$. An interesting observation is that all lepton flavor asymmetries apparently reach the same constant value for $T \lesssim 15$ GeV. The remnant lepton asymmetries are on the order $l_\alpha > 10^{-7} \gg b$. At very low temperatures $T \ll M/\pi$ an additional contribution to the lepton asymmetries can be generated through the non-equilibrium decay of right-handed neutrinos [7, 8].

Another method is that large lepton asymmetries $|l| \gtrsim 10^{-2}$ are produced well above the electroweak scale, i.e., at $T \gg T_{\rm EW}$. The electroweak symmetry breaking occurs at much higher temperatures due to preexisting large lepton asymmetries and sphaleron processes are suppressed. This results in a baryon asymmetry consistent with observational bounds and an orders of magnitude larger lepton asymmetry [11–16]. Large lepton asymmetries at very early times can, for example, be generated through the Affleck-Dine mechanism via decaying supersymmetric partners of the SM particles [71], or in Grand Unified Theories [14].

5 Quantum Chromodynamics

Besides the generation of the matter-antimatter asymmetry, another important, yet not well understood event in the early universe is the transition from freely propagating quarks and gluons to hadrons. The cosmic QCD transition at approximately 10 μs after the Big Bang. This transition is accompanied with the most drastic change in the effective relativistic degrees of freedom g_{*s} during the evolution of the universe. The true kind of this transition is therefore of outermost interest for the thermodynamics of the early universe.

The cosmic QCD transition, depending on its nature, might create observable consequences. A first-order phase transition would result in a separation of cosmic phases [34]. Bubbles of hadron gas are nucleated in the quark-gluon plasma, grow and collide which produces gravitational waves [72, 73]. Furthermore, shrinking quark droplets could remain at the end of the phase transition forming (strange) quark nuggets [34] which could account for DM. Various other possible relics due to a first- or second-order cosmic QCD transition have been studied in the past like, e.g., magnetic fields, inhomogeneous BBN, black hole formation, QCD balls as CDM, or CDM clumps generated by the QCD transition itself. However, all have been ruled out to survive until today or are inconsistent with observational bounds. For a detailed review on the cosmic QCD transition and possible relics see, e.g., Ref. [33]. Independent of the nature of the transition, the specific behavior of the universe at this transition, i.e., the change of the effective relativistic degrees of freedom, modifies the primordial gravitational wave background. This could be measured by pulsar timing arrays [37]. Furthermore, for a large electric charge chemical potential, $|\mu_Q| \geq m_\pi$, pion condensation might occur in the early universe [35, 36].

However, the calculation of many quantities in QCD turns out to be very difficult owing to the intrinsic property of QCD, i.e., the running of the strong coupling constant α_s. The asymptotic freedom causes interactions between quarks and gluons to become asymptotically weaker at higher energy densities and vice versa [74, 75]. This is the underlying reason for the cosmic QCD transition from the quark-gluon plasma at high temperatures to the hadron gas at low temperatures.

5.1 Lattice QCD

Due to the highly non-perturbative behavior of QCD (α_s is close to unity at relatively low temperatures), the only first-principle method to perform calculations at $T \sim T_{\rm QCD}$ is based on lattice QCD today. The other possibility is to rely on predictions of effective models of QCD. The aim of lattice QCD is to understand the nature of the QCD transition and to be able to determine the EoS, i.e., the fundamental thermodynamic relation of QCD. Thus, one goal is to understand the QCD phase diagram in the (μ_B, T) plane.[12]

The idea of lattice QCD is to discretize the space-time on a four-dimensional lattice and then going to finer and finer lattice spacings to perform a vanishing lattice spacing, i.e., continuum limit, extrapolation. First lattice QCD studies of strongly interacting matter at nonvanishing temperature have been performed in the early 1980s [76–78]. It has been shown that for vanishing and small chemical potentials the QCD transition of the SM is a crossover [27, 28] (see, e.g., [79] for a review). The crossover or a potential phase transition should be related to chiral symmetry restoration. Thus, one can determine the crossover temperature $T_{\rm QCD}$ (also often called pseudo-critical temperature) studying chiral observables, e.g., by determining the inflection point of the chiral condensate $\langle\bar{\psi}\psi\rangle_f = \frac{T}{V}\frac{\partial \ln Z}{\partial m_f}$, with ψ the Dirac-spinor fields, or the peak of the chiral susceptibility $\chi_m^{fg} = \frac{\partial}{\partial m_g}\langle\bar{\psi}\psi\rangle_f$, where the quark flavors are denoted by f and g. For details on the determination of $T_{\rm QCD}$ see, e.g., Ref. [80, 81]. At vanishing chemical potential and physical quark masses $T_{\rm QCD}$ is according to the HotQCD collaboration given by [22]

$$T_{\rm QCD}(0) = (156.5 \pm 1.5)\ \text{MeV}\ , \tag{5.1}$$

and respectively $T_{\rm QCD}(0) \simeq 147(2) - 165(5)$ MeV by the Wuppertal-Budapest collaboration [80].

The region of nonvanishing baryon chemical potential is however not accessible with first principle lattice Monte Carlo calculations of the QCD partition function. Present lattice QCD methods require taking a path integral with a measure which includes a complex fermion determinant for finite baryon chemical potential, leading to the infamous sign problem in lattice QCD [26, 29–31]. To access the region of nonvanishing chemical potentials in order to better understand the QCD phase diagram different extrapolation methods have been developed: The Taylor series

[12] In fact this is just a two-dimensional projection of the $n+1$-dimensional diagram, where n is the number of conserved charges and 1 is the temperature dimension. Considering only strong interactions the conserved charges are baryon number B, electric charge Q, and strangeness S.

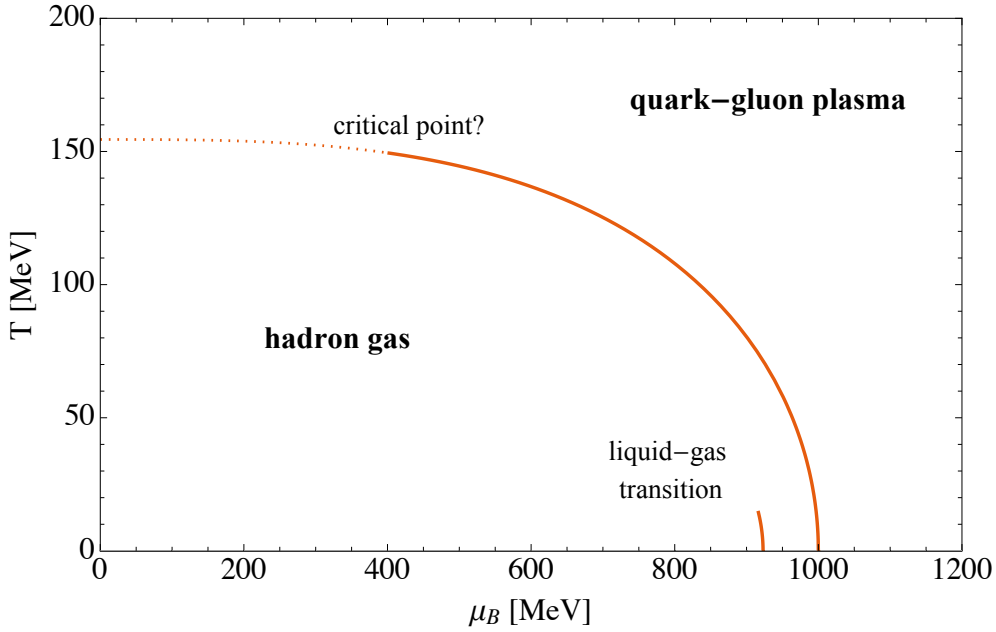

Fig. 5.1: Sketch of the QCD phase diagram in the (μ_B, T) plane. Solid lines denote first-order phase transitions, the dotted line a crossover transition.

method [82, 83], the reweighting method [84], analytic continuation of imaginary chemical potential for which no sign problem exists [85, 86], complexification of the gauge fields and then using a complex Langevin algorithm [87, 88] or Lefschetz thimbles [89] (see, e.g., [90] for a short review on different methods). In this thesis we will restrict ourselves to the discussion of lattice QCD results obtained by the Taylor series method, which is the state-of-the-art method and will be explained in detail in Chapter 6. With this method it has been shown that the curvature of the transition line $T_{\mathrm{QCD}}(\mu_B)$, separating confined from deconfined phase in the QCD phase diagram, is negative and surprisingly small [22, 91]. Recently, the application of lattice QCD for cosmology has been studied, regarding the change of the effective degrees of freedom and the topological susceptibility which can be used to predict the dark matter axion's mass [92].

For a pedagogical review on lattice QCD at finite temperatures and densities see, e.g., Ref. [93].

5.2 QCD Phase Diagram

In Fig. 5.1 the state-of-the-art conception of the QCD phase diagram in the (μ_B, T) plane is sketched. At high temperatures and/or densities, i.e., chemical potentials,

there is the phase of freely propagating quarks and gluons, the quark-gluon plasma. At low temperatures and/or densities quarks and gluons are confined into hadrons and we have a hadron gas. Effective models of QCD, like the Nambu–Jona-Lasinio model [23], predict a first-order chiral transition for vanishing temperatures and large baryon chemical potential $\mu_B > m_N$, with m_N the nucleon mass. For this reason, it is speculated that there might exist a critical line in the (μ_B, T) plane of the QCD phase diagram, which describes a first-order phase transition between the two phases [24]. This line is expected to end in a second-order critical endpoint, as for large temperatures and vanishing chemical potentials the transition is a smooth crossover, which is known by lattice simulations [25, 26]. Lattice calculations at finite densities aim to find the location of the critical endpoint or at least determine the region, for which the critical endpoint is disfavored by not seeing any hints of a phase transition behavior in the studied chiral observables. Roughly speaking a critical endpoint is disfavored for $\mu_B/T \lesssim 2$ [94]. More details on the search for the location of a possible critical endpoint are given in Chapter 8. Also pictured in Fig. 5.1 is the first-order liquid-gas transition of nuclear matter [95, 96]. At very large chemical potentials, i.e., baryon densities, there is the phase of color superconductivity (not shown in Fig. 5.1), which might be present in compact stars as, e.g., neutron stars and its existence might be tested by their observations (see, e.g., [97] for a review).

In the sketch of the QCD phase diagram in Fig. 5.1, one can also trace how the baryon chemical potential varied during the evolution of the universe, i.e., the cosmic trajectory in the (μ_B, T) plane. Actually, the cosmic trajectory lies in a $5+1$-dimensional space of chemical potentials for the conserved charges B, Q, L_α, and temperature. It is commonly assumed that the cosmic trajectory passes T_{QCD} at vanishing chemical potentials and proceeds to $\mu_B = m_N$, and $\mu_Q \approx \mu_{L_\alpha} \approx 0$ at $m_e \ll T \lesssim m_N$ (cf., e.g., [2]). As at low temperatures adding a baryon to the particle content of the universe requires the energy of the rest mass of the nucleus, i.e., proton or neutron assuming $m_p \approx m_n$. However, it has been shown that for $|l| \gg b$ the baryon and charge chemical potentials become on the order of $\mu_B \sim \mu_Q \sim l T_{\mathrm{QCD}}$ [2]. Thus, for large lepton asymmetries the cosmic trajectory will be shifted towards larger chemical potentials and maybe into the region of a possible first-order QCD transition.

In the following, the scenario of $l = -(51/28)b$ and equally distributed asymmetries between the lepton flavors will be referred to as the *standard scenario*. In Chapter 7 we will present the first precise calculation of the standard cosmic trajectory and the effect of large lepton asymmetries accounting for strong interaction effects around T_{QCD} [1].

The QCD phase diagram is not only tested by theoretical attempts but also by experiments. Heavy ion experiments have been built up with the goal to explore the transition to the quark-gluon plasma. The Large Hadron Collider (LHC) at CERN, and previously its precursors, investigates high energy heavy ion collisions which are probed with the ALICE experiment. The conditions at the LHC ($\mu_B \approx 0$) are close to the standard scenario in the early universe. However, the main difference between heavy ion collisions and cosmology is the time scale of the QCD transition. In cosmology the QCD transition lasts 10^{-5} s whereas in the laboratory it lasts only 10^{-23} s [33]. At the Relativistic Heavy Ion Collider (RHIC) the Beam Energy Scan program is dedicated to explore the phase diagram at different values of the baryon chemical potential and to find evidence for a second-order critical endpoint and a first-order transition line. For a recent review on experimental tests of the QCD phase diagram see, e.g., Ref. [98].

5.3 Perturbative QCD

At very high energies, the strong coupling constant α_s becomes small and the techniques of perturbation theory, i.e., an expansion in small α_s, can be applied to compute different observables of QCD and in particular the thermodynamic potential. However, a simple weak coupling expansion for finite-temperature field theories suffers from poor convergence behavior at $T \sim T_{\mathrm{QCD}}$. This is due to the fact that at high temperatures one has to consider plasma effects and cannot just consider massless particle states (see, e.g., [99] for a review). Thus improved perturbative theories have been applied. One approach is Hard Thermal Loop (HTL) perturbation theory which is known up to next-to-next-to-leading order in the massless limit [100] and recently the quark mass dependence has been studied up to next-to-leading order [101] (for an overview see, e.g., [102]). Another method is dimensional reduction (DR) [103]. For massless particles, the perturbative expansion has been calculated up to $\mathcal{O}(g^6 \ln(1/g))$ [104], where g is the renormalized strong coupling $\alpha_s \equiv g^2/(4\pi)$, which has been extended to finite temperature and chemical potentials [105–107]. The effect of finite quark masses up to $\mathcal{O}(g^2)$, while considering gluonic contributions up to $\mathcal{O}(g^6 \ln(1/g))$, has been studied in [49]. Results obtained by both improved pQCD methods are in agreement with lattice QCD results down to temperatures of about a few T_{QCD}. A recent comparison of lattice QCD results with HTL and DR results obtained agreement even down to $T \sim 250$ MeV [108].

At very high temperatures, $T \gg T_{\mathrm{QCD}}$, strong interactions should be negligible and the QCD part of the SM, i.e., quarks and gluons, should adequately be described

by an ideal gas of noninteracting particles. Due to considerably strong gluonic interactions up to very high temperatures [105, 109], the ideal gas limit is however not reached until $T \sim 1$ GeV (see Sec. 7.4).

In the following Chapters we will use the results for some thermodynamic quantities (pressure, entropy denstiy and energy density) for vanishing chemical potential obtained by [49][13] in the QCD temperature regime and to account for strong interactions between gluons at higher temperatures. They provide an interpolation for the SM equation of state over a wide temperature range, matching perturbative QCD (pQCD) results at low temperatures to lattice QCD results and at even lower temperatures to the HRG. The "weakly interacting" sector has been considered at 1-loop level. These present the to date most precise results including the effect of finite physical quark masses, even though the quark mass correction is small (about 5% on top to the total correction at $\mathcal{O}(g^2)$ of $20 - 30\%$). For a comparison of the parametrization of the EoS obtained by lattice QCD calculations and this pQCD approach see App. A.3.

5.4 Hadron Resonance Gas Model

Well below T_{QCD}, i.e., at $T \lesssim 130$ MeV, all studied observables of lattice QCD are remarkably well described by the ideal Hadron Resonance Gas (HRG) model [108, 110–113]. The HRG is based on assumptions of thermal equilibrium of a system composed of free hadrons and their resonances. Strong interactions of hadrons can effectively be approximated by this model because resonances represent the dominant part of the interactions among hadrons [114–116]. Thermodynamically the HRG can be described by the sum of the thermodynamic variables given by Eqs. (3.7)–(3.9) over hadron resonances up to a specified mass.

However, the success of the HRG is quite surprising and it is very likely that the HRG is not able to describe all strong interaction aspects of fluctuations in QCD thermodynamics. The highest temperature of agreement of HRG and lattice QCD varies in different observables, which may be a hint to the limitations of the HRG [108]. Furthermore, comparing lattice QCD with HRG results, deviations in the strangeness sector have been observed. These might be explained by additional strange resonances [117–119] which have not been observed experimentally yet, but have been predicted in lattice QCD [120] and quark model calculations [121, 122]. There exist attempts to improve the validitity range of the ideal HRG by the inclu-

[13] Their tabulated results can be found at http://www.laine.itp.unibe.ch/eos15/ .

sion of attractive and repulsive van der Waals interactions [123] or by accounting for the finite width of the resonances [124], which however do not succeed.

Due to the great success of the HRG in describing lattice QCD and experimental results below T_{QCD}, we will use it as an approximation for the low temperature regime $T \lesssim T_{\mathrm{QCD}}$ for our calculations of the evolution of the chemical potentials in Chapters 7 and 8.

6 Taylor Series Method

In this Chapter we will elaborate on the Taylor series method, which is at the moment the state-of-the-art first principle method to obtain access to the region of nonvanishing chemical potentials via lattice QCD calculations. Moreover, we will use this method to be able to use lattice QCD results for determining the cosmic trajectory accounting properly for strong interaction effects close to T_{QCD} in the following Chapter 7. For an overview of the Taylor series method applied to QCD see also Ref. [125].

We expand the QCD pressure, defined via the grand canonical potential $p = -\Omega/V$ (cf. Sec. 3.1), in a Taylor series in the chemical potentials up to second order,

$$p^{\mathrm{QCD}}(T,\mu) = p^{\mathrm{QCD}}(T,0) + \frac{1}{2!}\mu_a \chi_{ab} \mu_b + \mathcal{O}(\mu^4) \ , \tag{6.1}$$

with an implicit sum over $a, b \in \{B, Q\}$ here and in the following. The second order susceptibilities are defined by[14]

$$\chi_{ab}(T) \equiv \frac{1}{TV} \left\langle N_a N_b \right\rangle_{gc} \Big|_{\mu=0} = \frac{\partial^2 p^{\mathrm{QCD}}(T,\mu)}{\partial \mu_a \partial \mu_b} \Big|_{\mu=0} = \chi_{ba}(T) \ , \tag{6.2}$$

with $\langle \ldots \rangle_{gc}$ the grand canonical expectation value. Due to CP-symmetry, the pressure is symmetric under the exchange of particles and antiparticles, i.e., $\mu_i \longleftrightarrow -\mu_i$ (cf. Eq. (3.26)). Thus, expansion coefficients, i.e., susceptibilities, of odd powers vanish. The quadratic fluctuations of charges can be obtained by evaluating Eq. (6.2) at nonvanishing chemical potentials.

The conserved charge densities as functions of the chemical potentials follow as

$$n_a^{\mathrm{QCD}}(T,\mu) = \frac{\partial p^{\mathrm{QCD}}(T,\mu)}{\partial \mu_a} = \chi_{ab}\mu_b + \mathcal{O}(\mu^3) \ . \tag{6.3}$$

Thus, the susceptibilities can also be written as derivatives of the charge densities,

$$\chi_{ab}(T,\mu) = \frac{\partial n_a^{\mathrm{QCD}}(T,\mu)}{\partial \mu_b} \Big|_{\mu=0} \ . \tag{6.4}$$

We use the Taylor series ansatz of the pressure to account for contributions to the entropy and energy density due to nonvanishing chemical potentials (cf. [94]).[15] The

[14] Our notation for the susceptibilities differ from the one often used in lattice QCD papers: $\chi_{BB} \equiv \chi_2^B$, $\chi_{QQ} \equiv \chi_2^Q$, and $\chi_{BQ} \equiv \chi_{11}^{BQ}$.

[15] The basic thermodynamic quantity conveniently calculated on the lattice is $\Delta \equiv (\epsilon - 3p)/T^4 = T(\partial(p/T^4)/\partial T)_\xi$, which is often called "trace anomaly" (cf. [126]). All other thermodynamic variables are then deduced from it. In the ideal gas limit it vanishes and thus is a measure for the impact of masses and the strength of interactions.

entropy can be obtained according to the relation for the grand canonical potential, $\mathrm{d}\Omega = -p\mathrm{d}V - S\mathrm{d}T - N\mathrm{d}\mu$ thus $S = -(\partial\Omega/\partial T)_{\mu,V}$. Hence, with $p = -\Omega/V$ the entropy density of strongly interacting matter is given by

$$s^{\mathrm{QCD}}(T,\mu) = \left(\frac{\partial p^{\mathrm{QCD}}}{\partial T}\right)_{\mu,V} . \tag{6.5}$$

Inserting the Taylor series of the pressure given by Eq. (6.1) up to second order in μ we get:

$$s^{\mathrm{QCD}}(T,\mu) - s^{\mathrm{QCD}}(T,0) = \frac{1}{2}\frac{\mathrm{d}\chi_{ab}}{\mathrm{d}T}\mu_a\mu_b . \tag{6.6}$$

The energy density is according to Eq. (3.34) given by

$$\epsilon^{\mathrm{QCD}}(T,\mu) = Ts^{\mathrm{QCD}} - p^{\mathrm{QCD}} + \sum_a \mu_a n_a^{\mathrm{QCD}} . \tag{6.7}$$

Inserting Eqs. (6.1), (6.3), and (6.6) we get

$$\epsilon^{\mathrm{QCD}}(T,\mu) - \epsilon^{\mathrm{QCD}}(T,0) = \frac{1}{2}\left(T\frac{\mathrm{d}\chi_{ab}}{\mathrm{d}T} + \chi_{ab}\right)\mu_a\mu_b . \tag{6.8}$$

Thus, in order to determine the dependence of entropy and energy density on the chemical potentials, we need to determine the temperature derivatives of the lattice QCD susceptibilities $\mathrm{d}\chi_{ab}/\mathrm{d}T$.

6.1 Charge and Quark Number Susceptibilities

The conserved charge susceptibilities or fluctuations can be expressed through quark number susceptibilities or fluctuations by a change of basis. We can express the total electric charge and baryon asymmetry in QCD by the sum over the net numbers of strongly interacting particles:

$$N_B^{\mathrm{QCD}} = \sum_i B_i N_i , \tag{6.9}$$

$$N_Q^{\mathrm{QCD}} = \sum_i Q_i N_i , \tag{6.10}$$

with B_i the baryon number and Q_i the electric charge of particle species i. Thus, as only quarks are strongly interacting and contribute, we get[16]

$$N_B^{\mathrm{QCD}} = \frac{1}{3}\left(N_u + N_d + N_s + N_c + N_b + N_t\right) , \tag{6.11}$$

$$N_Q^{\mathrm{QCD}} = \frac{2}{3}\left(N_u + N_c + N_t\right) - \frac{1}{3}\left(N_d + N_s + N_b\right) . \tag{6.12}$$

[16] In fact, the contributions of bottom and top quarks are negligible at $T \sim T_{\mathrm{QCD}}$.

Inserting these equations in Eq. (6.2) yields relations between the conserved charge and quark number susceptibilities or fluctuations, respectively. The quark number susceptibilities are defined analogously to the conserved charge number susceptibilities,

$$\chi_{qq'} \equiv \frac{1}{TV} \langle N_q N_{q'} \rangle_{gc} \bigg|_{\mu=0} = \frac{\partial n_q(T,\mu)}{\partial \mu_{q'}} \bigg|_{\mu=0} \tag{6.13}$$

with $q, q' \in \{u, d, s, c, b, t\}$.

For convenience, let us have a closer look at the 2+1+1 flavor system, i.e., considering up, down, strange, and charm quark.[17] The equations just become lengthy for considering all quark flavors without providing new insights. For this system, the relations between the susceptibilities are (suppressing the index gc)

$$\begin{aligned}
\chi_{BB} &= \frac{1}{9}\frac{1}{TV} \langle (N_u + N_d + N_s + N_c)^2 \rangle \bigg|_{\mu=0} \\
&= \frac{1}{9}\frac{1}{TV} \Big(\langle N_u^2 \rangle + \langle N_d^2 \rangle + \langle N_s^2 \rangle + \langle N_c^2 \rangle + 2\langle N_u N_d \rangle + 2\langle N_u N_s \rangle \\
&\qquad + 2\langle N_u N_c \rangle + 2\langle N_d N_s \rangle + 2\langle N_d N_c \rangle + 2\langle N_s N_c \rangle \Big) \bigg|_{\mu=0} \\
&= \frac{1}{9} \left(\chi_{uu} + \chi_{dd} + \chi_{ss} + \chi_{cc} + 2\chi_{ud} + 2\chi_{us} + 2\chi_{uc} + 2\chi_{ds} + 2\chi_{dc} + 2\chi_{sc} \right) ,
\end{aligned} \tag{6.14}$$

and analogously

$$\chi_{QQ} = \frac{1}{9} \left(4\chi_{uu} + \chi_{dd} + \chi_{ss} + 4\chi_{cc} - 4\chi_{ud} - 4\chi_{us} + 8\chi_{uc} + 2\chi_{ds} - 4\chi_{dc} - 4\chi_{sc} \right) , \tag{6.15}$$

$$\chi_{BQ} = \frac{1}{9} \left(2\chi_{uu} - \chi_{dd} - \chi_{ss} + 2\chi_{cc} + \chi_{ud} + \chi_{us} + 4\chi_{uc} - 2\chi_{ds} + \chi_{dc} + \chi_{sc} \right) . \tag{6.16}$$

To get an intuition on the quark flavor dependence of the conserved charge susceptibilities we can evaluate Eqs. (6.14)–(6.16) in the ideal quark gas approximation and vary the numbers of considered quark flavors. We refer to a noninteracting gas of massive quarks in thermal equilibrium, whose particle densities are given by Eq. (3.22), as the ideal quark gas approximation. In this approximation all

[17] Lattice QCD calculations are performed at degenerate light quark masses, i.e., $m_u = m_d$. Thus up and down quarks are referred to as "2" in their notation of how many quark flavor are considered in a calculation. We will adopt this notation, even though in calculations we perform directly we will consider $m_u \neq m_d$.

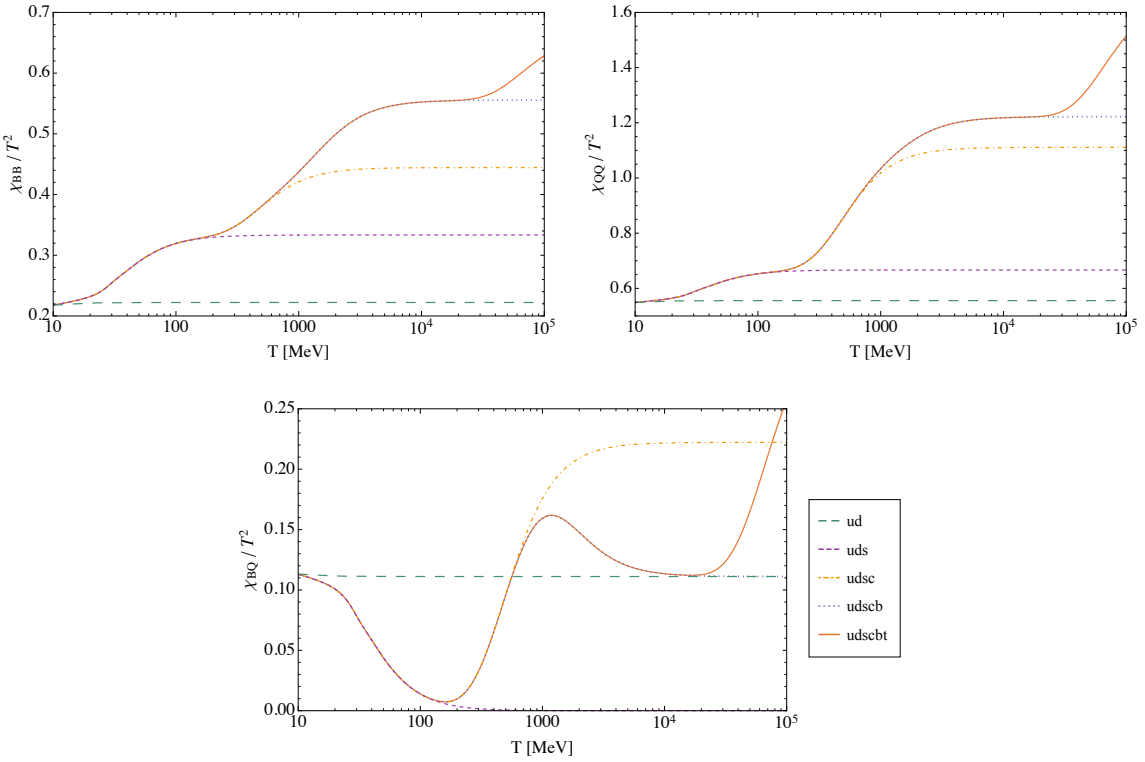

Fig. 6.1: Conserved charge susceptibilities in the ideal quark gas approximation for varying quark flavor content.

off-diagonal quark number susceptibilities, $q \neq q'$, vanish and the diagonal quark number susceptibilities, $q = q'$, are given by

$$\chi_{qq} = \left.\frac{\partial n_q}{\partial \mu_q}\right|_{\mu_q=0} = -\frac{g_q}{\pi^2}\int_{m_q}^{\infty} \mathrm{d}E E\sqrt{E^2-m_q^2}\underbrace{\left(-\frac{1}{T}\right)\Big[1-n_F(E)\Big]n_F(E)}_{=n_F'(E)=\frac{\mathrm{d}}{\mathrm{d}E}n_F(E)} \ . \tag{6.17}$$

For vanishing mass this integral evaluates to $\chi_{qq} = g_q T^2/6$, whereas for massive particles this integral is given by

$$\left.\frac{\partial n_i}{\partial \mu_i}\right|_{\mu_i=0} = \frac{m_i^2}{\pi^2}\sum_{k=1}^{\infty}(-1)^{k+1}K_2\left(\frac{km_i}{T}\right) \ , \tag{6.18}$$

where K_2 is a modified Bessel function.

In Fig. 6.1 the numerical evaluation of the conserved charge susceptibilities in the ideal quark gas approximation for the temperature range 10 MeV $\leq T \leq$ 100 GeV is shown. It is important to mention that the displayed behavior of the susceptibilities for $T \lesssim 200$ MeV is most likely not realistic, as for temperatures around T_{QCD} and

below we cannot neglect strong interactions and use the ideal quark gas approximation anymore. We just want to reveal the dependence on the quark flavors with this approach. The temperature, at which a quark flavor q starts to contribute to the conserved charge susceptibilities in the ideal quark gas approximation is about $T \gtrsim m_q/12$, see Fig. 6.1. This is quite surprising, as the quark number susceptibility is exponentially suppressed for a large mass $m_q \gg T$ (cf. Eq. (3.24)),

$$\chi_{qq} \sim \left(m_q^3 T\right)^{\frac{1}{2}} \exp\left(-\frac{m_q}{T}\right) \ . \tag{6.19}$$

We particularly want to stress that the charm quark starts to contribute to the conserved charge susceptibilities at around $T \sim 180$ MeV despite its large mass of $m_c = 1275$ MeV. Even though, this is in the temperature regime of the QCD transition, at which the approximation of an ideal quark gas does not hold any longer, this is an important observation. Considering only u, d, s quarks results in vanishing χ_{BQ} for temperatures at which the strange quark is effectively massless, because their total electric charge adds up to zero (cf. Fig. 6.1). This is a significantly different behavior compared to considering u, d, s, c quarks. It raises the question whether lattice QCD simulations should better also consider charm quarks to describe nature around the QCD transition more accurately. Recently, it has also been pointed out by lattice QCD studies that charm quarks start to contribute to the EoS above $T \sim 300$ MeV [92]. In Sec. 7 we will study the effect of charm quarks on the evolution of chemical potentials.

6.2 Lattice QCD Susceptibilities

Quark number and conserved charge susceptibilities and fluctuations for 2+1 flavor QCD are available up to fourth order from lattice QCD methods [108, 127, 128] and selected higher-order susceptibilities and fluctuations are available [94, 129]. We restrict our analyses in the following Chapters to a Taylor series up to second order. Thus, in this Section we compare the to date newest available continuum extrapolated second order conserved charge susceptibilities obtained by the two leading lattice QCD collaborations: the HotQCD collaboration [117] and the Wuppertal-Budapest collaboration [130].

Continuum extrapolated second-order susceptibilities of the Wuppertal-Budapest collaboration are obtained using a stout-improved staggered fermionic action and are available in the temperature range $125 \leq T \leq 400$ MeV [130]. For temperatures larger than $T = 190$ MeV the step size is $10 - 20$ MeV. Whereas for the HotQCD

results, obtained by using the highly improved staggered quark action, the step size is 5 MeV throughout the whole temperature range $150 \leq T \leq 250$ MeV.[18]

Comparing the results of both collaborations in Fig. 6.2, we can see that they approximately agree within errors, with the general tendency of slightly larger susceptibilities obtained by the HotQCD collaboration. Differences can be seen in χ_{BQ}. However, χ_{BQ} is not directly reported by [130] and has to be determined from the reported quark number susceptibilities via (cf. Eqs. (6.14)–(6.16) and [108])

$$\chi_{BQ} = -\frac{1}{2}\left(\chi_{BB} + \chi_{QQ} - \chi_{uu}\right) \ . \tag{6.20}$$

As the errors, obtained via error propagation, are quite large, this yields agreement with the susceptibilities reported by the HotQCD collaboration within errors.

The problem of lattice QCD simulations in going to larger quark numbers, i.e., including additional heavy quarks (charm, bottom, top) at physical masses, is of computational type as the lattice spacing is inversely proportional to the quark mass. In addition, it is difficult to deal with very different mass scales, e.g., the charm quark is about three orders of magnitude heavier compared to the up and down quark.

In the following Chapters we want to compare results obtained by using 2+1 to 2+1+1 flavor lattice QCD susceptibilities. As we only have access to 2+1+1 flavor susceptibilities of the HotQCD collaboration, we will use their susceptibilities for our calculations. Nevertheless, the presented procedure is universal and also other susceptibilities can be used.

[18] Quark number susceptibilities up to $T = 400$ MeV have been studied in [127].

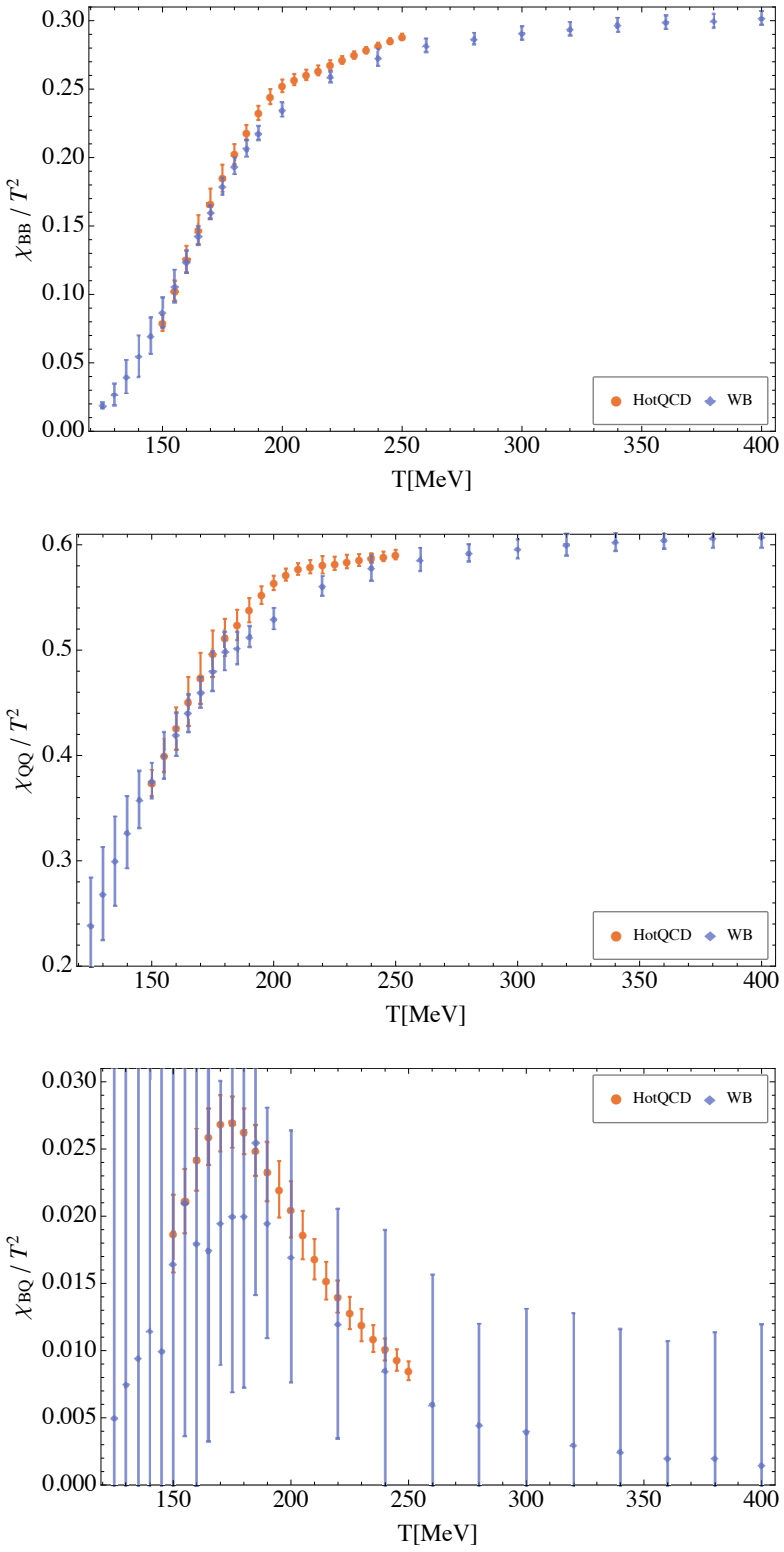

Fig. 6.2: Comparison of second order conserved charge susceptibilities obtained by the HotQCD collaboration [117] and the Wuppertal-Budapest (WB) collaboration [130], with χ_{BQ} of the last-mentioned determined according to Eq. (6.20).

7 Evolution of Chemical Potentials

In this Chapter we present our novel technique of determining the evolution of chemical potentials for arbitrary lepton asymmetries throughout the QCD epoch by using lattice QCD results for conserved charge susceptibilities [1]. Thus, we are able to properly take into account strong interaction effects close to T_{QCD}. In Sec. 7.1 we will discuss the basics of our technique. The evolution of the cosmic trajectory for different lepton asymmetries and in particular the standard cosmic trajectory will be shown in Sec. 7.2. In this Section, we will also discuss different HRG approximations and the effect of unequal lepton flavor asymmetries on the cosmic trajectory. We will comment on a possible consequence of large lepton asymmetries and resulting large electric charge chemical potential, i.e., pion condensation, in Sec. 7.3. In Sec. 7.4 we conclude with the influence of lepton asymmetries on the entropy, energy, and pressure, i.e., on the effective relativistic degrees of freedom in the early universe.

7.1 System of Equations

After the electroweak crossover at $T_{\mathrm{EW}} \sim 100$ GeV and before the onset of neutrino oscillations at $T_{\mathrm{osc}} \sim 10$ MeV, there are five conserved charges in the early universe: B, Q, and the three lepton flavor numbers L_α, with corresponding chemical potentials μ_B, μ_Q, and μ_{L_α}, respectively. In contrast to heavy ion collisions and lattice QCD calculations, individual quark flavors like strangeness are not conserved due to weak processes until $T \sim 1$ MeV, which are in thermal equilibrium in the early universe (cf. Fig. 2.2). We divide our calculations for the determination of the cosmic trajectory in three temperature regimes for which we use different approximations to determine the conserved charges, i.e., define our system of equations:

(i) ideal quark gas approximation ($T \geq 100$ MeV),

(ii) lattice QCD susceptibilities ($250 \geq T \geq 150$ MeV for the 2+1 flavor system and $330 \gtrsim T \gtrsim 150$ MeV for the 2+1+1 flavor system), and

(iii) HRG approximation ($250 \geq T \geq 10$ MeV).

We chose a quite large overlap region for the ideal quark gas and the HRG approximation, down or up to temperatures, where these approximations definitively should fail to describe nature, in order to be able to better estimate the impact of considering strong interactions around T_{QCD}. For all temperatures, we fix $b = 8.71 \times 10^{-11}$ according to [68] and $q = 0$ in agreement with observations. Leptons are considered

in the approximation of free particles, i.e., as an ideal gas of massive leptons, at all temperatures.

Let us describe those three temperature regimes in some more detail in the following.

7.1.1 Ideal Quark Gas Approximation

In kinetic and chemical equilibrium we can calculate the net number densities for an ideal gas of massive particles according to Eq. (3.22). We neglect contributions of the $W^{\pm}$, Z^0, and Higgs bosons, because their contributions are suppressed at the temperature range we are considering in more detail in the following, i.e., $T \leq 400$ MeV. Thus, the five conservation laws for the specific lepton flavor asymmetries l_α, $\alpha \in \{e, \mu, \tau\}$, specific baryon asymmetry b, and electric charge density q can be written in terms of the lepton and quark number densities,

$$l_\alpha s = n_{L_\alpha} = n_\alpha + n_{\nu_\alpha} \ , \tag{7.1a}$$

$$bs = n_B = \frac{1}{3} \sum_{q=u,d,s,c,b,t} n_q \ , \tag{7.1b}$$

$$qs = n_Q = \frac{2}{3} \sum_{q=u,c,t} n_q - \frac{1}{3} \sum_{q=d,s,b} n_q - \sum_{\alpha=e,\mu,\tau} n_\alpha \ . \tag{7.1c}$$

The chemical potentials of all quarks and leptons can be associated with the chemical potentials of the conserved charges in the context of the grand canonical partition function (cf. Eq. (3.1)):

$$\mu_B n_B + \mu_Q n_Q + \sum_\alpha \mu_{L_\alpha} n_{L_\alpha} = \sum_q \mu_q n_q + \sum_l \mu_l n_l \ , \tag{7.2}$$

with on the r.h.s. the sum over all quarks q and leptons $l \in \{\alpha, \nu_\alpha\}$. Inserting the charge densities in terms of the particle net number densities according to Eqs. (7.1a)–(7.1c) and comparing the coefficients in front of the particle net number densities we get

$$\mu_u = \mu_c = \mu_t = \frac{2}{3}\mu_Q + \frac{1}{3}\mu_B \ , \tag{7.3}$$

$$\mu_d = \mu_s = \mu_b = -\frac{1}{3}\mu_Q + \frac{1}{3}\mu_B \ , \tag{7.4}$$

$$\mu_\alpha = \mu_{L_\alpha} - \mu_Q \ , \tag{7.5}$$

$$\mu_{\nu_\alpha} = \mu_{L_\alpha} \ . \tag{7.6}$$

The chemical potentials for quarks of up-type (u, c, t) and down-type (d, s, b) are each the same. Thus, we just have to distinguish between chemical potentials of up-type quarks μ_u and down-type quarks μ_d. Vice versa, we can express the conserved charge chemical potentials in terms of the particle chemical potentials,

$$\mu_{L_\alpha} = \mu_{\nu_\alpha} \ , \tag{7.7}$$

$$\mu_B = \mu_u + 2\mu_d \ , \tag{7.8}$$

$$\mu_Q = \mu_u - \mu_d = \mu_{\nu_\alpha} - \mu_\alpha \ . \tag{7.9}$$

The entropy density $s = s(T, \mu)$ in our system of equations, Eqs. (7.1a)–(7.1c), can be determined according to Eq. (3.34) evaluating the integrals for the net number density, energy density, and pressure for particles in thermal equilibrium given by Eqs. (3.22), (3.25), and (3.26), respectively. We can also use the interpolated pQCD entropy density $s(T, 0)$ for the SM provided by [49], to be able to account for the considerably strong gluonic interactions and add the contribution for nonvanishing chemical potentials calculated as explained before (cf. Sec. 7.4).

7.1.2 QCD Susceptibilities

In order to account for strong interactions, we have to adjust our system of equations, i.e., the calculation of the baryon asymmetry and electric charge density. Only quarks contribute to the baryon asymmetry $bs = n_B^{\mathrm{QCD}}$. And as we neglect interactions between quarks and leptons, the contribution to the electric charge density can be divided into a part arising from the quarks n_Q^{QCD} and one by leptons n_Q^{lep}: $n_Q = n_Q^{\mathrm{QCD}} + n_Q^{\mathrm{lep}}$.[19] With the QCD net number densities given according to Eq. (6.3), our system of equations reads

$$l_\alpha s \quad = n_\alpha + n_{\nu_\alpha} \ , \tag{7.10a}$$

$$bs \quad = \mu_B \chi_{BB} + \mu_Q \chi_{BQ} \ , \tag{7.10b}$$

$$qs \quad = \mu_Q \chi_{QQ} + \mu_B \chi_{BQ} - \sum_\alpha n_\alpha \ . \tag{7.10c}$$

The chemical potentials of the leptons are still given by Eqs. (7.5) and (7.6).

For the numerical evaluation of Eqs. (7.10a)–(7.10c) we use continuum extrapolated lattice QCD susceptibilities for a 2+1 flavor system by [117] and for a 2+1+1

[19] The same holds for the entropy density $s = s^{\mathrm{QCD}} + s^{\mathrm{lep}}$, energy density $\epsilon = \epsilon^{\mathrm{QCD}} + \epsilon^{\mathrm{lep}}$, and pressure $p = p^{\mathrm{QCD}} + p^{\mathrm{lep}}$.

flavor system (not continuum extrapolated, $N_\tau = 8$) by [119, 131]. We determine numerical temperature derivatives of the susceptibilities for the calculation of $s^{\mathrm{QCD}}(T,\mu)$ according to Eq. (6.6). The entropy density at vanishing chemical potentials $s(T,0)$ is taken from [49]. The leptonic contribution to the entropy density at nonvanishing chemical potentials is calculated in the ideal gas approximation as for high temperatures.

The error of the results has been naively estimated by solving our system of equations in Eqs. (7.10a)–(7.10c) for accounting for the error of the lattice QCD susceptibilities, i.e., for $\chi+\Delta\chi$ and $\chi-\Delta\chi$ with the reported errors by [117, 119, 131] (cf. App. A.2). These results then yield the estimated error for our evolution of the chemical potentials obtained by using lattice QCD susceptibilities.

7.1.3 HRG Approximation

At relatively low temperatures we use the hadron resonance gas model to approximate the QCD sector. Thus, now hadrons, i.e., baryons and mesons, and hadron resonances contribute to the baryon asymmetry and electric charge densities. Our system of equations becomes

$$l_\alpha s = n_\alpha + n_{\nu_\alpha} \ , \tag{7.11a}$$

$$bs = \sum_{\text{baryons}} n_b \ , \tag{7.11b}$$

$$qs = \sum_{\text{baryons}} Q_b n_b + \sum_{\text{mesons}} Q_m n_m - \sum_\alpha n_\alpha \ , \tag{7.11c}$$

with Q_b and Q_m the electric charge of a baryon and a meson, respectively.

The chemical potentials of baryons and mesons can be obtained in analogy to Sec. 7.1.1:

$$\mu_b = \mu_B + Q_b \mu_Q \ , \tag{7.12}$$

$$\mu_m = Q_m \mu_Q \ . \tag{7.13}$$

For instance, the chemical potential of the neutron is $\mu_n = \mu_B$, the chemical potential of the proton is $\mu_p = \mu_B + \mu_Q$, and the chemical potential of the charged pion is $\mu_\pi = \mu_Q$. The lepton chemical potentials are again given by Eqs. (7.5) and (7.6). The conserved charge chemical potentials can then be expressed as

$$\mu_{L_\alpha} = \mu_{\nu_\alpha} \ , \tag{7.14}$$

$$\mu_B = \mu_n \ , \tag{7.15}$$

$$\mu_Q = \mu_\pi = \mu_p - \mu_n = \mu_{\nu_\alpha} - \mu_\alpha \ . \tag{7.16}$$

The entropy density $s = s(T, \mu)$ is determined according to Eq. (3.34) evaluating the integrals for the net number density, energy density, and pressure for particles in thermal equilibrium given by Eqs. (3.22), (3.25), and (3.26), respectively, and summing over all particles and hadron resonances.

7.1.4 Calculational Details

For a given temperature the free variables in our systems of equations are the chemical potentials in the particle net number densities $n_i(T, \mu_i)$ or rather the five conserved charge chemical potentials and the specific lepton flavor asymmetries l_α. By fixing l_α we can determine the evolution of the chemical potentials. Integrations like in the determination of the particle densities according to Eq. (3.22) are performed using Gauss-Laguerre quadrature. The system of equations is solved by using Broyden's method [132], which is a modification of Newton's method to solve a nonlinear system of equations. For solving our system of integral-equations, we are free to choose arbitrarily five independent chemical potentials as free parameters according to the relations between conserved charge and particle chemical potentials. However, one has to carefully choose them such that they are of different size to be able to obtain all particle chemical potentials without running into numerical problems. This is most important for the HRG at low temperatures where $\mu_Q = \mu_p - \mu_n$ and $\mu_n \approx \mu_p$. A good choice for all temperatures is $\{\mu_Q, \mu_B, \mu_{L_e}, \mu_{L_\mu}, \mu_{L_\tau}\}$. For the HRG approximation we consider hadron resonances up to $m_{\Lambda(2350)} \approx 2350\,\text{MeV} \sim 15 T_{\text{QCD}}$, using particle properties according to the summary tables of the Particle Data Group [3]. A detailed list of the properties of all hadrons and resonances included in our numerical evaluation of Eqs. (7.11a)–(7.11c) can be found in App. A.4.

The numerical determination of the evolution of the charge chemical potentials is based on the `C` code used in [2]. Mistakes in the determination of the particle densities and entropy density in the original code have been corrected. The particle properties were updated, corrected, and the number of included hadron resonances has been enlarged from 54 to in total 239 hadron resonances (96 meson and 143 baryon resonances). Furthermore, we implemented the possibility of using lattice QCD results in the code and self-consistently included chemical potentials in our system of equations, i.e., in the particle net number densities and in the entropy density.

Deviations of our results for the evolution of the chemical potentials from the results in [2] are due to these improvements.

7.2 Cosmic Trajectory

In this Section we present numerical solutions for our systems of equations discussed before, i.e., the results for the temperature evolution of the chemical potentials of the five conserved charges, μ_B, μ_Q, μ_{L_e}, μ_{L_μ}, and μ_{L_τ}. One should keep in mind that the cosmic trajectory follows a path in the 5+1-dimensional phase diagram of these five chemical potentials and temperature. In the following, we will show two-dimensional projections of this phase diagram. For $l = -(51/28)b$ and $l_\alpha = l/3$ we obtain the standard cosmic trajectory accounting properly for strong interaction effects around T_{QCD}. We will assume equal lepton flavor asymmetries, $l_\alpha = l/3$, except for Sec. 7.2.5 where we will discuss the effect of unequal lepton flavor asymmetries on the evolution of the chemical potentials. But in all cases, we will consider a total lepton asymmetry which is in agreement with observational bounds, $|l| \lesssim 0.012$ [18].

7.2.1 Baryon Chemical Potential

The result for the temperature evolution of the baryon chemical potential for different negative values of the total lepton asymmetry is shown in Fig. 7.1 (top) and a zoom on the standard cosmic trajectory in the (μ_B, T) plane is shown (bottom). Talking about absolute values, we can see in Fig. 7.1 that a larger total lepton asymmetry induces a larger baryon chemical potential. In addition, we see that μ_B is proportional to l. This is true as long as $l > \mathcal{O}(b)$. For lepton asymmetries $l \lesssim \mathcal{O}(b)$ the evolution of μ_B is determined by the baryon asymmetry b, and the influence of l is negligible. In the following Sections we will see that this general dependence on the total lepton asymmetry is the same for all conserved charge chemical potentials.

The chemical potentials obtained using lattice QCD susceptibilities connect the ideal quark gas with the HRG approximation quite well for different orders of magnitude of l. Without the lattice QCD results, there would be a nonphysical gap between the ideal quark gas and HRG results for $l > \mathcal{O}(b)$. This reflects the need of considering strong interactions via, e.g., including lattice QCD susceptibilities to obtain the cosmic trajectory. However, the results with 2+1 flavor lattice QCD susceptibilities do not connect the two approximations smoothly for $l > \mathcal{O}(b)$. At low temperatures a small gap between the HRG and lattice QCD results exists. At high temperatures the lattice QCD results do not smoothly converge to the ideal quark gas, but they intersect in a single point for $l \gtrsim 10^{-8}$. This might be a hint to a first-order phase transition, which would be reflected in a kink in the temperature evolution of the chemical potential (cf. Sec. 3.4). However, taking into account the charm quark by using 2+1+1 flavor lattice QCD susceptibilities, the lattice QCD

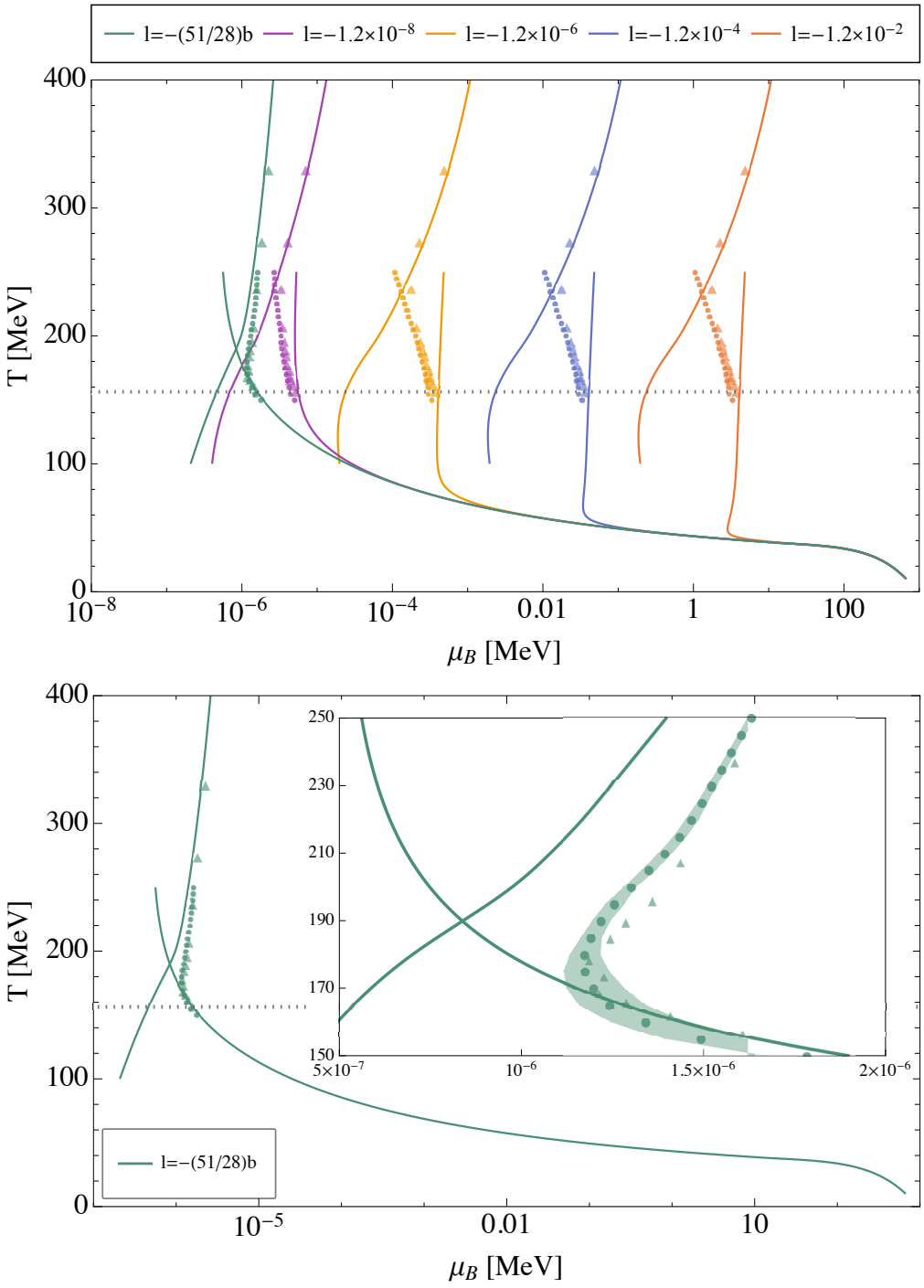

Fig. 7.1: Temperature evolution of baryon chemical potential for different negative total lepton asymmetries l (top) and a zoom on the standard cosmic trajectory of the early universe (bottom). Continuous lines for high temperatures are results for the ideal quark gas, for low temperatures for the HRG. The symbols • and ▲ indicate results obtained using 2+1 flavor and 2+1+1 flavor lattice QCD susceptibilities, respectively. $T_{\mathrm{QCD}} = 156.5$ MeV is displayed by a horizontal dotted line. In the lower diagram the error band of results obtained with 2+1 flavor lattice QCD susceptibilities is shown. In the upper diagram and for the 2+1+1 flavor results in the lower diagram the errors are approximately on the size of the symbols.

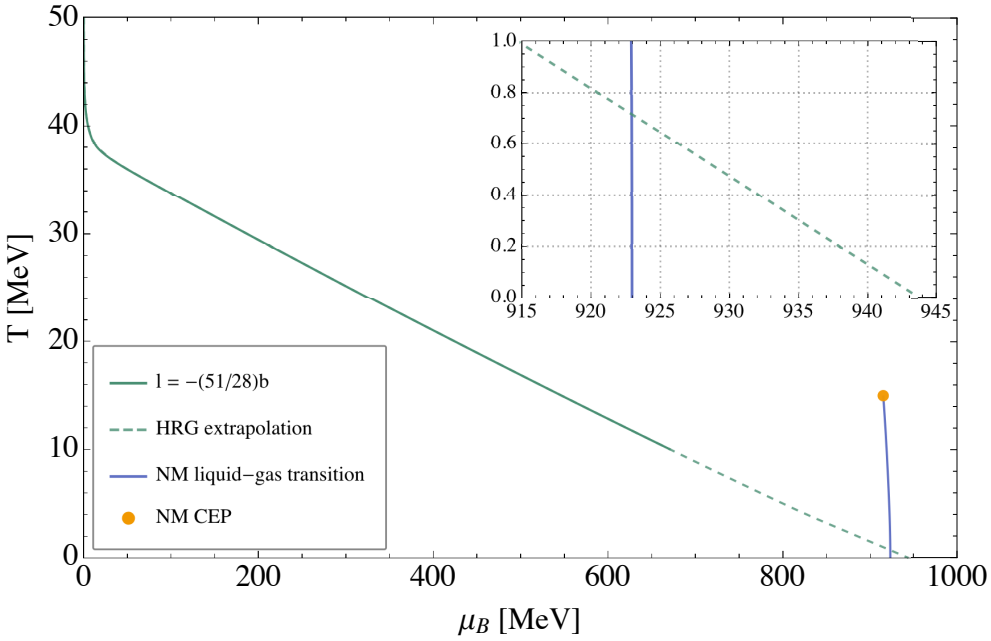

Fig. 7.2: Standard cosmic trajectory in the (μ_B, T) plane in the HRG approximation and its extrapolation to $T = 0$. Also shown is the first-order liquid-gas transition of nuclear matter (NM liquid-gas transition) and the critical endpoint of this transition (NM CEP) in this plane according to [95].

results seem to converge to the ideal quark gas results at high temperatures without a kink, see Fig. 7.1 (top). The estimated uncertainty of the lattice QCD results is on the order of the point sizes in Fig. 7.1. The error band of the 2+1 flavor lattice QCD results is shown for the standard cosmic trajectory in the zoom in Fig. 7.1 (bottom). For the standard cosmic trajectory we see a good match of the lattice QCD and HRG results within errors at low temperatures. At temperatures $T \sim T_{\mathrm{QCD}}$ we see a gap between the lattice and ideal quark gas results, which reflects the importance of strong interaction effects around T_{QCD}. For high temperatures lattice QCD and ideal quark gas results agree quite well within the errors .

An important feature in the evolution of μ_B is that for small temperatures $T \lesssim m_\pi/3 \approx 46$ MeV, after the annihilation of pions and muons, μ_B no longer depends on the value of l but follows one trajectory (cf. Fig. 7.1(top)). At low temperatures μ_B approaches the nucleon mass $m_N \sim 1$ GeV. In Fig. 7.2 a naive extrapolation of the HRG to low temperatures $T < 10$ MeV is shown. In this extrapolation $\mu_B(T = 0) \approx 944$ MeV. We also show the first-order liquid-gas transition of nuclear matter according to [95] in the (μ_B, T) plane in Fig. 7.2. In case of the naive extrapolation of our HRG result, it looks as if the cosmic trajectory passes through

this liquid-gas transition of nuclear matter and the matter in the early universe underwent this first-order transition at $T < 1$ MeV. However, we cannot use our technique for $T \lesssim 10$ MeV. One has to consider neutrino flavor oscillations, which become active at these temperatures, under which the individual lepton flavors are not conserved anymore and our system of equations changes. The cosmic trajectory then follows a path in the 3+1-dimensional phase diagram of the three conserved charges, i.e., B, Q, total lepton number L, and temperature. Furthermore, for $T \lesssim 1$ MeV weak interactions are not in equilibrium any longer and we cannot use our technique, for which thermal equilibrium of all particles is needed. Thus, whether the universe passes the first-order liquid-gas transition of nuclear matter or not, and what consequences this might have, has to be analyzed in a refined study.

7.2.2 Electric Charge Chemical Potential

In Fig. 7.3 the temperature evolution of the electric charge chemical potential $-\mu_Q$ is shown for different negative total lepton asymmetries. As in the case of μ_B, a larger total lepton asymmetry induces a larger absolute value of the electric charge chemical potential and $\mu_Q \propto l$ for $l > \mathcal{O}(b)$ and $\mu_Q \propto b$ for $l \lesssim \mathcal{O}(b)$. The chemical potentials obtained using lattice QCD susceptibilities (2+1 and 2+1+1 flavor) almost smoothly connect the ideal quark gas with the HRG results. In the zoom on the standard cosmic trajectory of μ_Q in Fig. 7.3 (bottom) we see a small gap between the lattice QCD results and the ideal quark gas results at high temperatures. However, estimating the error of $s(T, 0)$ by pQCD, which we do not show but which is quite large at relatively low temperatures (cf. e.g. [102]), and the error of the lattice results, which is on the order of the point sizes in Fig. 7.3 (bottom), the results should agree within errors. At low temperatures, the HRG and 2+1 flavor lattice results do not match well in the standard scenario, whereas the 2+1+1 flavor lattice results match better. At larger lepton asymmetries, however, the lattice results converge better to the HRG approximation. This might be due to limitations of the HRG model. It would be helpful to have lattice QCD susceptibilities for lower temperatures and continuum extrapolated 2+1+1 flavor susceptibilities available, to see if these gaps then might be closed.

Figure 7.4 shows the effect of the sign of a lepton asymmetry. We can see, that the sign of the total lepton asymmetry mainly changes the sign and not the absolute value or the evolution of the chemical potentials. For negative l, μ_Q is negative and μ_B is positive and vice versa for positive l. However, at low temperatures μ_B proceeds to the nucleon mass irrespective of the sign of the lepton asymmetry.

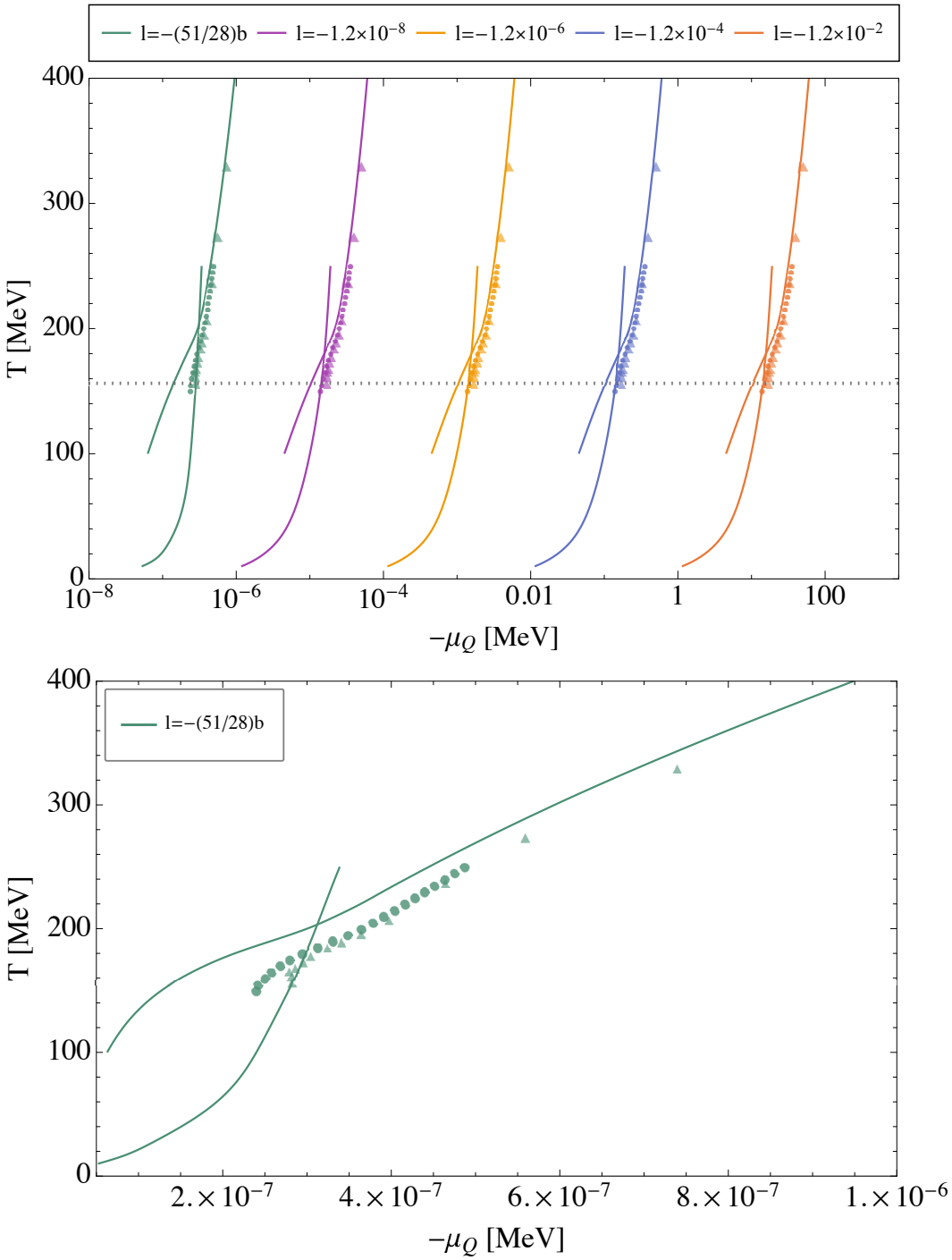

Fig. 7.3: Temperature evolution of electric charge chemical potential $-\mu_Q$ for different negative total lepton asymmetries l (top) and a zoom on the standard cosmic trajectory of the early universe (bottom). Continuous lines for high temperatures are results for the ideal quark gas, for low temperatures for the HRG. The symbols • and ▲ indicate results obtained using 2+1 flavor and 2+1+1 flavor lattice QCD susceptibilities, respectively. $T_{\mathrm{QCD}} = 156.5$ MeV is displayed by a horizontal dotted line. The errors of the results obtained with lattice QCD susceptibilities are approximately on the size of the symbols in the lower diagram and half of the size of the symbols in the upper diagram.

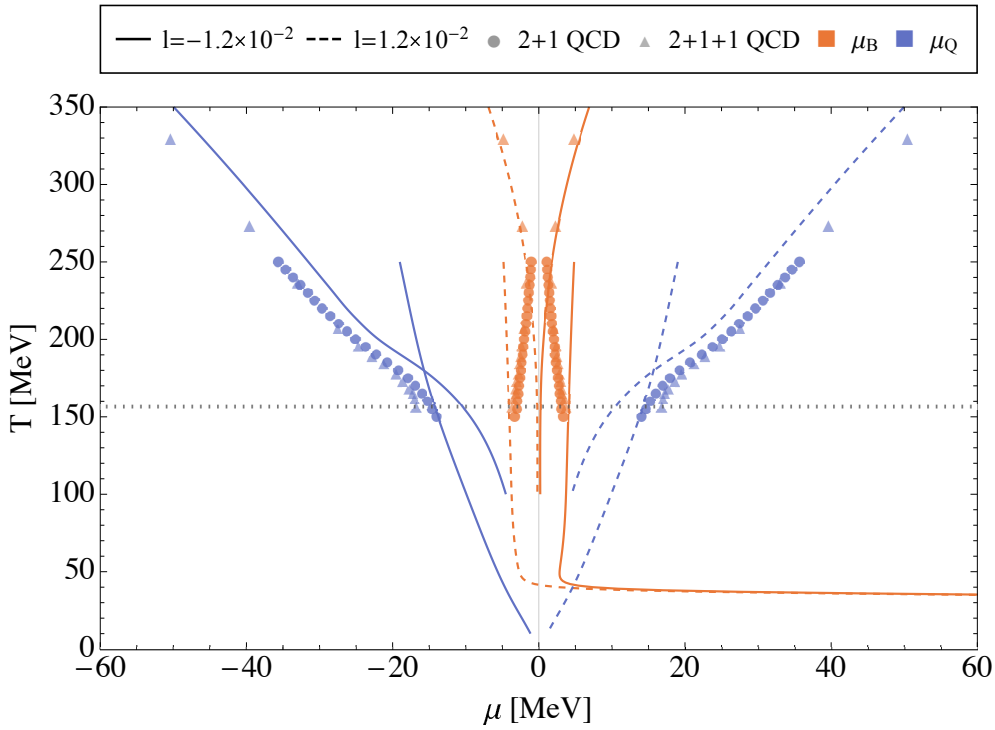

Fig. 7.4: Temperature evolution of baryon chemical potential μ_B and electric charge chemical potential μ_Q for both signs of a large lepton asymmetry $|l| = 1.2 \times 10^{-2}$. Continuous and dashed lines for high temperatures are results for the ideal quark gas, for low temperatures for the HRG.

Comparing Fig. 7.1 to Fig. 7.3, and looking at Fig. 7.4 it can be seen that, for large lepton asymmetries $l > \mathcal{O}(b)$, the absolute value of μ_Q becomes larger than μ_B at nonvanishing temperature. This can be understood in the following way. As already discussed in Sec. 6.1, the electric charges of the three light quarks add up to zero. In the case of only three mass degenerate quarks the susceptibility χ_{BQ} would vanish, so that no μ_B is induced. Thus, μ_B remains small for $T \gtrsim m_s$ (cf. evolution of χ_{BQ} in Fig. 6.1). As mentioned, this is why the charm quark is important for the evolution of μ_B, despite its large mass.

A possible consequence of a large electric charge chemical potential in the early universe, i.e., pion condensation, will be discussed in Sec. 7.3.

7.2.3 Lepton Flavor Chemical Potentials

Figures 7.5 and 7.6 show the temperature evolution of the lepton flavor chemical potentials for different orders of magnitude of the total lepton asymmetry and a

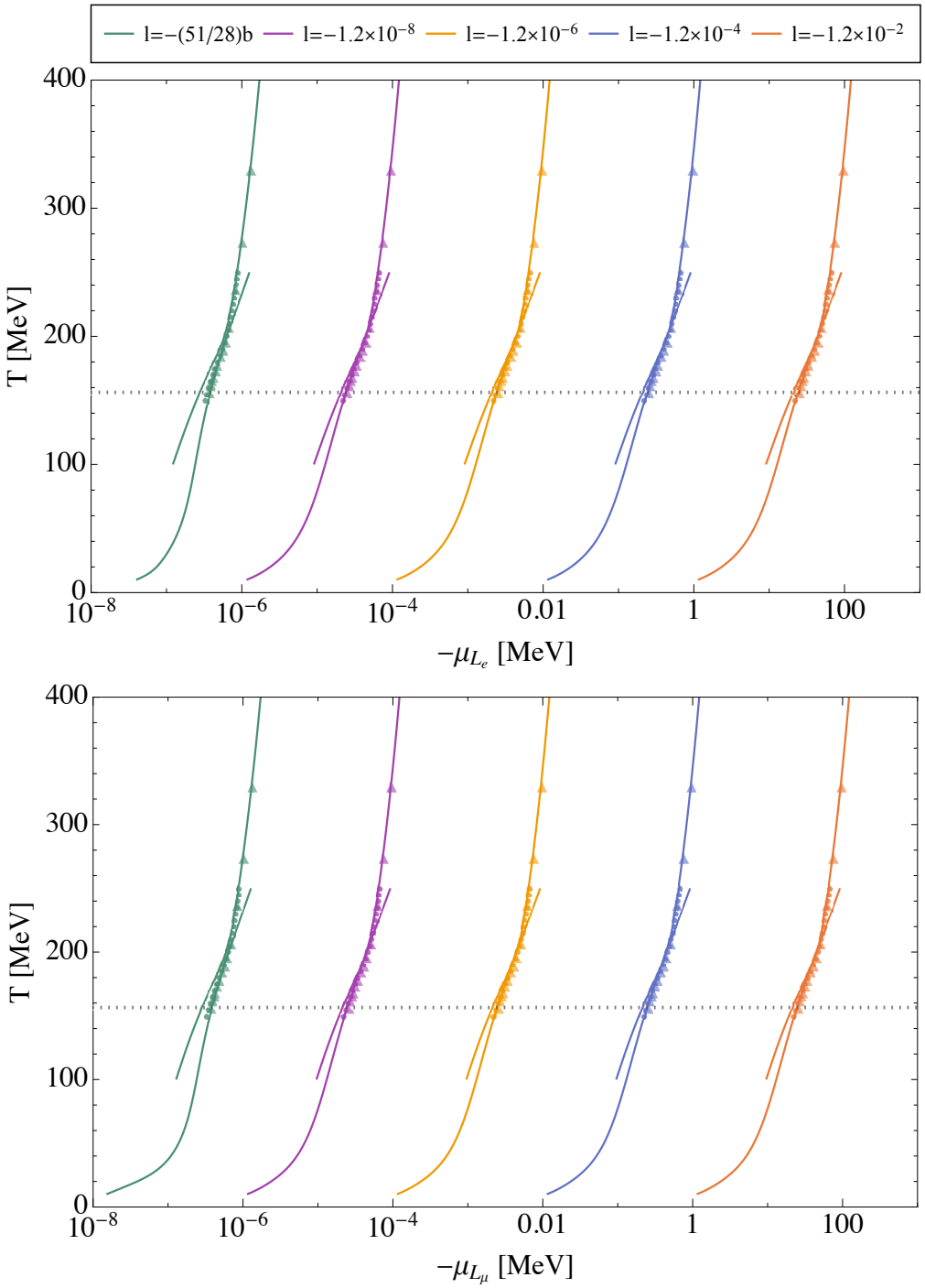

Fig. 7.5: Temperature evolution of electron (top) and muon (bottom) lepton flavor chemical potential for different negative total lepton asymmetries l. Continuous lines for high temperatures are results for the ideal quark gas, for low temperatures for the HRG. The symbols • and ▲ indicate results obtained using 2+1 flavor and 2+1+1 flavor lattice QCD susceptibilities, respectively. $T_{\mathrm{QCD}} = 156.5$ MeV is displayed by a horizontal dotted line. The errors of the results obtained with lattice QCD susceptibilities are approximately half of the size of the symbols in both diagrams.

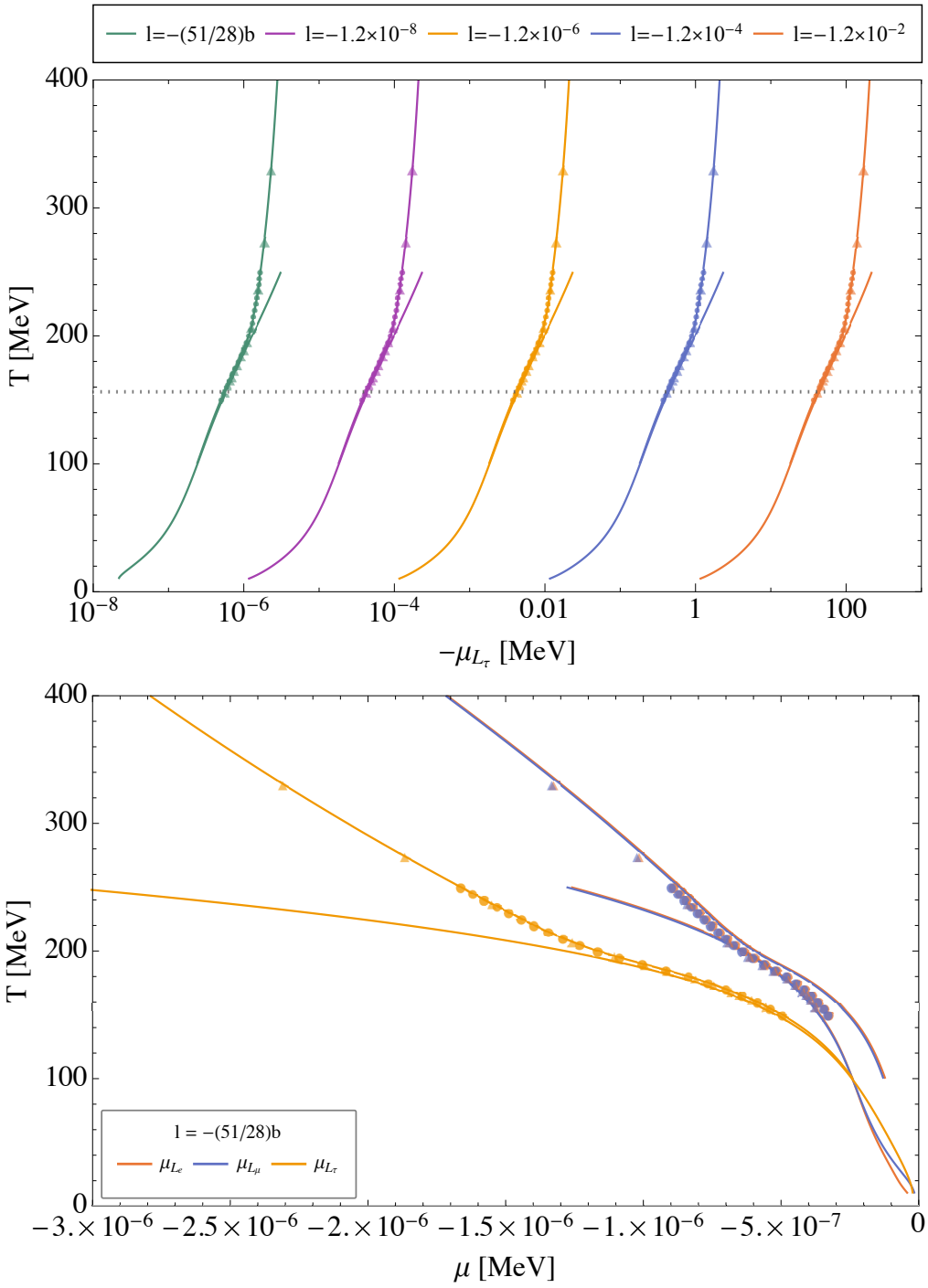

Fig. 7.6: Temperature evolution of tau lepton flavor chemical potential for different negative total lepton asymmetries l (top) and a zoom on the standard cosmic trajectory of the early universe for all lepton flavor chemical potentials (bottom). The errors of the results obtained with lattice QCD susceptibilities are approximately on the size of the symbols in the lower diagram and half of the size of the symbols in the upper diagram. Notations as before.

zoom on the standard cosmic trajectory for all lepton flavors in Fig. 7.6 (bottom). As before, in terms of absolute values, a larger lepton asymmetry induces larger chemical potentials. The chemical potentials are proportional to l for $l > \mathcal{O}(b)$. For all lepton flavor chemical potentials, the results obtained with lattice QCD susceptibilities (2+1 and 2+1+1 flavor) match with the results obtained in the HRG and ideal quark gas and interpolate between them. Gaps between the lattice QCD results and ideal quark gas reported in [1] were closed by taking higher-order perturbative corrections into account, using the interpolated pQCD entropy density $s(T, 0)$ by [49] in the temperature regime of the ideal quark gas approximation.

Notwithstanding equal lepton flavor asymmetries l_α for all flavors, the different lepton flavor chemical potentials evolve differently due to the different lepton masses. However, μ_{L_e} and μ_{L_μ} evolve very similar, especially at high temperatures where electrons and muons are both effectively massless. Having a closer look at the zoom on the standard cosmic trajectory in Fig. 7.6 (bottom), we see that at low temperatures μ_{L_μ} evolves differently compared to μ_{L_e}. This is due to the fact that the muon is about 200 times as heavy as the electron and it becomes nonrelativistic and, finally, annihilates at higher temperatures compared to the electron. The effect of the heavy mass is also the reason why the evolution of μ_{L_τ} is different compared to μ_{L_e} and μ_{L_μ}. Tau leptons are nonrelativistic at all temperatures we are considering. In particular, tau leptons annihilate well above T_{QCD} at $T_{\mathrm{ann},\tau} \sim 600$ MeV. This leads to another interesting feature, namely the (partial) decoupling of the tau lepton flavor conservation equation from the system of equations (it is still coupled via $s(T, \mu)$). Due to this (partial) decoupling, the trajectories of the ideal quark gas and HRG match without the need of lattice susceptibilities, the perturbative consideration of strong effects in $s(T, 0)$ suffices in the case of μ_{L_τ} (cf. Fig. 7.6).[20]

7.2.4 Comparison of Different HRG Approximations

In the code of [2] hadron resonances up to $m_{K_0^*(1410)} \approx 1421$ MeV $\sim 9T_{\mathrm{QCD}}$ (38 meson and 16 baryon resonances) have been considered. We included additional 185 hadron resonances (58 meson and 127 baryon resonances). In Fig. 7.7 we show the evolution of the baryon chemical potential for three different HRG approximations: (i) including only protons, neutrons, and pions, (ii) including resonances up to $m_{K_0^*(1410)}$, and (iii) the HRG used in this work including resonances up to $m_{\Lambda(2350)}$. The changes in μ_Q and μ_{L_α} due to different HRG approximations are visible but not

[20] However, for lepton (flavor) asymmetries orders of magnitude larger than we considered here this might be different, as larger lepton asymmetries induce larger chemical potentials and, thus, a larger change in the entropy density $s(T, \mu)$.

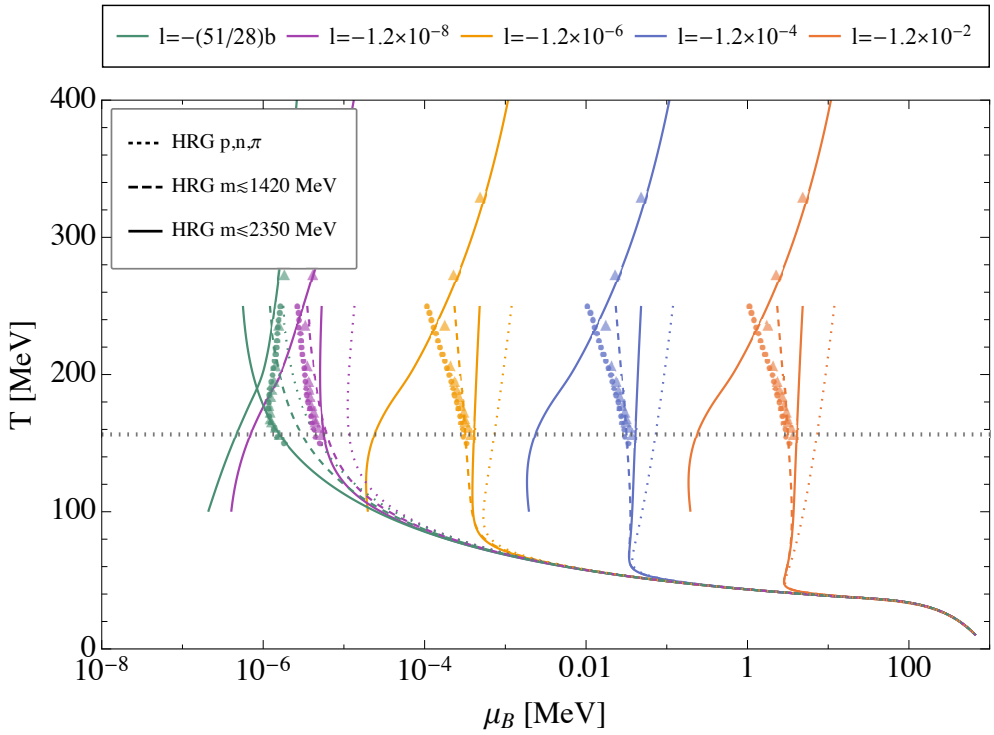

Fig. 7.7: Temperature evolution of baryon chemical potential μ_B for different HRG approximations at different negative total lepton asymmetries l. Continuous lines for high temperatures are results for the ideal quark gas, for low temperatures for the HRG including resonances up to $m_{\Lambda(2350)} \approx 2350$ MeV $\sim 15 T_{\mathrm{QCD}}$. Dashed lines are results for the HRG including resonances up to $m_{K_0^*(1410)} \approx 1421$ MeV $\sim 9 T_{\mathrm{QCD}}$. Dotted lines are results for the HRG including only proton, neutrons, and pions. Further notations as before.

as strong as in μ_B. At relatively low temperatures, the temperature evolution of μ_B does not depend on the specific HRG approximation but follows one trajectory and proceeds to the nucleon mass, as all heavier hadrons annihilated (cf. Sec. 7.2.1). For temperatures $T \gtrsim 80$ MeV, we can strongly see the dependence of the temperature evolution of μ_B on the particular HRG approximation. Especially the additional baryon resonances in the HRG with masses up to $m_{\Lambda(2350)}$ change the evolution of μ_B in the HRG approximation at these relatively high temperatures due to their large spin degrees of freedom, despite their large masses. Regarding the standard cosmic trajectory, the trajectory with the HRG we used in this work matches the results obtained with lattice susceptibilities quite well (see also the zoom on the standard cosmic trajectory in Fig. 7.1). The standard trajectories obtained with the other HRG approximations, on the other hand, fail to match the results obtained with lattice susceptibilities. The good agreement of an HRG with masses up to

$m \sim 2$ GeV with lattice QCD at vanishing chemical potentials is also expected by comparative studies of lattice QCD and HRG (cf. Sec. 5.4) and it has been shown that this agreement is insensitive to possible higher resonances [118].

7.2.5 Unequal Lepton Flavor Asymmetries

Until now, we just considered equal lepton flavor asymmetries for all flavors. In this Section, we will consider different, i.e., unequal, lepton flavor asymmetries in agreement with BBN and CMB limits discussed in Sec. 4.1: $|l| \lesssim 0.012$ as before and $|l_e| \lesssim 0.004$ and $|l_{\mu,\tau}| \lesssim 0.021$. Additionally, we will have a look at an extreme case of $l_e = 0$ and $l_\mu = -0.1 = -l_\tau$. In general, one could also assume very large lepton flavor asymmetries, e.g., $|l_e| = 0.1$, while the total lepton asymmetry is in agreement with the observational constraint $|l| \lesssim 0.012$. Efficient neutrino oscillations at $T \lesssim 10$ MeV lead to lepton flavor chemical potentials in agreement with constraints of BBN and the CMB.

In Fig. 7.8 we show the temperature evolution of the conserved charge chemical potentials for different cases of unequal lepton flavor asymmetries. For comparison, we also show the evolution for equal lepton flavor asymmetries with the maximal, observationally permitted total lepton asymmetry $l = -1.2 \times 10^{-2}$, which we already discussed in the previous Sections. In general, with unequal lepton flavor asymmetries larger conserved charge chemical potentials can be obtained. Furthermore, different lepton flavor asymmetries yield considerably different evolutions of the three lepton flavor chemical potentials, concerning not only absolute value or size [cf. Fig. 7.8 (middle & bottom left)]. This is especially true in the case of $l_e = 0$ and $l_\mu = -0.1 = -l_\tau$. There we can also see larger discrepancies between ideal quark gas or HRG results and the lattice QCD results, respectively. These discrepancies may be due to limitations of our technique at such large lepton flavor asymmetries, especially limitations of the Taylor series ansatz for the QCD pressure (cf. Chapter 8 and especially Sec. 8.3).

In particular, with unequal lepton flavor asymmetries we can reach larger electric charge and baryon chemical potentials, shifting the cosmic trajectory towards a possible critical endpoint or first-order phase transition of QCD.

Large chemical potentials lead, according to Eq. (3.36), to a larger number of effective relativistic degrees of freedom $g_{*s}(T, \mu)$. We can see in Fig. 7.8 that this change is quite large for unequal lepton flavor asymmetries, as they induce larger chemical potentials compared to equal lepton flavor asymmetries while being in agreement with observational constraints. More details will be discussed in Sec. 7.4.

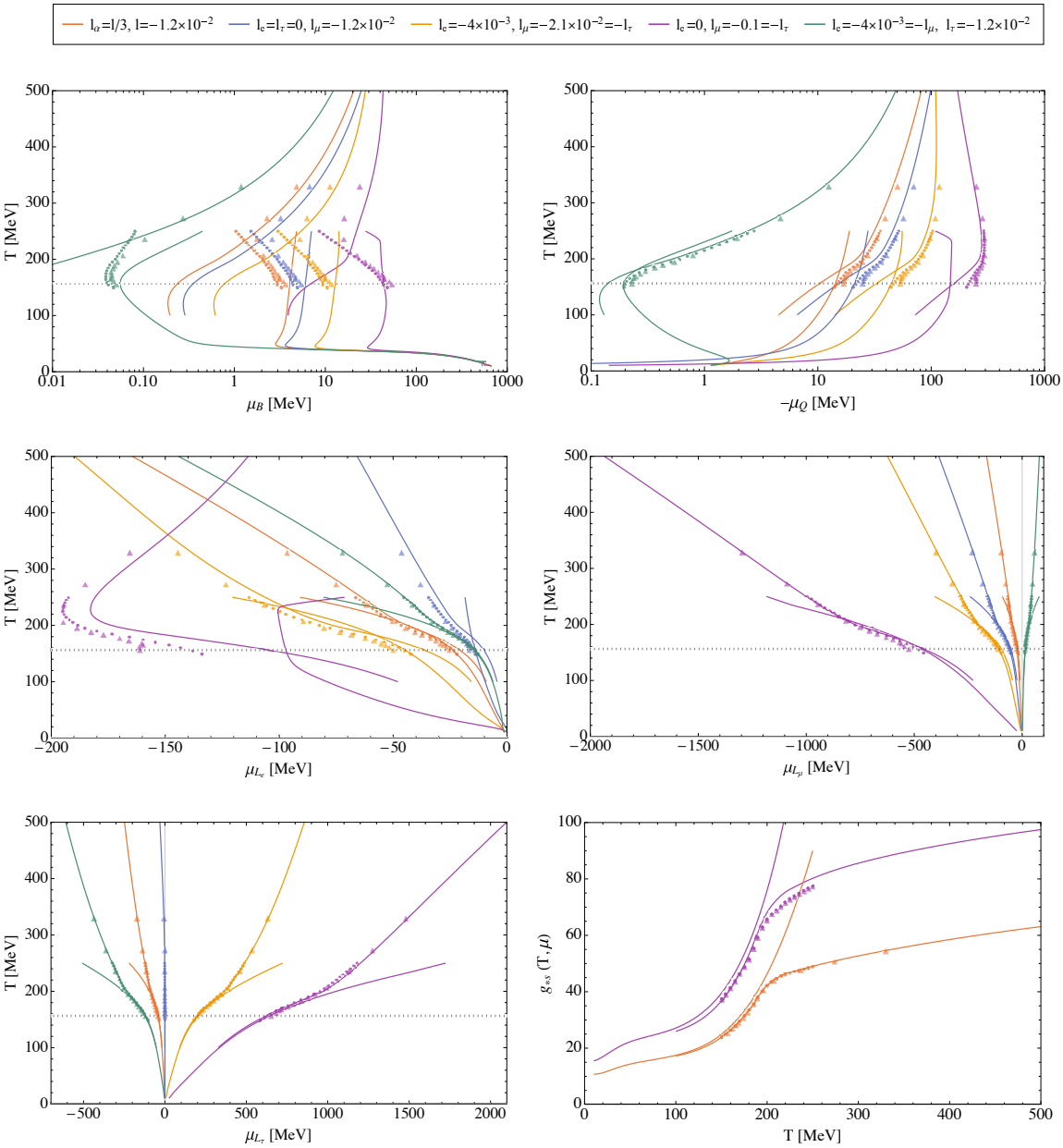

Fig. 7.8: Temperature evolution of conserved charge chemical potentials for different cases of unequal lepton flavor asymmetries. (Top left) Baryon chemical potential μ_B. (Top right) Electric charge chemical potential $-\mu_Q$. (Middle left) Electron lepton flavor chemical potential μ_{L_e}. (Middle right) Muon lepton flavor chemical potential μ_{L_μ}. (Bottom left) Tau lepton flavor chemical potential μ_{L_τ}. (Bottom right) Effective relativistic degrees of freedom $g_{*s}(T, \mu)$ for equal $l = -1.2 \times 10^{-2}$ and unequal lepton flavor asymmetries $l_e = 0$, $l_\mu = -0.1 = -l_\tau$. Notations as before.

7.3 Pion condensation

We saw in Sec. 7.2.2 that the absolute value of the electric charge chemical potential exceeds the baryon chemical potential at nonvanishing temperature and, thus, might be (more) important for the evolution of the early universe. An example for the importance of the electric charge chemical potential is that, for μ_Q larger than the pion mass $m_\pi \approx 140$ MeV a Bose-Einstein condensate of charged pions is formed. This has been studied in the Nambu–Jona-Lasinio model in the presence of a dense neutrino gas, i.e., at nonvanishing lepton asymmetries, at vanishing temperature (with estimates for higher temperatures) in [35]. Using lattice QCD methods at vanishing μ_B, pion condensation was observed for $T \lesssim 160$ MeV [36]. In this study nonvanishing isospin chemical potential was investigated.[21] The isospin chemical potential is the same as the pion chemical potential, $\mu_I = \mu_\pi$, which is for a system of conserved electric charge the same as the electric charge chemical potential, $\mu_Q = \mu_\pi$.[22] A possible result of pion condensation might be pion stars, a new class of compact stars in the universe [52]. Isospin chemical potential is also studied in lattice QCD as lattice QCD calculations at pure isospin, i.e., $\mu_I \neq 0$ and $\mu_B = 0$, do not suffer from a sign problem but share some technical features with QCD at finite baryon chemical potential (cf. [134, 135]).

We can use our technique for determining the lepton asymmetry which is needed to reach $|\mu_Q| \geq m_\pi$ at $T \lesssim 160$ MeV. As we obtained quite good agreement of lattice results with HRG results in μ_Q for $T \lesssim T_{\mathrm{QCD}}$ (cf. Fig. 7.3), we use the HRG approximation to study the evolution of the electric charge chemical potential for pion condensation. Considering equal lepton flavor asymmetries $l_\alpha = l/3$, we find that for $|l| \gtrsim 0.12$ we get $|\mu_Q| \gtrsim m_\pi$ at nonvanishing temperatures (see Fig. 7.9). Such a large total lepton asymmetry, however, exceeds the observational constraints by an order of magnitude. Assuming unequal lepton flavor asymmetries, we can reach the region of pion condensation, while satisfying $|l| \lesssim 0.012$. One example is $l_e = 0$ and $l_\mu = -0.1 = -l_\tau$ which we already studied in Sec. 7.2.5. In this case we get $|\mu_Q| \geq m_\pi$ for temperatures $T \gtrsim 125$ MeV (see Fig. 7.9). For small temperatures, μ_Q tends to vanish for this example due to assumed charge neutrality, since $l_e = 0$ and muons annihilate at low temperatures, thus, $l_\mu = l_{\nu_\mu}$ and $l_\tau = l_{\nu_\tau}$.

[21] Due to the unusual definition of the isospin in this study, i.e., $n_I = n_u - n_d$, the pion condensation forms at $|\mu_I| \geq m_\pi/2$. The common definition of isospin is, however, $n_I = (n_u - n_d)/2$, which exactly yield the factor 1/2 difference to other studies.

[22] A nice discussion about relations between susceptibilities and chemical potentials in ensembles of different conserved charges can be found in [133].

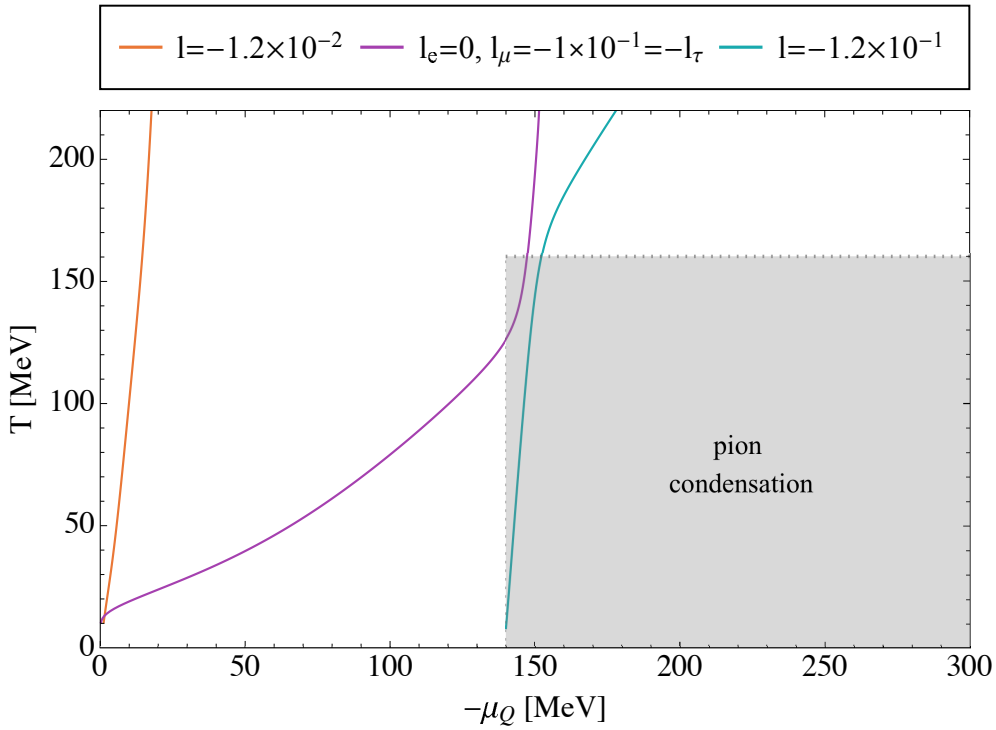

Fig. 7.9: Temperature evolution of electric charge chemical potential $-\mu_Q$ in the HRG approximation for different lepton flavor asymmetries. For equal lepton flavor asymmetries consistent with observational constraints, $l = -1.2 \times 10^{-2}$, the region of pion condensation cannot be reached. For a total lepton asymmetry which is one order of magnitude larger, $|\mu_Q| \geq m_\pi$ for nonvanishing temperatures so that pion condensation might occur (cf. [36]). Considering unequal lepton flavor asymmetries, the region of pion condensation can be reached in keeping with observational constraints on the total lepton asymmetry.

We considered pion condensation in the (μ_Q, T) plane, hence neglected the size of μ_B and other chemical potentials, so far. However, nonvanishing chemical potentials influence the possibility of pion condensation. In general, for finite μ_B and other chemical potentials, due to plasma interactions, a larger electric charge chemical potential is needed to form a pion condensate. Additionally, the temperature at which pion condensation occurs may be decreased leading to a shrinking region of pion condensation (cf. [36, 136]). Furthermore, in [27] it is discussed that a pion condensate would form for $|\mu_Q| \geq m_\pi$ only in the case of $|\mu_B| < m_p - m_\pi$. For $-\mu_Q \sim m_\pi$ and $\mu_B \gtrsim m_p$ a negatively charged kaon condensate turns out to be more likely to occur in dense nuclear matter, as the kaon mass is decreased by an attractive interaction [137, 138]. For lepton (flavor) asymmetries required for pion condensation, μ_B is not vanishingly small (cf. Fig. 7.8) and proceeds to the nucleon

mass for $T \lesssim m_\pi/3$. Thus, our results reflect a lower limit on the lepton asymmetries needed for pion condensation. A refined lattice QCD study at nonvanishing isospin (or electric charge) and baryon chemical potentials is needed, to be able to discuss the possibility of pion condensation in the early universe more appropriately.

7.4 Evolution of Entropy, Energy and Pressure

Large lepton asymmetries change the entropy density, energy density, and pressure due to nonvanishing chemical potentials (cf. Sec. 3.2). The change in $s(T,\mu)$, $\epsilon(T,\mu)$, and $p(T,\mu)$ can numerically be determined according to Eqs. (3.34), (3.25), and (3.26), respectively. In Fig. 7.10 their temperature evolution for different negative total lepton asymmetries l and equal lepton flavor asymmetries $l_\alpha = l/3$ is shown. We can see that the change in the entropy density, energy density and pressure due to nonvanishing lepton asymmetries is rather small in the case of equal lepton flavor asymmetries and a total lepton asymmetry in agreement with observational bounds, $|l| \lesssim 0.012$. One can only distinguish the results for $l = -1.2 \times 10^{-2}$ from the standard scenario $l = -(51/28)b$ at high temperatures. Numerically the change amounts to at most 0.5% at high temperatures and vanishes to good approximation for low temperatures in the HRG.[23] The change in the energy density and pressure is slightly larger than in the entropy density. This is due to the fact that chemical potentials have a larger contribution to the energy density and pressure compared to the entropy density. In the massless limit, this can be seen by comparing the effective relativistic degrees of freedom for the entropy and energy density in Eqs. (3.36) and (3.39), respectively (see also Fig. 7.11). There the contribution proportional to μ^2 is twice as large in the energy density compared to the entropy density.

In the high temperature regime we show results obtained by the true ideal quark gas approximation without any perturbative corrections (dashed lines) and results obtained by using the interpolated pQCD results according to [49] for $s(T,0)$, $\epsilon(T,0)$, and $p(T,0)$ and adding the contribution of nonvanishing chemical potentials obtained in the ideal quark gas limit (continuous line). The perfect agreement of the latter with the results obtained with lattice susceptibilities (2+1 and 2+1+1 flavor) are due to the fact that around T_{QCD} we used these interpolated pQCD results for $s(T,0)$, $\epsilon(T,0)$, and $p(T,0)$. The smooth connections to the HRG results at low temperatures are based on the fact of the matching of the pQCD results to the

[23] The change of the effective relativistic degrees of freedom due to nonvanishing chemical potentials has also been studied by [139] and found to be small for equal lepton asymmetries and $l \sim 10^{-2}$.

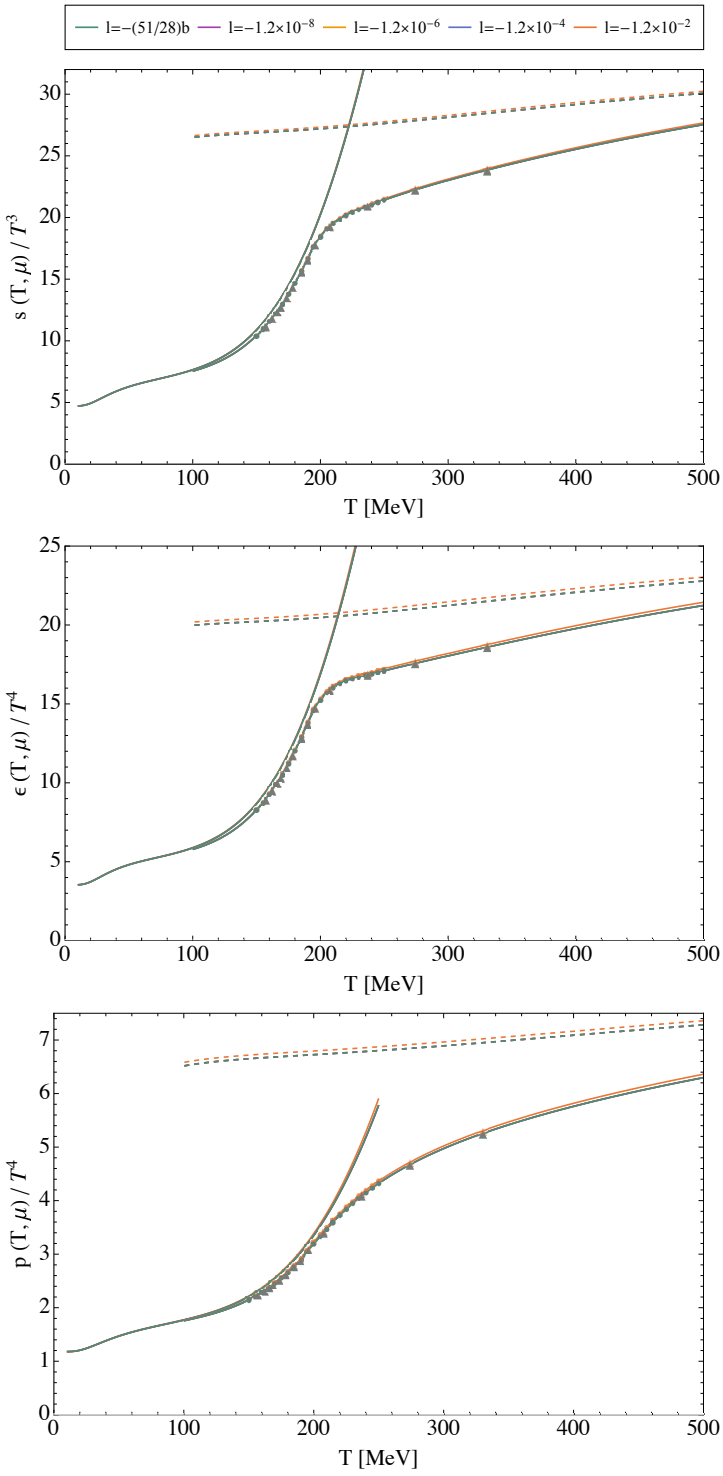

Fig. 7.10: Temperature evolution of entropy density, energy density, and pressure for different negative total lepton asymmetries l and $l_\alpha = l/3$. Continuous lines at low temperatures are results for the HRG. The symbols • and ▲ indicate results obtained using 2+1 flavor and 2+1+1 flavor lattice QCD susceptibilities, respectively. The dashed lines are the true ideal quark gas results without perturbative corrections. Continuous lines for high temperatures are ideal quark gas results with $s(T,0)$, $\epsilon(T,0)$, and $p(T,0)$ according to [49] including strong interaction effects.

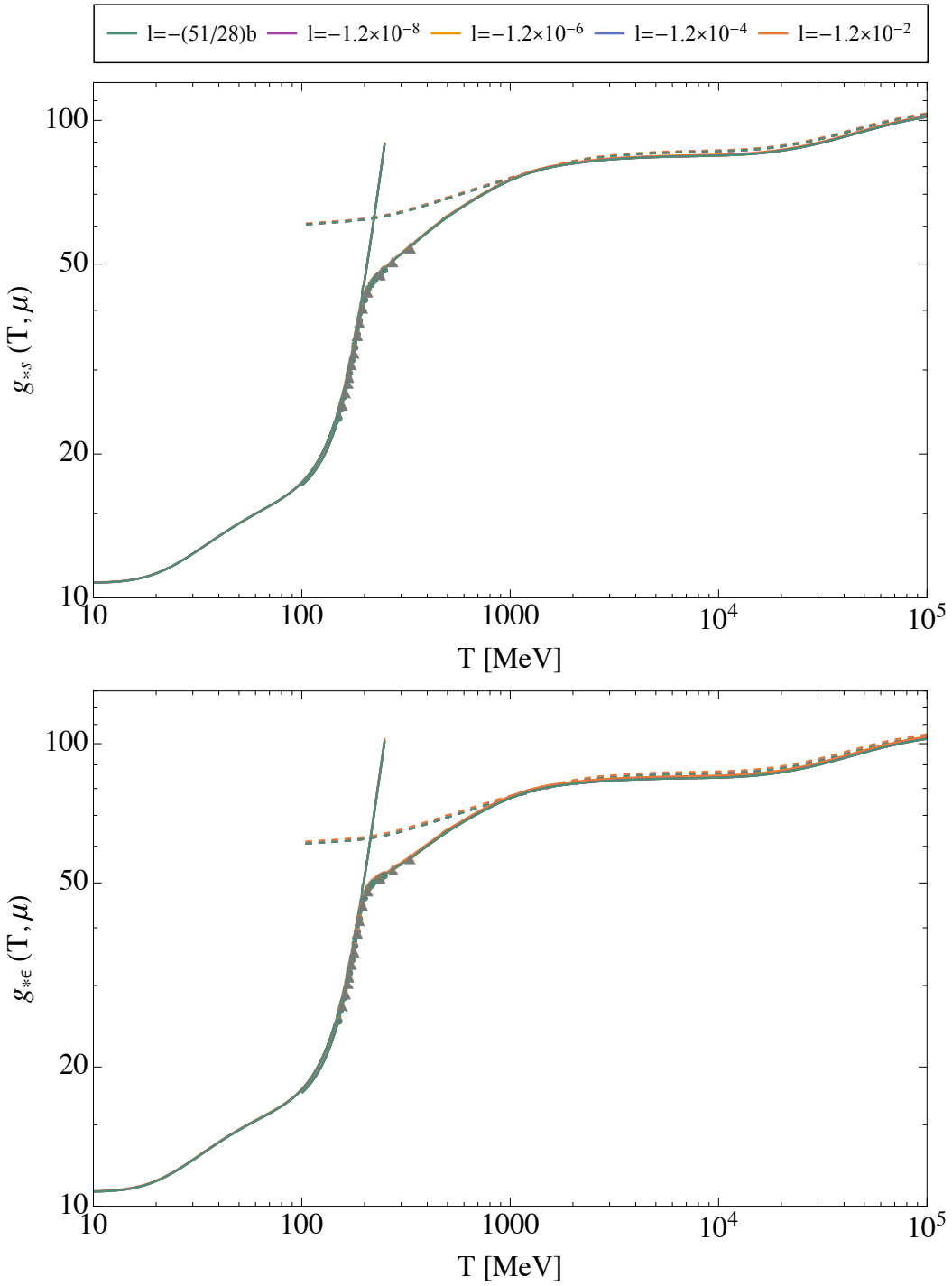

Fig. 7.11: Temperature evolution of efective relativistic degrees of freedom $g_{*s}(T,\mu) = (45/2\pi^2T^3)s(T,\mu)$ and $g_{*\epsilon}(T,\mu) = (30/\pi^2T^4)\epsilon(T,\mu)$ for different negative total lepton asymmetries l and $l_\alpha = l/3$. Notations as before.

HRG at relatively low temperatures in [49]. In Fig. 7.10 we see, that the ideal quark gas approximation overestimates entropy density, energy density and pressure when not using the interpolated pQCD results, which take into account the considerably large interactions between gluons. Figure 7.11 shows in terms of the effective relativistic degrees of freedom (defined via the entropy and energy density, respectively) that the ideal gas limit is not reached until very high temperatures of about $T \sim 1$ GeV.[24] Thus, in our case, for the determination of the temperature evolution of the chemical potentials around the QCD transition, it is more appropriate to take the strong gluonic interactions into account via using interpolated pQCD results for the entropy density.

For unequal lepton flavor asymmetries the chemical potentials can be larger and thus is the change in the effective relativistic degrees of freedom (cf. Sec. 7.2.5). This can be seen in Fig. 7.8 (bottom right), where we show the evolution of $g_{*s}(T, \mu)$ in the case of equal lepton flavor asymmetries with $l = -1.2 \times 10^{-2}$ and an extreme case of unequal lepton flavor asymmetries $l_e = 0$ and $l_\mu = -0.1 = -l_\tau$. In the latter case we get approximately 34 additional effective degrees of freedom at $T \sim 500$ MeV, 14 at $T \sim T_{\mathrm{QCD}}$, and 4 at $T \sim 10$ MeV compared to the standard scenario [cf. Fig. 7.8 (bottom right)]. Efficient neutrino oscillations will equilibrate these lepton flavor asymmetries for $T \lesssim 10$ MeV. Thus, $g_{*s}(T, \mu)$ will be as small as in the standard scenario at BBN and for the CMB and these findings are not in contradiction with observational constraints Nevertheless, the increased $g_{*s}(T, \mu)$ for unequal lepton flavor asymmetries lead to an even more drastic change of effective relativistic degrees of freedom during the QCD transition than in the standard case. This would, e.g., lead to a change in the gravitational wave background in frequencies of several nHz today, which might be detectable by pulsar timing arrays [37].

[24] At temperatures $T > 500$ MeV we also included $W^{\pm}$, Z^0, and Higgs bosons in our calculations.

8 Convergence Properties

First principle lattice QCD calculations aim at determining or at least restricting the location of a possible second-order critical endpoint (CEP) of a first-order phase transition line in the QCD phase diagram $(\mu_{\mathrm{CEP}}, T_{\mathrm{CEP}})$. With the Taylor series method, introduced in Chapter 6, the calculation of several thermodynamic variables can be extended to nonvanishing chemical potentials. Techniques on estimating the radius of convergence of the Taylor series method and using this method to estimate the location of a possible CEP in the QCD phase diagram have been developed. Our technique of tracing the evolution of chemical potentials at nonvanishing lepton asymmetry also makes use of a Taylor series of the QCD pressure around vanishing chemical potentials for temperatures close to T_{QCD}. However, as we are considering possibly large chemical potentials due to large lepton (flavor) asymmetries, we have to check if the Taylor series ansatz can be used for our purpose. In this Chapter the applicability and constraints of our technique using a Taylor series ansatz of the QCD pressure up to $\mathcal{O}(\mu^2)$ are studied. Therefore, we will comment on the convergence behavior of the Taylor series method in general and in lattice QCD, and the possibility to determine the location of a possible CEP of QCD with this method.

8.1 Convergence Criterion

In general, the convergence of a (power) series,

$$\sum_{n=1}^{\infty} a_n = \sum_{n=1}^{\infty} c_n x^n \ , \tag{8.1}$$

can be tested with the ratio test: for

$$L = \lim_{n\to\infty} \left| \frac{a_{n+1}}{a_n} \right| < 1 \tag{8.2}$$

the series converges absolutely. The radius of convergence r is a nonnegative real number or ∞ such that for $|x| < r$ the series given in Eq. (8.1) converges. It can be obtained from the behavior of the expansion coefficients c_n:

$$r = \lim_{n\to\infty} r_n = \lim_{n\to\infty} \left| \frac{c_n}{c_{n+1}} \right| \ . \tag{8.3}$$

The radius of convergence of a Taylor series is determined by the distance from the series' origin to the nearest nonanalytic point, i.e., singularity, in the complex plane.

It is not given that the radius of convergence $r > 0$. Furthermore, if a Taylor series of a function converges, it is not given that it converges to the function itself. This is true only for points x for which the remainder converges to zero.

However, in practice one typically only knows a finite number of terms of a series and the limit $n \to \infty$ cannot be performed. Thus, one has to rely on approximate methods to estimate the radius of convergence from a finite number of expansion coefficients. This can be done by a Domb–Sykes plot [140], i.e., plotting the estimates for the radius of convergence $1/r_n$ versus $1/n$ and graphically extrapolate to $1/n = 0$ via a linear fit. This works for expansion coefficients of a common or alternating sign. A more advanced estimator, which also works in case of an irregular sign pattern of the expansion coefficients, is given by the Mercer–Roberts estimator [141]

$$r_n = \left| \frac{c_{n+1}c_{n-1} - c_n^2}{c_{n+2}c_n - c_{n+1}^2} \right|^{\frac{1}{4}} \ . \tag{8.4}$$

Subsequently, the radius of convergence according to this estimator can be estimated in a Domb–Sykes plot. In contrast to the ratio estimator, more expansion coefficients are needed for the Mercer-Roberts estimator and it works best for singularities away from the real axis [141]. Trying to estimate the radius of convergence by only a small number of expansion coefficients might be affected by some unphysical behavior of these first expansion coefficients. Thus, in general estimating the radius of convergence works better the more expansion coefficients are known.

In lattice QCD estimates for the radius of convergence of the Taylor series of the QCD pressure are studied. Therefore, the Taylor series of p^{QCD} around vanishing chemical potentials is considered in the (μ_B, T) plane, i.e., for vanishing other chemical potentials,[25]

$$p^{\mathrm{QCD}}(T, \mu_B) = \sum_{n=0}^{\infty} c_n \mu_B^n = \sum_{n=0}^{\infty} \frac{1}{n!} \chi_n^B \mu_B^n \ , \ \chi_n^B = \left. \frac{\partial^n p^{\mathrm{QCD}}}{\partial \mu_B^n} \right|_{\mu=0} \ . \tag{8.5}$$

As all odd expansion coefficients vanish, the radius of convergence according to the Taylor expansion coefficients of the pressure can theoretically be obtained by

$$r^p = \lim_{n \to \infty} r_{2n}^p \ , \tag{8.6}$$

with the estimator for the radius of convergence r_{2n}^p according to Eq. (8.3) given by

$$\left(\frac{\mu_B^{\mathrm{crit}}}{T} \right)^p \equiv r_{2n}^p = \frac{1}{T} \sqrt{\left| \frac{c_{2n}}{c_{2n+2}} \right|} = \frac{1}{T} \sqrt{\left| \frac{(2n+2)(2n+1)\chi_{2n}^B}{\chi_{2n+2}^B} \right|} \ . \tag{8.7}$$

[25] For notational simplicity and the sake of easier comparison, in this Section we will rely on the notation for the susceptibilities often used in the context of lattice QCD.

This definition is widely used in the context of lattice QCD to estimate the radius of convergence of the Taylor series method, cf. e.g. [94, 125, 142–144]. While the pressure stays finite and continuous at a possible CEP in the QCD phase diagram, which is associated with a nonanalyticity, its derivatives, the susceptibilities, are expected to diverge at this point (cf. Fig. 3.1). Thus, their Taylor series will behave differently near the phase boundary. For the susceptibility series

$$\begin{aligned} \chi_2^B = \frac{\partial^2 p}{\partial \mu_B^2} &= \sum_{n=2}^{\infty} n(n-1) c_n \mu_B^{n-2} \\ &= \sum_{n=2}^{\infty} \frac{n(n-1)}{n!} \chi_n^B \mu_B^{n-2} = \sum_{n=2}^{\infty} c_{n-2}^{\chi} \mu_B^{n-2} \ , \end{aligned} \tag{8.8}$$

the estimator for the radius of convergence r_{2n}^{χ} is given by

$$\begin{aligned} \left(\frac{\mu_B^{\text{crit}}}{T} \right)^{\chi} \equiv r_{2n}^{\chi} &= \frac{1}{T} \sqrt{\left| \frac{c_{2n-2}^{\chi}}{c_{2n}^{\chi}} \right|} = \frac{1}{T} \sqrt{\left| \frac{2n(2n-1)\chi_{2n}^B}{\chi_{2n+2}^B} \right|} \\ &= r_{2n}^{p} \sqrt{\left| \frac{2n(2n-1)}{(2n+2)(2n+1)} \right|} \ . \end{aligned} \tag{8.9}$$

It is reported that this estimator for the radius of convergences converges faster and, thus, might be more suitable than the corresponding one for the pressure series [125, 142]. At finite n the two estimators yield different results with $r_{2n}^{\chi} < r_{2n}^{p}$ as can be seen in Eq. (8.9). In the limit $n \to \infty$ both estimators for the radius of convergence will reach the same value r. Other definitions of the radius of convergence and their application for QCD have been discussed in the literature, see, e.g., [83, 125, 145, 146].

One has to keep in mind that the singularity closest to $\mu = 0$ will determine the radius of convergence of the Taylor series in lattice QCD and it not necessarily has to lie on the real axis. Only if all expansion coefficients, i.e., the susceptibilities are positive, then the singularity lies on the real axis [141][26] and the radius of convergence of the Taylor series determines the location of the singularity on the real axis, i.e., the location of a possible CEP.

In general, the exact radius of convergence may provide a valuable estimate for the location of a possible CEP. However, the region of reliability of the Taylor series and the radius of convergence are a priori unknown. One possibility for obtaining an estimate for the radius of convergence is to use the expected asymptotic behavior

[26] In fact, for a singularity to lie on the real axis a few negative expansion coefficients are not excluded. The expansion coefficients asymptotically have to be positive.

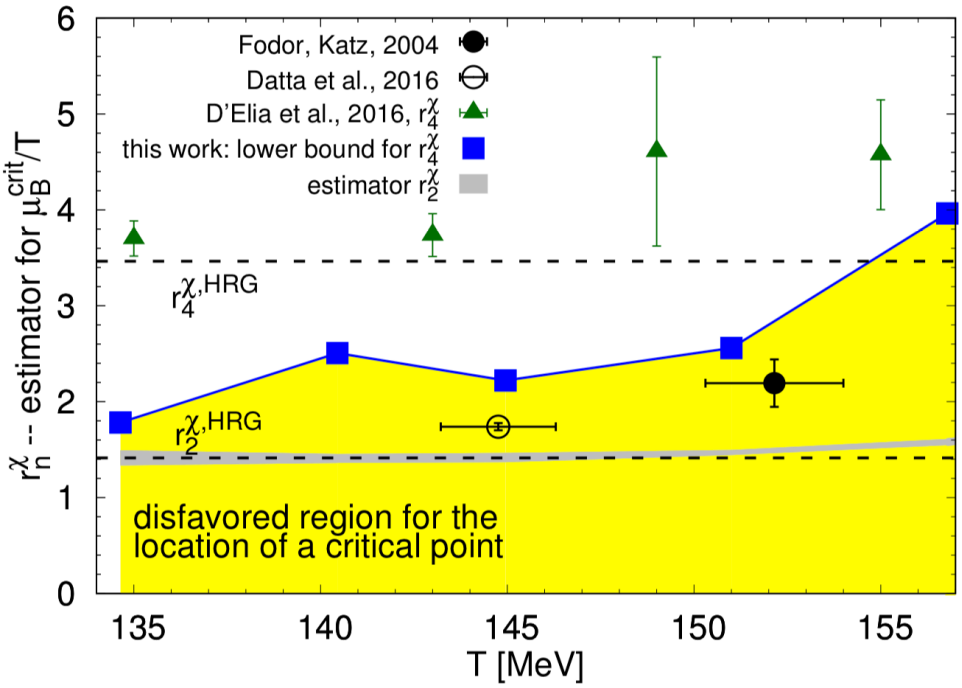

Fig. 8.1: Estimators for the radius of convergence of the Taylor series of the susceptibility r_4^χ for vanishing μ_Q and μ_S obtained by lattice QCD calculations ($N_\tau = 8$) [94] (■). Also shown are results from analytic continuation of imaginary chemical potential [148] (▲) and rescaled estimates for the location of the critical point from [143] (○) and [150] (●). The plot is taken from [94].

of the r_{2n}, if known. Another is to assume that r has been reached when subsequent estimators r_{2n} do not change within errors anymore (cf. [142]). The applicability of this method to lattice QCD will be discussed in the following Section.

8.2 Critical Point Location

A possible CEP of a first-order phase transition line in the QCD phase diagram (μ_B, T) plane should be located somewhere at the transition line $T_{\mathrm{QCD}}(\mu_B)$ which separates confined from deconfined phase in the QCD phase diagram. It has been shown that the curvature of the transition line is negative and surprisingly small [22, 147–149]. Thus a possible CEP is disfavored for $T > T_{\mathrm{QCD}}(0)$.

In Fig. 8.1 [94] we can see different estimates for the radius of convergence, i.e., the critical baryon chemical potential μ_B^{crit}/T, according to the susceptibility series given in Eq. (8.9) which yield a smaller radius of convergence for finite n compared

to Eq. (8.7). The results are obtained from lattice QCD calculations via a Taylor series around vanishing baryon chemical potential [94] (■), analytic continuation of imaginary chemical potential [148] (▲), and estimates on the CEP location are obtained by [143] (○) and [150] (●). However, the different analyses come to different and to some extent even contradictory results.

According to Eq. (8.9) the ratio of susceptibilities asymptotically needs to decrease as $|\chi^B_{2n}/\chi^B_{2n+2}| \sim 1/n^2$ to yield a finite radius of convergence for $n \to \infty$. For the HRG the ratio of susceptibilities is constant $|\chi^B_{2n}/\chi^B_{2n+2}|^{\mathrm{HRG}} = 1$, thus yield an infinite radius of convergence. For comparison estimators for the radius of convergence of the HRG are shown in Fig. 8.1. Up to sixth order all susceptibility ratios do not differ much from the HRG results within errors for $T \lesssim T_{\mathrm{QCD}}$ [94, 144, 148], see Fig. 8.1. Thus, one cannot finally rule out an infinite radius of convergence at the moment. However, there are indications that ratios of susceptibilities at nonvanishing chemical potentials become smaller compared to the corresponding HRG ratios [113]. According to Ref. [94], using sixth order expansion coefficients, at temperatures $T > 135$ MeV a CEP is disfavored for $\mu_B \leq 2T$, see Fig. 8.1.

A huge drawback of the determination of the radius of convergence in lattice QCD is that there only exists a (small) finite number of expansion coefficients, currently $2n \leq 8$, and the limit $n \to \infty$ cannot be performed. Estimates for the radius of convergence based on just the first few expansion coefficients might be affected by unknown systematic errors and there exists the possibility that, even if a CEP exists in QCD, lattice QCD may not be sensitive to it at the current level of statistical uncertainty. Studies suggest that higher-order Taylor expansion coefficients are needed for a meaningful application to lattice QCD, cf., e.g., [125, 142, 144].

The applicability of the Taylor series method has been investigated in various studies. In the Ising Model the Taylor series method can successfully be applied to estimate the radius of convergence. However, higher-order ($n \geq 8$ nonvanishing) expansion coefficients and small uncertainties are needed for an accurate determination [151]. More recently, in the case of nonvanishing isospin chemical potential the reliability of the Taylor series method has been studied and compared to lattice QCD results for nonvanishing isospin chemical potential [152]. QCD at nonvanishing isospin is directly accessible by lattice QCD calculations and the QCD phase diagram in the (μ_I, T) plane exhibits a second-order phase transition [36]. Thus, the reliability of the Taylor series for nonvanishing isospin may give hints to the reliability of the Taylor series for nonvanishing baryon chemical potentials and the reliability of the estimates for the radius of convergence. In this study [152], it was

shown that the estimate for the radius of convergence via the susceptibility series r_2^χ is surprisingly close to the phase boundary of the second-order phase transition. Whether higher-order estimators exhibit the same behavior still needs to be investigated.

However, another question is whether a finite estimate for the radius of convergence can be interpreted as estimates on the location of a possible CEP. One can find models reproducing lattice QCD results on baryon number fluctuations, i.e., the same behavior of the estimates r_{2n}^χ, without having a CEP [144, 146, 153]. Thus, apparent convergence in a finite number of ratio estimators does not imply the existence of a CEP and we have to be careful with this interpretation of the estimates for the radius of convergence. Additionally, the Taylor series of p^{QCD} was simplified to an expansion in only one chemical potential, i.e., μ_B, and the other chemical potentials were assumed to vanish. The other chemical potentials may also influence the radius of convergence of the Taylor series as the nearest singularity may be determined by them rather than μ_B.

There exist possible improvements on the reliability of the Taylor series in general and on the estimator of the radius of convergence. The convergence of a Taylor series can be improved further by a resummation of the expansion coefficients based on a Padé approximation, which often shows better convergence behavior, especially in the presence of singularities (cf. [142, 146]). The estimates for the radius of convergence might be improved by using other estimators which show a better convergence behavior like, e.g., the Mercer–Roberts estimator given in Eq. (8.4) (cf. [146]).

Anyway, estimating the radius of convergence from a finite number of expansion coefficients in combination with other lattice QCD results is at the moment the only option to make statements about the location of a possible CEP of a first-order transition line in the QCD phase diagram. For being able to provide a well-founded, rigorous statement on the location of a possible CEP, further studies have to be performed, either via the determination of higher-order lattice QCD susceptibilities or studies of a totally new kind.

8.3 Reliability of Cosmic Trajectory Determination

In this Section, we want to study the reliability of our technique to account for strong interaction effects in the determination of the evolution of chemical potentials. For our calculations in Chapter 7 we considered the Taylor series of the QCD pressure up to $\mathcal{O}(\mu^2)$ and used lattice QCD susceptibilities. We will now, according to our system

of equations for the temperature regime around T_{QCD} given in Eqs. (7.10a)–(7.10c), determine the combination of chemical potentials and lepton (flavor) asymmetries for which our technique is applicable.

Keep in mind that the total pressure is additive, $p(T,\mu) = p^{\mathrm{lep}}(T,\mu) + p^{\mathrm{QCD}}(T,\mu)$. The leptonic contribution to the pressure $p^{\mathrm{lep}}(T,\mu)$ can be determined exactly. Thus, for estimating the reliability bound of our technique we apply

$$\begin{aligned} p_2^{\mathrm{QCD}}(T,\mu) &\leq p^{\mathrm{QCD}}(T,0) \\ \Rightarrow \frac{1}{2}\mu_a \chi_{ab} \mu_b &\leq p^{\mathrm{QCD}}(T,0) \end{aligned} \tag{8.10}$$

as an estimator for convergence in our calculations according to Eq. (8.2), considering all conserved charge chemical potentials as nonvanishing.[27] In the following we will denote $p_2^{\mathrm{QCD}}(T,\mu) \equiv p_2^{\mathrm{QCD}}$ and $p^{\mathrm{QCD}}(T,0) \equiv p_0^{\mathrm{QCD}}$. For $p_2^{\mathrm{QCD}} > p_0^{\mathrm{QCD}}$ a truncation of the Taylor series at $\mathcal{O}(\mu^2)$ is not appropriate anymore and the size of higher-order expansion coefficients should be considered. This constraint may provide a good estimator for the convergence because known higher-order lattice QCD susceptibilities tend to be of the same size or smaller compared to the second order ones within errors (cf. [94, 129, 143]). However, refined analyses of higher-order expansion coefficients with smaller errors have to be awaited to be able to profoundly judge about their impact.

Even though it is not needed, we also could make use of a Taylor series of $p^{\mathrm{lep}}(T,\mu)$ around vanishing chemical potentials. Naively, one could assume that this Taylor series should converge with an infinite radius of convergence, as no critical behavior for the leptons is known at the temperatures we are considering. However, the pressure of the leptons is determined by an integral over the Fermi-Dirac distribution (cf. Eqs. (3.6) and (3.26)) which has singularities for complex values of the chemical potential at $\mu/T = i\pi + 2i\pi k + E/T$ with $k \in \mathbb{Z}$. The singularity nearest to zero determines the radius of convergence of the Taylor series of the pressure, i.e., $r = \mu^c = \sqrt{\pi^2 T^2 + m^2}$.[28] Thus, even though no critical behavior of $p^{\mathrm{lep}}(T,\mu)$ at real μ is observed and we are able to determine it analytically, using a Taylor series we get a finite radius of convergence. Moreover, we found that using the Taylor series ansatz also for $p^{\mathrm{lep}}(T,\mu)$ can limit the convergence of the total pressure even more than using the Taylor series ansatz only for $p^{\mathrm{QCD}}(T,\mu)$. This demonstrates

[27] Actually, also the contribution of nonvanishing chemical potentials to $s^{\mathrm{QCD}}(T,\mu)$ is determined via a Taylor series ansatz. However, as $s^{\mathrm{QCD}}(T,\mu)$ is determined via the Taylor series of the pressure (cf. Sec. 6), as an approximation, we assume the same estimator for convergence to hold.

[28] Keep in mind, that we are performing the integral of the Fermi-Dirac distribution over the interval $[m,\infty]$, cf. Eq. (3.26).

the limitations of the Taylor series method and shows how important it is to treat $p^{\mathrm{lep}}(T,\mu)$ exactly.

For the numerical determination of the chemical potentials of the conserved charges and the lepton flavor asymmetries for which $p_2^{\mathrm{QCD}} \leq p^{\mathrm{QCD}}$ we add this constraint as an additional equation to our system of equations given in Eqs. (7.10a)–(7.10c). As before, we used $p^{\mathrm{QCD}}(T,0)$ by [49]. Having now a system of six equations, we can choose six free parameters. As before, we will choose the five chemical potentials of the conserved charges and additionally we will choose one lepton flavor asymmetry as free parameter. The other two lepton flavor asymmetries will be determined by a fixed relation to the free lepton flavor asymmetry. We will also consider the case of not equally distributed lepton flavor asymmetries in this Section. We will consider 2+1 flavor lattice QCD susceptibilities in this study, as for them a finer temperature grid is available and thus the numerical derivatives of the susceptibilities are assumed to be more accurate. Furthermore, for $T \lesssim 250$ MeV the results obtained with 2+1 and 2+1+1 flavor lattice QCD susceptibilities do not differ substantially for most temperatures. In the following Sections we show results for the chemical potentials and lepton (flavor) asymmetries under the constraints $p_2^{\mathrm{QCD}}/p_0^{\mathrm{QCD}} = 1$ and $p_2^{\mathrm{QCD}}/p_0^{\mathrm{QCD}} = 0.1$ for comparison with a linear interpolation between calculated points.

8.3.1 Constraints on Chemical Potentials

Let us first discuss some general behavior of the chemical potentials under the pressure constraints. Using the constraint on the pressure, given in Eq. (8.10), together with baryon number conservation, given in Eq. (7.10b), we get relations for μ_B and μ_Q which partly decouple from the system of equations:

$$|\mu_Q^c| \leq \sqrt{\frac{2p^{\mathrm{QCD}}(T,0)\chi_{BB} - b^2 s^2(T,\mu)}{\chi_{QQ}\chi_{BB} - \chi_{BQ}^2}} \,, \tag{8.11}$$

$$\mu_B^c = \frac{bs(T,\mu)}{\chi_{BB}} - \mu_Q^c \frac{\chi_{BQ}}{\chi_{BB}} \,, \tag{8.12}$$

where the superscript c denotes the solution obtained under the pressure constraint. These relations are coupled to the system of equations given by Eqs. (7.10a)–(7.10c) only via the entropy density $s(T,\mu)$, to which the chemical potentials of all conserved charges contribute. However, the term proportional to the entropy density in Eq. (8.11) is suppressed by the small baryon asymmetry $b \sim 10^{-10}$ and negligible compared to the term proportional to the pressure. Even quite large lepton (flavor)

asymmetries lead to $s(T,\mu)$ on the order of $s(T,0)$ at $T \sim T_{\mathrm{QCD}}$ (cf. Sec. 7.4). Thus, we can estimate $s(T,\mu) \equiv s \sim 100T^3$ as an upper bound. Together with the baryon asymmetry we get $bs \sim 10^{-8}T^3$. The pressure can be estimated as $p^{\mathrm{QCD}}(T,0) \sim T^4$ (cf. Sec. 7.4) and $\chi_{BB} \sim 10^{-1}T^2$ (cf. Sec. 6.2). Thus, $2p^{\mathrm{QCD}}(T,0)\chi_{BB} \sim 10^{-1}T^6$ and $b^2s^2 \sim 10^{-16}T^6$. We clearly see, that the term proportional to s is negligible for the determination of μ_Q^c and μ_B^c according to Eqs. (8.11) and (8.12) and, hence, they decouple from the system of equations to good approximation. For this reason we obtain to a very good approximation always the same values for μ_Q^c and μ_B^c, respectively, irrespective of the different possibilities of unequal lepton flavor asymmetries we will study in the following.

In Fig. 8.2 (top) the temperature evolution of μ_Q^c and μ_B^c corresponding to the constraint $p_2^{\mathrm{QCD}} = p_0^{\mathrm{QCD}}$ is shown, which separates the values of the chemical potentials for which we assume our approximation of a Taylor series of p^{QCD} up to $\mathcal{O}(\mu^2)$ to be applicable and for which not (shaded regions). To guide the eye, we also show the line $p_2^{\mathrm{QCD}} = 0.1p_0^{\mathrm{QCD}}$ (dashed lines). In Fig. 8.2 (bottom) we also show the (μ_B, μ_Q) plane. In this diagram the temperature evolution is shown by the varying color of the line for $p_2^{\mathrm{QCD}} = p_0^{\mathrm{QCD}}$. For this diagram a counterpart with opposite signs of μ_B and μ_Q exists. To be in agreement with the pressure constraint, we see, that quite large electric charge chemical potentials are allowed, whereas at the same time the baryon chemical potential has to be much smaller. The allowed values of μ_B and μ_Q evolve opposite to each other. While for large temperatures, $T \sim 250$ MeV, larger μ_Q are allowed to fulfill the pressure constraint compared to low temperatures, $T \sim 150$ MeV, μ_B at the same time has to be smaller compared to low temperatures.

The evolution of $\mu_{L_e}^c$ and $\mu_{L_\tau}^c$ corresponding to the pressure constraint in the case of equal lepton flavor asymmetries is shown in Fig. 8.3. The evolution of $\mu_{L_\mu}^c$ is not shown as it is similar to $\mu_{L_e}^c$. The corresponding evolution of the total lepton asymmetry l^c will be discussed in the following Section (cf. Fig. 8.4). In contrast to μ_Q^c and μ_B^c the evolution of the $\mu_{L_\alpha}^c$ is not independent of the case of (equal or unequal) lepton flavor asymmetries we are considering. In the case of unequal lepton flavor asymmetries, the lepton flavor chemical potentials corresponding to a large lepton flavor asymmetry are larger whereas the ones corresponding to a small lepton flavor asymmetry are smaller compared to $\mu_{L_\alpha}^c$ in the case of equal lepton asymmetries.

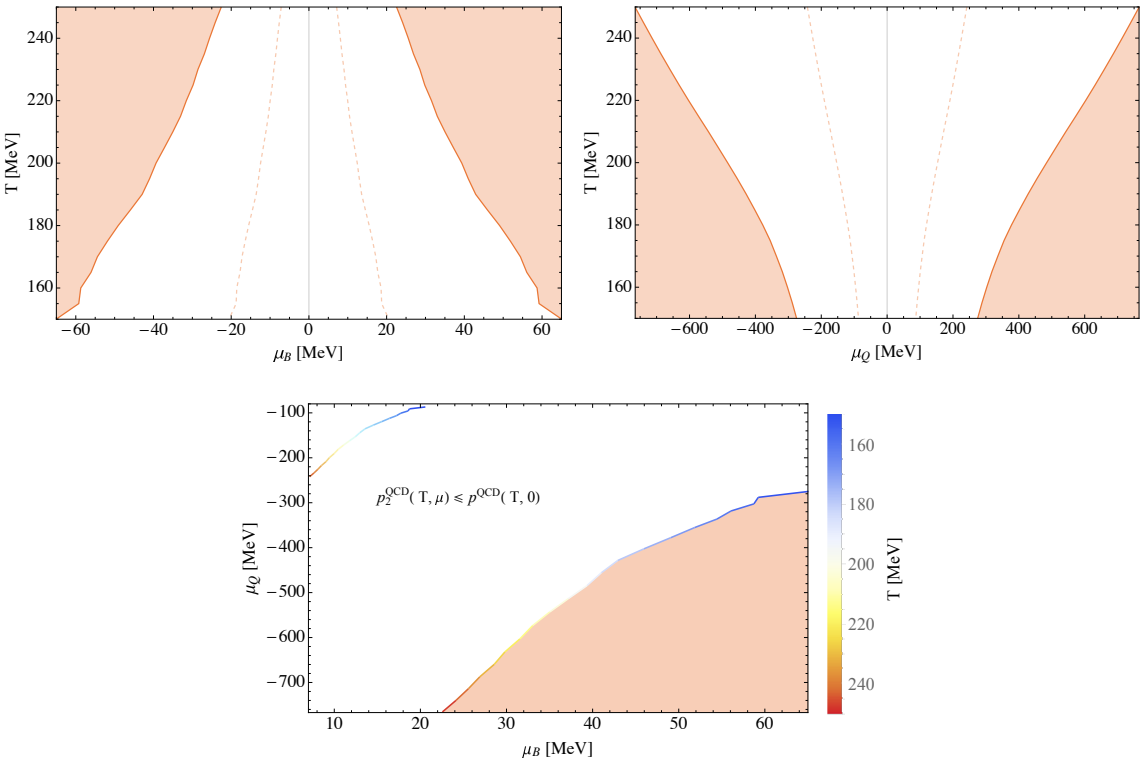

Fig. 8.2: (μ_B, T) plane (top left), (μ_Q, T) plane (top right), and (μ_B, μ_Q) plane (bottom). The lines divide the planes in values of the chemical potentials in agreement with the pressure constraint $p_2^{\mathrm{QCD}}(T,\mu) \leq p^{\mathrm{QCD}}(T,0)$ and for which this constraint is not fulfilled (shaded regions). To good approximation these classifications do not depend on the lepton flavor asymmetry. For the lower diagram a counterpart with opposite signs of the chemical potentials exists. Dashed and light colored lines correspond to the constraint $p_2^{\mathrm{QCD}}(T,\mu) \leq 0.1 p^{\mathrm{QCD}}(T,0)$.

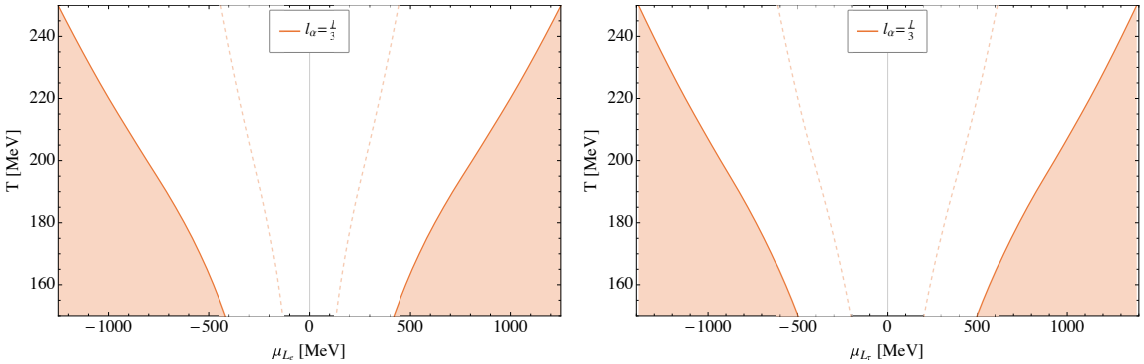

Fig. 8.3: (μ_{L_e}, T) plane (left) and (μ_{L_τ}, T) plane (right) for equal lepton flavor asymmetries $l_\alpha = l/3$. The lines divide the planes in values of the chemical potentials in agreement with the pressure constraint $p_2^{\mathrm{QCD}}(T,\mu) \leq p^{\mathrm{QCD}}(T,0)$ and for which this constraint is not fulfilled (shaded regions). Dashed lines correspond to the constraint $p_2^{\mathrm{QCD}}(T,\mu) \leq 0.1 p^{\mathrm{QCD}}(T,0)$. The (μ_{L_μ}, T) plane is not shown as it is similar to the other planes.

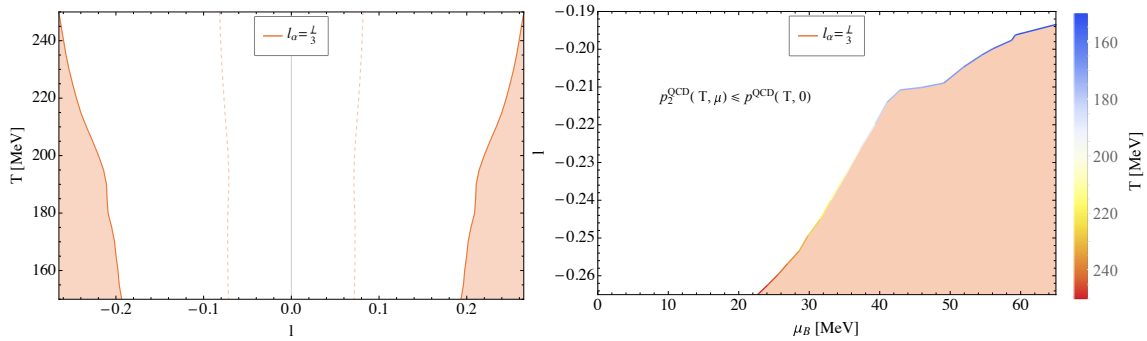

Fig. 8.4: (l, T) plane (left) and (μ_B, l) plane (right) for equal lepton flavor asymmetries $l_\alpha = l/3$. The lines divide the planes in values of the total lepton asymmetry l or, respectively, μ_B in agreement with the pressure constraint $p_2^{\mathrm{QCD}}(T,\mu) \leq p^{\mathrm{QCD}}(T,0)$ and for which this constraint is not fulfilled (shaded regions). Dashed lines correspond to the constraint $p_2^{\mathrm{QCD}}(T,\mu) \leq 0.1 p^{\mathrm{QCD}}(T,0)$. In the (μ_B, l) plane (right) the corresponding line is at very small values and does not lie in the region shown.

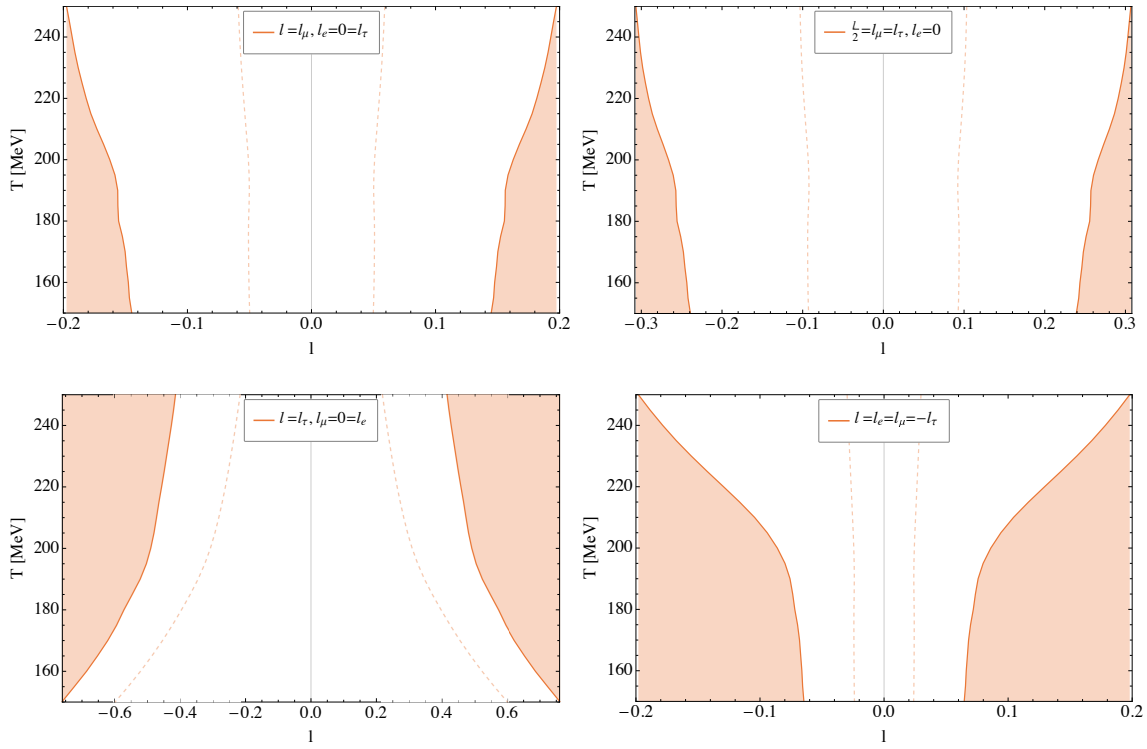

Fig. 8.5: (l, T) plane at different combinations of unequal lepton flavor asymmetries. The lines divide the planes in values of the total lepton asymmetry l in agreement with the pressure constraint $p_2^{\mathrm{QCD}}(T,\mu) \leq p^{\mathrm{QCD}}(T,0)$ and for which this constraint is not fulfilled (shaded regions). Dashed lines correspond to the constraint $p_2^{\mathrm{QCD}}(T,\mu) \leq 0.1 p^{\mathrm{QCD}}(T,0)$.

8.3.2 Constraints on Lepton Flavor Asymmetries

In Fig. 8.4 the temperature evolution of the total lepton asymmetry l^c for equal lepton flavor asymmetries for which the pressure constraint $p_2^{\mathrm{QCD}} \leq p_0^{\mathrm{QCD}}$ is fulfilled is shown (continuous line). For the shaded regions the pressure constraint is not fulfilled. In the (l, T) plane we can see that for equal lepton flavor asymmetries a total lepton asymmetry as large as $|l| \lesssim 0.2$ is in agreement with the pressure constraint for all temperatures $150 \leq T \leq 250$ MeV. We also provide the (μ_B, l) plane in Fig. 8.4 (right).

In Fig. 8.5 we show the (l, T) plane for a selection of different combinations of unequal lepton flavor asymmetries. Depending on the case of unequal lepton flavor asymmetries we are considering, the region in agreement with the pressure constraint varies. The temperature evolution of l^c in the case of $l_\tau = l$ and $l_e = l_\mu = 0$, shown in Fig. 8.5 (bottom left), differs from the other cases. In this case at low temperatures a larger lepton asymmetry is in agreement with the pressure constraint compared to higher temperatures. For the other cases the opposite is true. The case of the non-vanishing tau lepton flavor asymmetry is special, as already discussed in Sec. 7.2.3, as at low temperatures all tau leptons annihilated and the asymmetry remains in the tau neutrinos and thus tau lepton flavor conservation approximately decouples from the system of equations. This leads to larger freedom on the value of the tau lepton flavor asymmetry at low temperatures in agreement with $p_2^{\mathrm{QCD}} \leq p_0^{\mathrm{QCD}}$. For other combinations of unequal lepton flavor asymmetries, which we are not showing in Fig. 8.5, the regions of the (l, T) plane of the phase diagram in agreement and not in agreement with the pressure constraint do not feature a different behavior than the ones which are shown.[29] For the temperature regime we considered, roughly a total lepton asymmetry $|l| \lesssim 0.1$ is in agreement with $p_2^{\mathrm{QCD}} \leq p_0^{\mathrm{QCD}}$ for unequal lepton flavor asymmetries and our technique should be applicable.

Hence, all equal and unequal lepton flavor asymmetries we investigated in Chapter 7 are in agreement with the constraint $p_2^{\mathrm{QCD}} \leq p_0^{\mathrm{QCD}}$. This can also be seen by comparing the evolution of the cosmic trajectories given in Chapter 7 to Figs. 8.2 and 8.3. For all investigated lepton flavor asymmetries the trajectories lie in the region of $p_2^{\mathrm{QCD}} \leq p_0^{\mathrm{QCD}}$. A total lepton asymmetry in agreement with observational constraints, i.e., $|l| \lesssim 0.012$, is in fact in agreement with the even stronger constraint $p_2^{\mathrm{QCD}} \leq 0.1 p_0^{\mathrm{QCD}}$ as can be seen by looking at the dashed lines in Figs. 8.4 and 8.5.

[29] This also includes the cases of vanishing total lepton asymmetry, e.g., $l_e = 0$ and $l_\mu = -l_\tau$, for which we can study the phase diagram in the (l_α, T) plane.

If desired, one could estimate the location of a possible CEP of the QCD phase diagram by the estimate for the radius of convergence given by the pressure constraint $p_2^{\mathrm{QCD}} \leq p_0^{\mathrm{QCD}}$. Thus, for the first time, we are able to estimate the location of a possible CEP not only in the (μ_B, T) plane but also at nonvanishing electric charge chemical potential, lepton flavor chemical potentials, and lepton asymmetry. That is to say, we can estimate the location of a possible CEP for the cosmic QCD transition. We would, however, like the reader to keep in mind the limitations of this estimation which we discussed in Sec. 8.2. In fact, this interpretation of the estimate for the convergence of our technique depends on the possibility to determine the radius of convergence of the Taylor series of the QCD pressure within lattice QCD. This is due to the fact that the pressure constraint and baryon number conservation to a good approximation decouple from the system of equations, as we discussed at the beginning of Sec. 8.3.1, and thus the pressure constraint is to a good approximation determined by the lattice QCD susceptibilities.

Still more mysteries of the universe remain hidden. Their discovery awaits the adventurous scientists of the future. I like it this way.
— Vera Rubin

9 Conclusion

In this thesis we developed and studied a new technique of determining the evolution of chemical potentials in the early universe in the presence of arbitrary lepton flavor asymmetries. The novelty is that we used lattice QCD susceptibilities for the determination of the cosmic trajectory to properly account for strong interaction effects close to $T_{\rm QCD}$. Thus, we were able to connect the approximation of an ideal quark gas with the HRG. Additionally, for high temperatures $T \gtrsim T_{\rm QCD}$ we also partially included higher-order perturbative corrections in our calculations by using results for the entropy density, energy density and pressure at vanishing chemical potentials obtained with pQCD methods [49].

In Chapter 7 we explained in detail the three approximations we are considering for the determination of the cosmic trajectory: (i) the ideal quark gas approximation for which we also included perturbative corrections via using $s(T,0)$ by [49], (ii) using 2+1 and 2+1+1 flavor lattice QCD susceptibilities and the Taylor series of the QCD pressure up to $\mathcal{O}(\mu^2)$, and (iii) the HRG approximation which we extended from 54 to 239 hadron resonances compared to [2]. We also self-consistently included chemical potentials in our calculations, i.e., for the particle net number densities, entropy density, energy density, and pressure. Thus, we determined the standard cosmic trajectory in the 5+1 dimensional QCD phase diagram of chemical potentials of conserved charges and temperature for $l = -(51/28)b$ and, furthermore, the cosmic trajectory for different large lepton flavor asymmetries.

The 2+1+1 flavor lattice QCD susceptibilities allow us to interpolate between the trajectories of the ideal quark gas and HRG. We would like to emphasize the importance of the charm quark contribution at $T \gtrsim 200$ MeV, to obtain a smooth trajectory. This is especially important for the baryon chemical potential, for which the results obtained by 2+1 flavor lattice QCD susceptibilities intersect with the ideal quark gas results in a single point for $|l| \gtrsim 10^{-8}$. Unfortunately, no continuum extrapolated 2+1+1 flavor lattice QCD susceptibilities were available to date.

In general, gaps between the different approximations in our results for the cosmic trajectory, discussed in Section 7.2, are artifacts of our approximations. We were

able to close or at least reduce the gaps between the lattice QCD results and ideal quark gas reported in [1] by partially taking higher-order perturbative corrections of the entropy density $s(T, 0)$ [49] into account in the ideal quark gas approximation. We assume that the remaining gaps might be closed by considering higher-order perturbative corrections also for the determination of the conserved charge densities in our system of equations.

In Fig. 7.1 we observed small gaps for μ_B at low temperature between lattice QCD results and the HRG, which might be closed by lattice QCD susceptibilities for lower temperatures. Nevertheless, these gaps might also be due to limitations of the HRG approximation to describe all thermodynamical aspects of QCD (cf. Sec. 5.4).

In Sec. 7.2.5 we investigated the impact of unequal lepton flavor asymmetries on the cosmic trajectory. Assuming unequal lepton flavor asymmetries larger conserved charge chemical potentials can be obtained while satisfying observational constraints on the total lepton asymmetry. Additionally, for different individual lepton flavor asymmetries l_α, the evolution of the lepton flavor chemical potentials can be considerably different. Especially for very large l_α of opposite sign we can see larger gaps between the HRG and lattice QCD results which might be due to limitations of the HRG approximation (cf. Fig. 7.8). Here it would be likewise desirable to have lattice QCD susceptibilities for lower temperatures available.

For equally and not equally distributed lepton flavor asymmetries we find that the absolute value of the electric charge chemical potential exceeds the baryon chemical potential before pion annihilation (except in the standard scenario). Thus, μ_Q might be more important for the thermal history of the early universe than μ_B. In the case of equal lepton flavor asymmetries $|l| \gtrsim 0.12$ yield $|\mu_Q| \gtrsim m_\pi$ which might enable pion condensation in the early universe. However, this lepton asymmetry is an order of magnitude larger than the observational constraint on l. For unequal lepton flavor asymmetries, we found that the region of pion condensation might be reached while satisfying observational constraints, see Fig. 7.9.

In Sec. 7.4 we studied the change of the entropy density, energy density and pressure according to nonvanishing chemical potentials. For equal lepton flavor asymmetries in agreement with observational constraints, the change amounts to at most 0.5% at high temperatures. While efficient neutrino flavor oscillations will equilibrate different lepton flavor asymmetries, such that the effective relativistic degrees of freedom g_{*s} at BBN and the CMB are in agreement with observational constraints, at high temperatures g_{*s} for large unequal lepton flavor asymmetries can be much larger compared to the standard case. A change in g_{*s} might be detectable in the gravitational wave background with pulsar timing arrays [37].

In Chapter 8 we studied the convergence properties of the Taylor series method for the QCD pressure up to $\mathcal{O}(\mu^2)$ which we use in our technique for determining the cosmic trajectory close to T_{QCD}. We used the ratio test to determine chemical potentials and lepton asymmetries for which we estimate the pressure series to be reliable, i.e., $p_2^{\mathrm{QCD}}(T,\mu) \leq p_0^{\mathrm{QCD}}(T,0)$. In general, we found that all chemical potentials and lepton flavor asymmetries investigated in Chapter 7 are in agreement with this pressure constraint. Simplifying the results for unequal lepton flavor asymmetries, a total lepton asymmetry $|l| \lesssim 0.1$ is in agreement with the pressure constraint and our technique should be applicable (cf. Sec. 8.3). An interesting feature is, that we obtained constraints on μ_B and μ_Q in Eqs. (8.11) and (8.12) which were to good approximation independent of the lepton flavor asymmetries. Thus, the convergence of our technique is totally determined by lattice QCD results.

We also commented on the possibility to estimate the radius of convergence and the location of a possible critical endpoint by a small finite number of expansion coefficients in Chapter 8. There are many reasons, why this might not be a good idea, see Secs. 8.1 and 8.2. However, if one would be able to estimate the location of a possible CEP with estimates on the radius of convergence, our technique presents an improvement compared to just considering lattice QCD results, as we are also able to consider the effect of nonvanishing chemical potentials of other conserved charges and lepton flavor asymmetries. Thus, we might be able to estimate the location of a possible CEP of the cosmic QCD transition with our technique. As in lattice QCD, it will be absolutely necessary to consider numerous higher-order expansion coefficients of the Taylor series of the pressure to be able to provide a well-founded statement for the radius of convergence of the Taylor series and the location of a possible CEP in the QCD phase diagram.

The current precision of lattice susceptibilities and the ideal quark gas and HRG approximations used in this thesis do not allow us to make any statement on the nature of the cosmic QCD transition.

A possible further application of the technique we presented in this thesis is the determination of the evolution of chemical potentials in heavy ion collisions assuming thermal equilibrium. Therefore, the system of equations needs to be adjusted. In contrast to the early universe, due to the short timescale of relativistic heavy ion collisions weak processes are not in equilibrium and individual quark flavors like strangeness are conserved. This yields additional conservation equations for our system of equations. Moreover, the values for the conserved charges have to be tuned to the conditions present in heavy ion collisions.

A Appendix

A.1 Useful Relations and Integrals

For the study of particle density, energy density and pressure in Chapter 3, it is useful to know the following relations while dealing with Fermi-Dirac and Bose-Einstein distributions:

- Relations for the Riemann zeta function:

$$\zeta(s) = \sum_{k=1}^{\infty} k^{-s} \ , \tag{A.1}$$

$$\zeta(2) = \frac{\pi^2}{6} \ , \zeta(3) \simeq 1.2020569032 \ , \zeta(4) = \frac{\pi^4}{90} \ , \tag{A.2}$$

$$\sum_{k=1}^{\infty} (-1)^{k-1} k^{-n} = \left(1 - 2^{1-n}\right) \zeta(n) \ . \tag{A.3}$$

- Further relations and series:

$$\binom{n}{k} = \frac{n!}{k!(n-k)!} \ , \tag{A.4}$$

$$(x+y)^n = \sum_{k=0}^{n} \binom{n}{k} x^{n-k} y^k \ , \tag{A.5}$$

$$\sum_{k=0}^{\infty} x^k = (1-x)^{-1} \ , x < 1 \ . \tag{A.6}$$

- Useful relations for Fermi-Dirac and Bose-Einstein distributions:

$$\left(e^x \pm 1\right)^{-1} + \left(e^{-x} \pm 1\right)^{-1} = \pm 1 \ , \tag{A.7}$$

$$\left(e^x \pm 1\right)^{-1} \overset{(A.6)}{=} \sum_{k=1}^{\infty} (-1)^{k-1} \, e^{-kx} \ . \tag{A.8}$$

- Integrals:

$$\int_0^{\infty} \mathrm{d}x \frac{x^n}{e^x - 1} = n! \zeta(n+1) \ , \tag{A.9}$$

$$\int_0^{\infty} \mathrm{d}x \frac{x^n}{e^x + 1} = n! \left(1 - 2^{-n}\right) \zeta(n+1) \ . \tag{A.10}$$

- The following relation yield the solution of the fermionic particle asymmetry $n_i - n_{\bar{i}}$ in the relativistic limit ($m_i \ll T$) for $n = 2$ and for $n = 3$ for the total energy density $\epsilon_{\mathrm{tot},i}$ [154]:

$$\sum_{s=\pm 1} \int_0^\infty \mathrm{d}x \frac{s^{n+1} x^n}{e^{x - s\xi} + 1} = \frac{\xi^{n+1}}{n+1} + \sum_{k=0}^{n-1} \left[1 + (-1)^{n+k+1}\right] \left(1 - 2^{k-n}\right) \frac{n!}{k!} \zeta\left(n - k + 1\right) \xi^k \ , \tag{A.11}$$

- The following relation yield the solution of the bosonic particle asymmetry $n_i - n_{\bar{i}}$ in the relativistic limit ($m_i \ll T$) for $n = 2$ and for $n = 3$ for the total energy density $\epsilon_{\mathrm{tot},i}$:

$$\sum_{s=\pm 1} \int_0^\infty \mathrm{d}x \frac{s^{n+1} x^n}{e^{x - s\xi} - 1} = - \frac{\xi^{n+1}}{n+1} + \sum_{k=0}^{n-1} \left[1 + (-1)^{n+k+1}\right] \frac{n!}{k!} \zeta\left(n - k + 1\right) \xi^k \ . \tag{A.12}$$

A.2 2+1+1 Flavor Lattice QCD Susceptibilities

2+1+1 flavor lattice QCD results (not continuum extrapolated, $N_\tau = 8$) for χ_{BC}, χ_{QC}, χ_{CC} and χ_{SC} are reported by the HotQCD collaboration [119, 131]. For the calculation of the cosmic trajectory, we do not need the last one, as strangeness is not conserved in the early universe due to weak interactions. By the index C the charm quantum number (charmness) is meant, and also the charm quark contribution to B and Q is considered. As only the charm quark carries charmness, we can directly interpret these susceptibilities as charm quark susceptibilities: χ_{Bc}, χ_{Qc}, and χ_{cc}. The relations for the conserved charge susceptibilities χ^c_{QQ}, χ^c_{QB}, and χ^c_{BB} for the 2+1+1 flavor system (denoted by the superscript c to distinguish it from susceptibilities of the 2+1 flavor system) can be obtained using the relations between conserved charge susceptibilities and quark number susceptibilities, cf. Sec. 6.1. Then, we can separate the quark number susceptibilities with the charm quark from the ones without the charm quark (cf. Eqs. (6.2) and (6.11)–(6.16)). The quark susceptibilities without the charm quark yield the conserved charge susceptibilities of the 2+1 flavor system. Thus, in total we get the following relations for the conserved charge

susceptibilities of the 2+1+1 flavor system:

$$\chi^c_{QQ} = \chi_{QQ} + \frac{4}{3}\chi_{QC} - \frac{4}{9}\chi_{CC} \ , \tag{A.13}$$

$$\chi^c_{QB} = \chi_{QB} + \frac{2}{3}\chi_{BC} + \frac{1}{3}\chi_{QC} - \frac{2}{9}\chi_{CC} \ , \tag{A.14}$$

$$\chi^c_{BB} = \chi_{BB} + \frac{2}{3}\chi_{BC} - \frac{1}{9}\chi_{CC} \ . \tag{A.15}$$

The errors of these susceptibilities have been determined via error propagation.

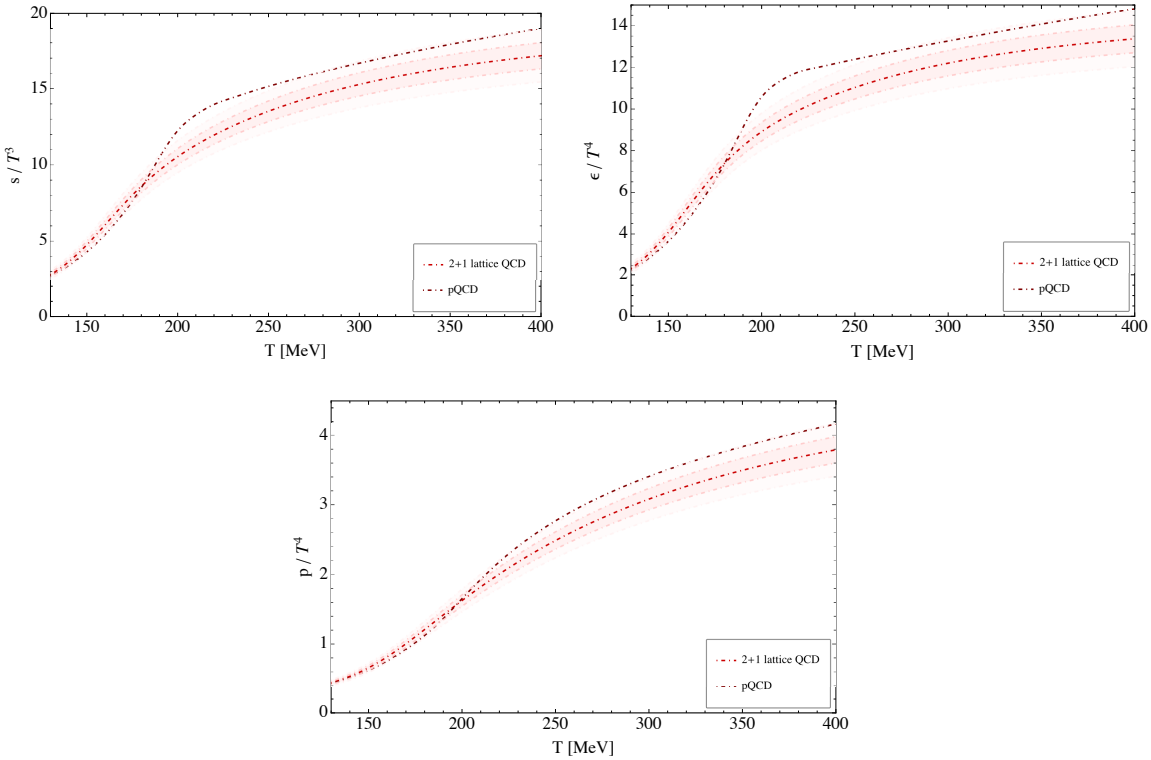

Fig. A.1: Entropy density, energy density and pressure given by interpolated pQCD results [49, 155] (pQCD) and a 2+1 flavor lattice QCD parametrization [156] (2+1 lattice QCD) at vanishing chemical potentials with 5% and 10% error bands.

A.3 Equation of State

Throughout our numerical evaluation we used the interpolated pQCD results for the entropy density, energy density and pressure at vanishing chemical potentials by [49, 155]. Here we want to compare these results with the parametrization of the EoS in 2+1 flavor QCD at vanishing chemical potentials for $130 \leq T \leq 400$ MeV [156].

In Fig. A.1 the entropy density, energy density and pressure of both methods are shown. Additionally we show 5% and 10% error bands for the lattice QCD parametrization. For our calculations we decided to rely on the interpolated pQCD results as the discrepancy to the 2+1 flavor lattice QCD parametrization is rather small, $\lesssim 10\%$. Furthermore, at temperatures $T \gtrsim 180$ MeV for which the charm quark becomes important (cf. Sec. 6.1), it is more appropriate to use the interpolated pQCD results for which all quark flavors have been considered and not only 2+1 flavors.

A.4 Particle and Hadron Resonance Properties

In the following particle and hadron resonance properties (particle, antiparticle, mass m_i, electric charge q_i, spin s_i, degrees of freedom g_i) according to the summary tables of the Particle Data Group 2018 [3] are listed. These properties have been used for the calculations explained in this thesis. In our calculation of the HRG we included resonances up to $m_{\Lambda(2350)} \approx 2350$ MeV $\sim 15 T_{\mathrm{QCD}}$, with $T_{\mathrm{QCD}} \approx 156.5 \pm 1.5$ MeV [22]. Mass uncertainties have been neglected in the calculations. As already mentioned we separately count the degrees of freedom for particles and antiparticles. Therefore our degrees of freedom may differ by a factor of two compared to other references. Particles which are their own antiparticles are denoted by "$-$" in the antiparticle column. For unknown spin $s_i =?$ (see summary table *Baryons* in [3]) we assumed the spin to be minimal for our calculation to not overestimate the influence of a resonance, i.e. $s_i \geq 1/2$ and thus $g_i \geq 1$. The particles are tabulated according to their properties: strangeness S, charm C, and bottomness B.

Table A.1: Leptons, quarks and gauge bosons.

		m_i [MeV]	q_i [e]	s_i	g_i
e^-	e^+	0.511	-1	1/2	2
μ^-	μ^+	105.658	-1	1/2	2
τ^-	τ^+	1776.86	-1	1/2	2
ν_e	$\bar{\nu}_e$	0	0	1/2	1
ν_μ	$\bar{\nu}_\mu$	0	0	1/2	1
ν_τ	$\bar{\nu}_\tau$	0	0	1/2	1
u	$\bar{u}$	2.2	2/3	1/2	6
d	$\bar{d}$	4.7	$-1/3$	1/2	6
s	$\bar{s}$	95	$-1/3$	1/2	6
c	$\bar{c}$	1275	2/3	1/2	6
b	$\bar{b}$	4180	$-1/3$	1/2	6
t	$\bar{t}$	173000	2/3	1/2	6
W^-	W^+	80379	-1	1	3
Z	$-$	91187.6	0	1	3/2
γ	$-$	0	0	1	1
g	$\bar{g}$	0	0	1	8
H	$-$	0	0	0	1/2

Table A.2: Light unflavored mesons with $S = C = B = 0$. $(\pi,\ b,\ \rho,\ a)$: $u\bar{d}$, $(u\bar{u} - d\bar{d})/\sqrt{2}$, $d\bar{u}$. $(\eta,\ \eta\prime,\ h,\ h\prime,\ \omega,\ \phi,\ f,\ f\prime)$: $c_1(u\bar{u} + d\bar{d}) + c_2 s\bar{s}$.

		m_i [MeV]	q_i [e]	s_i	g_i
π^+	π^-	139.571	+1	0	1
π^0	–	134.977	0	0	1/2
η	–	547.862	0	0	1/2
$f_0(500)$	–	500	0	0	1/2
$\rho(770)^0$	–	775.26	0	1	3/2
$\rho(770)^+$	$\rho(770)^-$	775.11	+1	1	3
$\omega(782)$	–	782.65	0	1	3/2
$\eta\prime$	–	957.58	0	0	1/2
$f_0(980)$	–	990	0	0	1/2
$a_0(980)^0$	–	980	0	0	1/2
$a_0(980)^+$	$a_0(980)^-$	980	+1	0	1
$\phi(1020)$	–	1019.461	0	1	3/2
$h_1(1170)$	–	1170	0	1	3/2
$b_1(1235)^+$	$b_1(1235)^-$	1229.5	+1	1	3
$b_1(1235)^0$	–	1229.5	0	1	3/2
$a_1(1260)^+$	$a_1(1260)^-$	1230	+1	1	3
$a_1(1260)^0$	–	1230	0	1	3/2
$f_2(1270)$	–	1275.5	0	2	5/2
$f_1(1285)$	–	1281.9	0	1	3/2
$\eta(1295)$	–	1294	0	0	1/2
$\pi(1300)^+$	$\pi(1300)^-$	1300	+1	0	1
$\pi(1300)^0$	–	1300	0	0	1/2
$a_2(1320)^+$	$a_2(1320)^-$	1318.3	+1	2	5
$a_2(1320)^0$	–	1318.3	0	2	5/2
$f_0(1370)$	–	1370	0	0	1/2
$\pi_1(1400)^+$	$\pi_1(1400)^+$	1354	+1	1	3
$\pi_1(1400)^0$	–	1354	0	1	3/2
$\eta(1405)$	–	1408.8	0	0	1/2
$f_1(1420)$	–	1426.4	0	1	3/2
$\omega(1420)$	–	1420	0	1	3/2
$a_0(1450)^+$	$a_0(1450)^-$	1474	+1	0	1
$a_0(1450)^0$	–	1474	0	0	1/2
$\rho(1450)^+$	$\rho(1450)^-$	1465	+1	1	3
$\rho(1450)^0$	–	1465	0	1	3/2
$\eta(1475)$	–	1476	0	0	1/2
$f_0(1500)$	–	1504	0	0	1/2
$f_2\prime(1525)$	–	1525	0	2	5/2
$\pi_1(1600)^+$	$\pi_1(1600)^-$	1662	+1	1	3
$\pi_1(1600)^0$	–	1662	0	1	3/2
$\eta_2(1645)$	–	1617	0	2	5/2
$\omega(1650)$	–	1670	0	1	3/2
$\omega_3(1670)$	–	1667	0	3	7/2
$\pi_2(1670)^+$	$\pi_2(1670)^-$	1672.2	+1	2	5
$\pi_2(1670)^0$	–	1672.2	0	2	5/2
$\phi(1680)$	–	1680	0	1	3/2
$\rho_3(1690)^+$	$\rho_3(1690)^-$	1688.8	+1	3	7
$\rho_3(1690)^0$	–	1688.8	0	3	7/2
$\rho(1700)^+$	$\rho(1700)^-$	1720	+1	1	3
$\rho(1700)^0$	–	1720	0	1	3/2
$f_0(1710)$	–	1723	0	0	1/2
$\pi(1800)^+$	$\pi(1800)^-$	1812	+1	0	1
$\pi(1800)^0$	–	1812	0	0	1/2
$\phi_3(1850)$	–	1854	0	3	7/2
$\pi_2(1880)^+$	$\pi_2(1880)^-$	1895	+1	2	5
$\pi_2(1880)^0$	–	1895	0	2	5/2
$f_2(1950)$	–	1944	0	2	5/2
$f_2(2010)$	–	2011	0	2	5/2
$a_4(2040)^+$	$a_4(2040)^-$	1995	+1	4	9
$a_4(2040)^0$	–	1995	0	4	9/2
$f_4(2050)$	–	2018	0	4	9/2
$\phi(2170)$	–	2188	0	1	3/2
$f_2(2300)$	–	2297	0	2	5/2
$f_2(2340)$	–	2345	0	2	5/2

Table A.3: Strange mesons with $S = \pm 1$, $C = B = 0$. $K^+ = u\bar{s}$, $K^0 = d\bar{s}$, $\bar{K}^0 = \bar{d}s$, $K^- = \bar{u}s$. $K^0 = 50\%K_s^0 + 50\%K_l^0$. $K_0^*(700)$ needs confirmation but is included in the summary table and thus has been considered in the calculations. For $K^*(892)^\pm$ hadron produced and τ–lepton-decay produced masses are quoted. The hadron produced mass $m_{K^*(892)^\pm} = 891.76$ MeV has been used in the calculations.

		m_i [MeV]	q_i [e]	s_i	g_i
K^+	K^-	493.677	+1	0	+1
K^0	$\bar{K}^0$	497.611	0	0	1
$K_0^*(700)^+$	$K_0^*(700)^-$	700	+1	0	1
$K_0^*(700)^0$	$\bar{K}_0^*(700)$	700	0	0	1
$K^*(892)^+$	$K^*(892)^-$	891.76	+1	1	3
		895.5	+1	1	3
$K^*(892)^0$	$\bar{K}^*(892)^0$	895.55	0	1	3
$K_1(1270)^+$	$K_1(1270)^-$	1272	+1	1	3
$K_1(1270)^0$	$\bar{K}_1(1270)^0$	1272	0	1	3
$K_1(1400)^+$	$K_1(1400)^-$	1403	+1	1	3
$K_1(1400)^0$	$\bar{K}_1(1400)^0$	1403	0	1	3
$K^*(1410)^+$	$K^*(1410)^-$	1421	+1	1	3
$K^*(1410)^0$	$\bar{K}^*(1410)^0$	1421	0	1	3
$K_0^*(1430)^+$	$K_0^*(1430)^-$	1425	+1	0	1
$K_0^*(1430)^0$	$\bar{K}_0^*(1430)^0$	1425	0	0	1
$K_2^*(1430)^+$	$K_2^*(1430)^-$	1425.6	+1	2	5
$K_2^*(1430)^0$	$\bar{K}_2^*(1430)^0$	1432.4	0	2	5
$K^*(1680)^+$	$K^*(1680)^-$	1718	+1	1	3
$K^*(1680)^0$	$\bar{K}^*(1680)^0$	1718	0	1	3
$K_2(1770)^+$	$K_2(1770)^-$	1773	+1	2	5
$K_2(1770)^0$	$\bar{K}_2(1770)^0$	1773	0	2	5
$K_3^*(1780)^+$	$K_3^*(1780)^-$	1776	+1	3	7
$K_3^*(1780)^0$	$\bar{K}_3^*(1780)^0$	1776	0	3	7
$K_2(1820)^+$	$K_2(1820)^-$	1819	+1	2	5
$K_2(1820)^0$	$\bar{K}_2(1820)^0$	1819	0	2	5
$K_4^*(2045)^+$	$K_4^*(2045)^-$	2045	+1	4	9
$K_4^*(2045)^0$	$\bar{K}_4^*(2045)^0$	2045	0	4	9

Table A.4: Charmed mesons with $C = \pm 1$, $S = B = 0$. $D^+ = c\bar{d}$, $D^0 = c\bar{u}$, $\bar{D}^0 = \bar{c}u$, $D^- = \bar{c}d$.

		m_i [MeV]	q_i [e]	s_i	g_i
D^+	D^-	1869.65	+1	0	1
D^0	$\bar{D}^0$	1864.83	0	0	1
$D^*(2007)^0$	$\bar{D}^*(2007)^0$	2006.85	0	1	3
$D^*(2010)^+$	$D^*(2010)^-$	2010.26	+1	1	3
$D_0^*(2400)^0$	$\bar{D}_0^*(2400)^0$	2318	0	0	1

Table A.5: Charmed and strange mesons with $C = S = \pm 1$, $B = 0$. $D_s^+ = c\bar{s}$, $D_s^- = \bar{c}s$.

		m_i [MeV]	q_i [e]	s_i	g_i
D_s^+	D_s^-	1968.34	+1	0	1
D_s^{*+}	D_s^{*-}	2112.2	+1	1	3
$D_{s0}^*(2317)^+$	$D_{s0}^*(2317)^-$	2317.7	+1	0	1

Table A.6: $p,\ n,\ N$ baryons and resonances with $S = 0$. $(p,\ N^+)$: *uud*. $(n,\ N^0)$: *udd*. Breit–Wigner masses used for resonance masses.

		m_i [MeV]	q_i [e]	s_i	g_i
p	$\bar{p}$	938.272	+1	1/2	2
n	$\bar{n}$	939.565	0	1/2	2
$N(1440)^+$	$N(1440)^-$	1440	+1	1/2	2
$N(1440)^0$	$\bar{N}(1440)^0$	1440	0	1/2	2
$N(1520)^+$	$N(1520)^-$	1515	+1	3/2	4
$N(1520)^0$	$\bar{N}(1520)^0$	1515	0	3/2	4
$N(1535)^+$	$N(1535)^-$	1530	+1	1/2	2
$N(1535)^0$	$\bar{N}(1535)^0$	1530	0	1/2	2
$N(1650)^+$	$N(1650)^-$	1650	+1	1/2	2
$N(1650)^0$	$\bar{N}(1650)^0$	1650	0	1/2	2
$N(1675)^+$	$N(1675)^-$	1675	+1	5/2	6
$N(1675)^0$	$\bar{N}(1675)^0$	1675	0	5/2	6
$N(1680)^+$	$N(1680)^-$	1685	+1	5/2	6
$N(1680)^0$	$\bar{N}(1680)^0$	1685	0	5/2	6
$N(1700)^+$	$N(1700)^-$	1720	+1	3/2	4
$N(1700)^0$	$\bar{N}(1700)^0$	1720	0	3/2	4
$N(1710)^+$	$N(1710)^-$	1710	+1	1/2	2
$N(1710)^0$	$\bar{N}(1710)^0$	1710	+1	1/2	2
$N(1720)^+$	$N(1720)^-$	1720	+1	3/2	4
$N(1720)^0$	$\bar{N}(1720)^0$	1720	0	3/2	4
$N(1875)^+$	$N(1875)^-$	1875	+1	3/2	4
$N(1875)^0$	$\bar{N}(1875)^0$	1875	0	3/2	4
$N(1880)^+$	$N(1880)^-$	1880	+1	1/2	2
$N(1880)^0$	$\bar{N}(1880)^0$	1880	0	1/2	2
$N(1895)^+$	$N(1895)^-$	1895	+1	1/2	2
$N(1895)^0$	$\bar{N}(1895)^0$	1895	0	1/2	2
$N(1900)^+$	$N(1900)^-$	1920	+1	3/2	4
$N(1900)^0$	$\bar{N}(1900)^0$	1920	0	3/2	4
$N(2060)^+$	$N(2060)^-$	2100	+1	5/2	6
$N(2060)^0$	$\bar{N}(2060)^0$	2100	0	5/2	6
$N(2100)^+$	$N(2100)^-$	2100	+1	1/2	2
$N(2100)^0$	$\bar{N}(2100)^0$	2100	0	1/2	2
$N(2120)^+$	$N(2120)^-$	2120	+1	3/2	4
$N(2120)^0$	$\bar{N}(2120)^0$	2120	0	3/2	4
$N(2190)^+$	$N(2190)^-$	2180	+1	7/2	8
$N(2190)^0$	$\bar{N}(2190)^0$	2180	0	7/2	8
$N(2220)^+$	$N(2220)^-$	2250	+1	9/2	10
$N(2220)^0$	$\bar{N}(2220)^0$	2250	0	9/2	10
$N(2250)^+$	$N(2250)^-$	2280	+1	9/2	10
$N(2250)^0$	$\bar{N}(2250)^0$	2280	0	9/2	10

Table A.7: Δ baryons with $S = 0$. $\Delta^{++} = uuu$, $\Delta^{+} = uud$, $\Delta^{0} = udd$, $\Delta^{-} = ddd$. Breit–Wigner masses used for resonance masses.

		m_i [MeV]	q_i [e]	s_i	g_i
$\Delta(1232)^{++}$	$\bar{\Delta}(1232)^{++}$	1232	+2	3/2	4
$\Delta(1232)^{+}$	$\bar{\Delta}(1232)^{+}$	1232	+1	3/2	4
$\Delta(1232)^{0}$	$\bar{\Delta}(1232)^{0}$	1232	0	3/2	4
$\Delta(1232)^{-}$	$\bar{\Delta}(1232)^{-}$	1232	−1	3/2	4
$\Delta(1600)^{++}$	$\bar{\Delta}(1600)^{++}$	1570	+2	3/2	4
$\Delta(1600)^{+}$	$\bar{\Delta}(1600)^{+}$	1570	+1	3/2	4
$\Delta(1600)^{0}$	$\bar{\Delta}(1600)^{0}$	1570	0	3/2	4
$\Delta(1600)^{-}$	$\bar{\Delta}(1600)^{-}$	1570	−1	3/2	4
$\Delta(1620)^{++}$	$\bar{\Delta}(1620)^{++}$	1610	+2	1/2	2
$\Delta(1620)^{+}$	$\bar{\Delta}(1620)^{+}$	1610	+1	1/2	2
$\Delta(1620)^{0}$	$\bar{\Delta}(1620)^{0}$	1610	0	1/2	2
$\Delta(1620)^{-}$	$\bar{\Delta}(1620)^{-}$	1610	−1	1/2	2
$\Delta(1700)^{++}$	$\bar{\Delta}(1700)^{++}$	1710	+2	3/2	4
$\Delta(1700)^{+}$	$\bar{\Delta}(1700)^{+}$	1710	+1	3/2	4
$\Delta(1700)^{0}$	$\bar{\Delta}(1700)^{0}$	1710	0	3/2	4
$\Delta(1700)^{-}$	$\bar{\Delta}(1700)^{-}$	1710	−1	3/2	4
$\Delta(1900)^{++}$	$\bar{\Delta}(1900)^{++}$	1860	+2	1/2	2
$\Delta(1900)^{+}$	$\bar{\Delta}(1900)^{+}$	1860	+1	1/2	2
$\Delta(1900)^{0}$	$\bar{\Delta}(1900)^{0}$	1860	0	1/2	2
$\Delta(1900)^{-}$	$\bar{\Delta}(1900)^{-}$	1860	−1	1/2	2
$\Delta(1905)^{++}$	$\bar{\Delta}(1905)^{++}$	1880	+2	5/2	6
$\Delta(1905)^{+}$	$\bar{\Delta}(1905)^{+}$	1880	+1	5/2	6
$\Delta(1905)^{0}$	$\bar{\Delta}(1905)^{0}$	1880	0	5/2	6
$\Delta(1905)^{-}$	$\bar{\Delta}(1905)^{-}$	1880	−1	5/2	6
$\Delta(1910)^{++}$	$\bar{\Delta}(1910)^{++}$	1900	+2	1/2	2
$\Delta(1910)^{+}$	$\bar{\Delta}(1910)^{+}$	1900	+1	1/2	2
$\Delta(1910)^{0}$	$\bar{\Delta}(1910)^{0}$	1900	0	1/2	2
$\Delta(1910)^{-}$	$\bar{\Delta}(1910)^{-}$	1900	−1	1/2	2
$\Delta(1920)^{++}$	$\bar{\Delta}(1920)^{++}$	1920	+2	3/2	4
$\Delta(1920)^{+}$	$\bar{\Delta}(1920)^{+}$	1920	+1	3/2	4
$\Delta(1920)^{0}$	$\bar{\Delta}(1920)^{0}$	1920	0	3/2	4
$\Delta(1920)^{-}$	$\bar{\Delta}(1920)^{-}$	1920	−1	3/2	4
$\Delta(1930)^{++}$	$\bar{\Delta}(1930)^{++}$	1950	+2	5/2	6
$\Delta(1930)^{+}$	$\bar{\Delta}(1930)^{+}$	1950	+1	5/2	6
$\Delta(1930)^{0}$	$\bar{\Delta}(1930)^{0}$	1950	0	5/2	6
$\Delta(1930)^{-}$	$\bar{\Delta}(1930)^{-}$	1950	−1	5/2	6
$\Delta(1950)^{++}$	$\bar{\Delta}(1950)^{++}$	1930	+2	7/2	8
$\Delta(1950)^{+}$	$\bar{\Delta}(1950)^{+}$	1930	+1	7/2	8
$\Delta(1950)^{0}$	$\bar{\Delta}(1950)^{0}$	1930	0	7/2	8
$\Delta(1950)^{-}$	$\bar{\Delta}(1950)^{-}$	1930	−1	7/2	8
$\Delta(2200)^{++}$	$\bar{\Delta}(2200)^{++}$	2200	+2	7/2	8
$\Delta(2200)^{+}$	$\bar{\Delta}(2200)^{+}$	2200	+1	7/2	8
$\Delta(2200)^{0}$	$\bar{\Delta}(2200)^{0}$	2200	0	7/2	8
$\Delta(2200)^{-}$	$\bar{\Delta}(2200)^{-}$	2200	−1	7/2	8

Table A.8: Λ baryons with $S = -1$. $\Lambda^0 = uds$.

		m_i [MeV]	q_i [e]	s_i	g_i
Λ	$\bar{\Lambda}$	1115.683	0	1/2	2
$\Lambda(1405)$	$\bar{\Lambda}(1405)$	1405.1	0	1/2	2
$\Lambda(1520)$	$\bar{\Lambda}(1520)$	1519.5	0	3/2	4
$\Lambda(1600)$	$\bar{\Lambda}(1600)$	1600	0	1/2	2
$\Lambda(1670)$	$\bar{\Lambda}(1670)$	1670	0	1/2	2
$\Lambda(1690)$	$\bar{\Lambda}(1690)$	1690	0	3/2	4
$\Lambda(1800)$	$\bar{\Lambda}(1800)$	1800	0	1/2	2
$\Lambda(1810)$	$\bar{\Lambda}(1810)$	1810	0	1/2	2
$\Lambda(1820)$	$\bar{\Lambda}(1820)$	1820	0	5/2	6
$\Lambda(1830)$	$\bar{\Lambda}(1830)$	1830	0	5/2	6
$\Lambda(1890)$	$\bar{\Lambda}(1890)$	1890	0	3/2	4
$\Lambda(2100)$	$\bar{\Lambda}(2100)$	2100	0	7/2	8
$\Lambda(2110)$	$\bar{\Lambda}(2110)$	2110	0	5/2	6
$\Lambda(2350)$	$\bar{\Lambda}(2350)$	2350	0	9/2	10

Table A.9: Σ baryons with $S = -1$. $\Sigma^+ = uus$, $\Sigma^0 = uds$, $\Sigma^- = dds$.

		m_i [MeV]	q_i [e]	s_i	g_i
Σ^+	$\bar{\Sigma}^+$	1189.37	+1	1/2	2
Σ^0	$\bar{\Sigma}^0$	1192.642	0	1/2	2
Σ^-	$\bar{\Sigma}^-$	1197.449	−1	1/2	2
$\Sigma(1385)^+$	$\bar{\Sigma}(1385)^+$	1382.8	+1	3/2	4
$\Sigma(1385)^0$	$\bar{\Sigma}(1385)^0$	1383.7	0	3/2	4
$\Sigma(1385)^-$	$\bar{\Sigma}(1385)^-$	1387.2	−1	3/2	4
$\Sigma(1600)^+$	$\bar{\Sigma}(1600)^+$	1660	+1	1/2	2
$\Sigma(1600)^0$	$\bar{\Sigma}(1600)^0$	1660	0	1/2	2
$\Sigma(1600)^-$	$\bar{\Sigma}(1600)^-$	1660	−1	1/2	2
$\Sigma(1670)^+$	$\bar{\Sigma}(1670)^+$	1670	+1	3/2	4
$\Sigma(1670)^0$	$\bar{\Sigma}(1670)^0$	1670	0	3/2	4
$\Sigma(1670)^-$	$\bar{\Sigma}(1670)^-$	1670	−1	3/2	4
$\Sigma(1750)^+$	$\bar{\Sigma}(1750)^+$	1750	+1	1/2	2
$\Sigma(1750)^0$	$\bar{\Sigma}(1750)^0$	1750	0	1/2	2
$\Sigma(1750)^-$	$\bar{\Sigma}(1750)^-$	1750	−1	1/2	2
$\Sigma(1775)^+$	$\bar{\Sigma}(1775)^+$	1775	+1	5/2	6
$\Sigma(1775)^0$	$\bar{\Sigma}(1775)^0$	1775	0	5/2	6
$\Sigma(1775)^-$	$\bar{\Sigma}(1775)^-$	1775	−1	5/2	6
$\Sigma(1915)^+$	$\bar{\Sigma}(1915)^+$	1915	+1	5/2	6
$\Sigma(1915)^0$	$\bar{\Sigma}(1915)^0$	1915	0	5/2	6
$\Sigma(1915)^-$	$\bar{\Sigma}(1915)^-$	1915	−1	5/2	6
$\Sigma(1940)^+$	$\bar{\Sigma}(1940)^+$	1940	+1	3/2	4
$\Sigma(1940)^0$	$\bar{\Sigma}(1940)^0$	1940	0	3/2	4
$\Sigma(1940)^-$	$\bar{\Sigma}(1940)^-$	1940	−1	3/2	4
$\Sigma(2030)^+$	$\bar{\Sigma}(2030)^+$	2030	+1	7/2	8
$\Sigma(2030)^0$	$\bar{\Sigma}(2030)^0$	2030	0	7/2	8
$\Sigma(2030)^-$	$\bar{\Sigma}(2030)^-$	2030	−1	7/2	8
$\Sigma(2250)^+$	$\bar{\Sigma}(2250)^+$	2250	+1	?	?
$\Sigma(2250)^0$	$\bar{\Sigma}(2250)^0$	2250	0	?	?
$\Sigma(2250)^-$	$\bar{\Sigma}(2250)^-$	2250	−1	?	?

Table A.10: Ξ baryons with $S = -2$. $\Xi^0 = uss$, $\Xi^- = dss$.

		m_i [MeV]	q_i [e]	s_i	g_i
Ξ^0	$\bar{\Xi}^0$	1314.86	0	1/2	2
Ξ^-	$\bar{\Xi}^-$	1321.71	−1	1/2	2
$\Xi(1530)^0$	$\bar{\Xi}(1530)^0$	1531.8	0	3/2	4
$\Xi(1530)^-$	$\bar{\Xi}(1530)^-$	1535.0	−1	3/2	4
$\Xi(1690)^0$	$\bar{\Xi}(1690)^0$	1690	0	?	?
$\Xi(1690)^-$	$\bar{\Xi}(1690)^-$	1690	−1	?	?
$\Xi(1820)^0$	$\bar{\Xi}(1820)^0$	1823	0	3/2	4
$\Xi(1820)^-$	$\bar{\Xi}(1820)^-$	1823	−1	3/2	4
$\Xi(1950)^0$	$\bar{\Xi}(1950)^0$	1950	0	?	?
$\Xi(1950)^-$	$\bar{\Xi}(1950)^-$	1950	−1	?	?
$\Xi(2030)^0$	$\bar{\Xi}(2030)^0$	2025	0	$\geq 5/2$	≥ 6
$\Xi(2030)^-$	$\bar{\Xi}(2030)^-$	2025	−1	$\geq 5/2$	≥ 6

Table A.11: Ω baryons with $S = -3$. $\Omega^- = sss$.

		m_i [MeV]	q_i [e]	s_i	g_i
Ω^-	$\bar{\Omega}^-$	1672.45	−1	3/2	4
$\Omega(2250)^-$	$\bar{\Omega}(2250)^-$	2252	−1	?	?

Table A.12: Charmed baryons with $C = +1$. $\Lambda_c^+ = udc$.

		m_i [MeV]	q_i [e]	s_i	g_i
Λ_c^+	$\bar{\Lambda}_c^+$	2286.46	+1	1/2	2

References

[1] M. M. Wygas, I. M. Oldengott, D. Bödeker, and D. J. Schwarz, "Cosmic QCD Epoch at Nonvanishing Lepton Asymmetry," *Phys. Rev. Lett.* **121** (2018) 201302, arXiv:1807.10815 [hep-ph].

[2] D. J. Schwarz and M. Stuke, "Lepton asymmetry and the cosmic QCD transition," *JCAP* **0911** (2009) 025, arXiv:0906.3434 [hep-ph]. [Erratum: JCAP1010,E01(2010)].

[3] **Particle Data Group** Collaboration, M. Tanabashi *et al.*, "Review of Particle Physics," *Phys. Rev.* **D98** (2018) no. 3, 030001.

[4] E. W. Kolb and M. S. Turner, "Grand Unified Theories and the Origin of the Baryon Asymmetry," *Ann. Rev. Nucl. Part. Sci.* **33** (1983) 645–696.

[5] M. Fukugita and T. Yanagida, "Baryogenesis Without Grand Unification," *Phys. Lett.* **B174** (1986) 45–47.

[6] J. A. Harvey and M. S. Turner, "Cosmological baryon and lepton number in the presence of electroweak fermion number violation," *Phys. Rev.* **D42** (1990) 3344–3349.

[7] M. Shaposhnikov, "The nuMSM, leptonic asymmetries, and properties of singlet fermions," *JHEP* **08** (2008) 008, arXiv:0804.4542 [hep-ph].

[8] L. Canetti, M. Drewes, T. Frossard, and M. Shaposhnikov, "Dark Matter, Baryogenesis and Neutrino Oscillations from Right Handed Neutrinos," *Phys. Rev.* **D87** (2013) 093006, arXiv:1208.4607 [hep-ph].

[9] S. Eijima and M. Shaposhnikov, "Fermion number violating effects in low scale leptogenesis," *Phys. Lett.* **B771** (2017) 288–296, arXiv:1703.06085 [hep-ph].

[10] J. Ghiglieri and M. Laine, "Precision study of GeV-scale resonant leptogenesis," arXiv:1811.01971 [hep-ph].

[11] D. A. Kirzhnits and A. D. Linde, "Symmetry Behavior in Gauge Theories," *Annals Phys.* **101** (1976) 195–238.

[12] J. Liu and G. Segre, "Baryon asymmetry of the universe and large lepton asymmetries," *Phys. Lett.* **B338** (1994) 259–262.

[13] J. McDonald, "Symmetry nonrestoration via order 10**-10 B and L

asymmetries," *Phys. Lett.* **B463** (1999) 225–229, arXiv:hep-ph/9907358 [hep-ph].

[14] J. A. Harvey and E. W. Kolb, "Grand Unified Theories and the Lepton Number of the Universe," *Phys. Rev.* **D24** (1981) 2090.

[15] A. Casas, W. Y. Cheng, and G. Gelmini, "Generation of large lepton asymmetries," *Nucl. Phys.* **B538** (1999) 297–308, arXiv:hep-ph/9709289 [hep-ph].

[16] G. Barenboim and W.-I. Park, "A full picture of large lepton number asymmetries of the Universe," *JCAP* **1704** (2017) no. 04, 048, arXiv:1703.08258 [hep-ph].

[17] C. Caprini, S. Biller, and P. G. Ferreira, "Constraints on the electrical charge asymmetry of the universe," *JCAP* **0502** (2005) 006, arXiv:hep-ph/0310066 [hep-ph].

[18] I. M. Oldengott and D. J. Schwarz, "Improved constraints on lepton asymmetry from the cosmic microwave background," *EPL* **119** (2017) no. 2, 29001, arXiv:1706.01705 [astro-ph.CO].

[19] G. Mangano, G. Miele, S. Pastor, O. Pisanti, and S. Sarikas, "Updated BBN bounds on the cosmological lepton asymmetry for non-zero θ_{13}," *Phys. Lett.* **B708** (2012) 1–5, arXiv:1110.4335 [hep-ph].

[20] A. D. Dolgov, S. H. Hansen, S. Pastor, S. T. Petcov, G. G. Raffelt, and D. V. Semikoz, "Cosmological bounds on neutrino degeneracy improved by flavor oscillations," *Nucl. Phys.* **B632** (2002) 363–382, arXiv:hep-ph/0201287 [hep-ph].

[21] Y. Y. Y. Wong, "Analytical treatment of neutrino asymmetry equilibration from flavor oscillations in the early universe," *Phys. Rev.* **D66** (2002) 025015, arXiv:hep-ph/0203180 [hep-ph].

[22] A. Bazavov *et al.*, "Chiral crossover in QCD at zero and non-zero chemical potentials," arXiv:1812.08235 [hep-lat].

[23] M. Buballa, "NJL model analysis of quark matter at large density," *Phys. Rept.* **407** (2005) 205–376, arXiv:hep-ph/0402234 [hep-ph].

[24] M. Asakawa and K. Yazaki, "Chiral Restoration at Finite Density and Temperature," *Nucl. Phys.* **A504** (1989) 668–684.

[25] M. A. Stephanov, K. Rajagopal, and E. V. Shuryak, "Signatures of the

tricritical point in QCD," *Phys. Rev. Lett.* **81** (1998) 4816–4819, arXiv:hep-ph/9806219 [hep-ph].

[26] M. A. Stephanov, "QCD phase diagram and the critical point," *Prog. Theor. Phys. Suppl.* **153** (2004) 139–156, arXiv:hep-ph/0402115 [hep-ph]. [Int. J. Mod. Phys.A20,4387(2005)].

[27] Y. Aoki, G. Endrodi, Z. Fodor, S. D. Katz, and K. K. Szabo, "The Order of the quantum chromodynamics transition predicted by the standard model of particle physics," *Nature* **443** (2006) 675–678, arXiv:hep-lat/0611014 [hep-lat].

[28] T. Bhattacharya *et al.*, "QCD Phase Transition with Chiral Quarks and Physical Quark Masses," *Phys. Rev. Lett.* **113** (2014) no. 8, 082001, arXiv:1402.5175 [hep-lat].

[29] O. Philipsen, "Exploring the QCD phase diagram," *PoS* **CPOD07** (2007) 028, arXiv:0710.1217 [hep-ph].

[30] C. Schmidt, "QCD thermodynamics at zero and non-zero density," *PoS* **CPOD2006** (2006) 002, arXiv:hep-lat/0701019 [hep-lat].

[31] H.-T. Ding, "Lattice QCD at nonzero temperature and density," *PoS* **LATTICE2016** (2017) 022, arXiv:1702.00151 [hep-lat].

[32] K. Zarembo, "Lepton asymmetry of the universe and charged quark gluon plasma," *Phys. Lett.* **B493** (2000) 375–379, arXiv:hep-ph/0008264 [hep-ph].

[33] D. J. Schwarz, "The first second of the universe," *Annalen Phys.* **12** (2003) 220–270, arXiv:astro-ph/0303574 [astro-ph].

[34] E. Witten, "Cosmic Separation of Phases," *Phys. Rev.* **D30** (1984) 272–285.

[35] H. Abuki, T. Brauner, and H. J. Warringa, "Pion condensation in a dense neutrino gas," *Eur. Phys. J.* **C64** (2009) 123–131, arXiv:0901.2477 [hep-ph].

[36] B. B. Brandt, G. Endrodi, and S. Schmalzbauer, "QCD phase diagram for nonzero isospin-asymmetry," *Phys. Rev.* **D97** (2018) no. 5, 054514, arXiv:1712.08190 [hep-lat].

[37] C. Tiburzi, "Pulsars probe the low-frequency gravitational sky: Pulsar Timing Arrays basics and recent results," *Publ. Astron. Soc. Austral.* **35** (2018) e013, arXiv:1802.05076 [astro-ph.IM].

[38] M. J. Fromerth and J. Rafelski, "Hadronization of the quark Universe," arXiv:astro-ph/0211346 [astro-ph].

[39] J. Ghiglieri and M. Laine, "Improved determination of sterile neutrino dark matter spectrum," *JHEP* **11** (2015) 171, arXiv:1506.06752 [hep-ph].

[40] T. Venumadhav, F.-Y. Cyr-Racine, K. N. Abazajian, and C. M. Hirata, "Sterile neutrino dark matter: Weak interactions in the strong coupling epoch," *Phys. Rev.* **D94** (2016) no. 4, 043515, arXiv:1507.06655 [astro-ph.CO].

[41] D. Clowe, M. Bradac, A. H. Gonzalez, M. Markevitch, S. W. Randall, C. Jones, and D. Zaritsky, "A direct empirical proof of the existence of dark matter," *Astrophys. J.* **648** (2006) L109–L113, arXiv:astro-ph/0608407 [astro-ph].

[42] **Planck** Collaboration, N. Aghanim *et al.*, "Planck 2018 results. VI. Cosmological parameters," arXiv:1807.06209 [astro-ph.CO].

[43] A. Coc, J.-P. Uzan, and E. Vangioni, "Standard big bang nucleosynthesis and primordial CNO Abundances after Planck," *JCAP* **1410** (2014) 050, arXiv:1403.6694 [astro-ph.CO].

[44] V. A. Rubakov and D. S. Gorbunov, *Introduction to the Theory of the Early Universe: Hot Big Bang Theory*. World Scientific, Singapore, 2011.

[45] F. Karsch, T. Neuhaus, A. Patkos, and J. Rank, "Critical Higgs mass and temperature dependence of gauge boson masses in the SU(2) gauge Higgs model," *Nucl. Phys. Proc. Suppl.* **53** (1997) 623–625, arXiv:hep-lat/9608087 [hep-lat].

[46] K. Kajantie, M. Laine, K. Rummukainen, and M. E. Shaposhnikov, "Is there a hot electroweak phase transition at m(H) larger or equal to m(W)?," *Phys. Rev. Lett.* **77** (1996) 2887–2890, arXiv:hep-ph/9605288 [hep-ph].

[47] M. Gurtler, E.-M. Ilgenfritz, and A. Schiller, "Where the electroweak phase transition ends," *Phys. Rev.* **D56** (1997) 3888–3895, arXiv:hep-lat/9704013 [hep-lat].

[48] F. Csikor, Z. Fodor, and J. Heitger, "Endpoint of the hot electroweak phase transition," *Phys. Rev. Lett.* **82** (1999) 21–24, arXiv:hep-ph/9809291 [hep-ph].

[49] M. Laine and Y. Schroder, "Quark mass thresholds in QCD

thermodynamics," *Phys. Rev.* **D73** (2006) 085009, arXiv:hep-ph/0603048 [hep-ph].

[50] G. Steigman, "Primordial Nucleosynthesis in the Precision Cosmology Era," *Ann. Rev. Nucl. Part. Sci.* **57** (2007) 463–491, arXiv:0712.1100 [astro-ph].

[51] E. W. Kolb and M. S. Turner, "The Early Universe," *Nature* **294** (1981) 521.

[52] B. B. Brandt, G. Endrodi, E. S. Fraga, M. Hippert, J. Schaffner-Bielich, and S. Schmalzbauer, "A new class of compact stars: pion stars," arXiv:1802.06685 [hep-ph].

[53] L. D. Landau and E. M. Lifšic, *Statistical physics*, vol. 5 of *Course of theoretical physics; 5.* Pergamon Pr., Oxford, 2., rev. and enl. ed., 2. impr ed., 1970.

[54] A. D. Sakharov, "Violation of CP Invariance, C asymmetry, and baryon asymmetry of the universe," *Pisma Zh. Eksp. Teor. Fiz.* **5** (1967) 32–35. [Usp. Fiz. Nauk161,no.5,61(1991)].

[55] W. Buchmuller, R. D. Peccei, and T. Yanagida, "Leptogenesis as the origin of matter," *Ann. Rev. Nucl. Part. Sci.* **55** (2005) 311–355, arXiv:hep-ph/0502169 [hep-ph].

[56] S. Davidson, E. Nardi, and Y. Nir, "Leptogenesis," *Phys. Rept.* **466** (2008) 105–177, arXiv:0802.2962 [hep-ph].

[57] G. Mangano, G. Miele, S. Pastor, T. Pinto, O. Pisanti, and P. D. Serpico, "Relic neutrino decoupling including flavor oscillations," *Nucl. Phys.* **B729** (2005) 221–234, arXiv:hep-ph/0506164 [hep-ph].

[58] P. F. de Salas and S. Pastor, "Relic neutrino decoupling with flavour oscillations revisited," *JCAP* **1607** (2016) no. 07, 051, arXiv:1606.06986 [hep-ph].

[59] G. Mangano, G. Miele, S. Pastor, O. Pisanti, and S. Sarikas, "Constraining the cosmic radiation density due to lepton number with Big Bang Nucleosynthesis," *JCAP* **1103** (2011) 035, arXiv:1011.0916 [astro-ph.CO].

[60] S. Pastor, T. Pinto, and G. G. Raffelt, "Relic density of neutrinos with primordial asymmetries," *Phys. Rev. Lett.* **102** (2009) 241302, arXiv:0808.3137 [astro-ph].

[61] L. Johns, M. Mina, V. Cirigliano, M. W. Paris, and G. M. Fuller, "Neutrino flavor transformation in the lepton-asymmetric universe," *Phys. Rev.* **D94** (2016) no. 8, 083505, arXiv:1608.01336 [hep-ph].

[62] G. Barenboim, W. H. Kinney, and W.-I. Park, "Resurrection of large lepton number asymmetries from neutrino flavor oscillations," *Phys. Rev.* **D95** (2017) no. 4, 043506, arXiv:1609.01584 [hep-ph].

[63] C. Giunti and C. W. Kim, *Fundamentals of Neutrino Physics and Astrophysics*. Univ. Pr, Oxford, UK, 2007.

[64] G. Beaudet and P. Goret, "Leptonic numbers and the neutron to proton ratio in the hot big bang model," *Astron. Astrophys.* **49** (1976) 415–419.

[65] P. Di Bari and R. Foot, "Active sterile neutrino oscillations and BBN + CMBR constraints," *Phys. Rev.* **D63** (2001) 043008, arXiv:hep-ph/0008258 [hep-ph].

[66] E. Castorina, U. Franca, M. Lattanzi, J. Lesgourgues, G. Mangano, A. Melchiorri, and S. Pastor, "Cosmological lepton asymmetry with a nonzero mixing angle θ_{13}," *Phys. Rev.* **D86** (2012) 023517, arXiv:1204.2510 [astro-ph.CO].

[67] C. T. Yang, J. Birrell, and J. Rafelski, "Lepton Number and Expansion of the Universe," arXiv:1812.05157 [hep-ph].

[68] **Planck** Collaboration, P. A. R. Ade *et al.*, "Planck 2015 results. XIII. Cosmological parameters," *Astron. Astrophys.* **594** (2016) A13, arXiv:1502.01589 [astro-ph.CO].

[69] M. Drewes *et al.*, "A White Paper on keV Sterile Neutrino Dark Matter," *JCAP* **1701** (2017) no. 01, 025, arXiv:1602.04816 [hep-ph].

[70] M. D'Onofrio, K. Rummukainen, and A. Tranberg, "Sphaleron Rate in the Minimal Standard Model," *Phys. Rev. Lett.* **113** (2014) no. 14, 141602, arXiv:1404.3565 [hep-ph].

[71] I. Affleck and M. Dine, "A New Mechanism for Baryogenesis," *Nucl. Phys.* **B249** (1985) 361–380.

[72] D. J. Schwarz, "Evolution of gravitational waves through cosmological transitions," *Mod. Phys. Lett.* **A13** (1998) 2771–2778, arXiv:gr-qc/9709027 [gr-qc].

[73] Y. Watanabe and E. Komatsu, "Improved Calculation of the Primordial

Gravitational Wave Spectrum in the Standard Model," *Phys. Rev.* **D73** (2006) 123515, arXiv:astro-ph/0604176 [astro-ph].

[74] D. J. Gross and F. Wilczek, "Ultraviolet Behavior of Nonabelian Gauge Theories," *Phys. Rev. Lett.* **30** (1973) 1343–1346. [,271(1973)].

[75] H. D. Politzer, "Reliable Perturbative Results for Strong Interactions?," *Phys. Rev. Lett.* **30** (1973) 1346–1349. [,274(1973)].

[76] J. Engels, F. Karsch, H. Satz, and I. Montvay, "High Temperature SU(2) Gluon Matter on the Lattice," *Phys. Lett.* **101B** (1981) 89. [,293(1980)].

[77] L. D. McLerran and B. Svetitsky, "A Monte Carlo Study of SU(2) Yang-Mills Theory at Finite Temperature," *Phys. Lett.* **98B** (1981) 195. [,283(1980)].

[78] J. Kuti, J. Polónyi, and K. Szlachányi, "Monte Carlo study of SU (2) gauge theory at finite temperature," *AIP Conf. Proc.* **68** (1980) 906–910.

[79] H.-T. Ding, F. Karsch, and S. Mukherjee, "Thermodynamics of strong-interaction matter from Lattice QCD," *Int. J. Mod. Phys.* **E24** (2015) no. 10, 1530007, arXiv:1504.05274 [hep-lat].

[80] **Wuppertal-Budapest** Collaboration, S. Borsanyi, Z. Fodor, C. Hoelbling, S. D. Katz, S. Krieg, C. Ratti, and K. K. Szabo, "Is there still any T_c mystery in lattice QCD? Results with physical masses in the continuum limit III," *JHEP* **09** (2010) 073, arXiv:1005.3508 [hep-lat].

[81] A. Bazavov *et al.*, "The chiral and deconfinement aspects of the QCD transition," *Phys. Rev.* **D85** (2012) 054503, arXiv:1111.1710 [hep-lat].

[82] C. R. Allton, S. Ejiri, S. J. Hands, O. Kaczmarek, F. Karsch, E. Laermann, C. Schmidt, and L. Scorzato, "The QCD thermal phase transition in the presence of a small chemical potential," *Phys. Rev.* **D66** (2002) 074507, arXiv:hep-lat/0204010 [hep-lat].

[83] R. V. Gavai and S. Gupta, "Pressure and nonlinear susceptibilities in QCD at finite chemical potentials," *Phys. Rev.* **D68** (2003) 034506, arXiv:hep-lat/0303013 [hep-lat].

[84] Z. Fodor and S. D. Katz, "A New method to study lattice QCD at finite temperature and chemical potential," *Phys. Lett.* **B534** (2002) 87–92, arXiv:hep-lat/0104001 [hep-lat].

[85] P. de Forcrand and O. Philipsen, "The QCD phase diagram for small

densities from imaginary chemical potential," *Nucl. Phys.* **B642** (2002) 290–306, arXiv:hep-lat/0205016 [hep-lat].

[86] M. D'Elia and M.-P. Lombardo, "Finite density QCD via imaginary chemical potential," *Phys. Rev.* **D67** (2003) 014505, arXiv:hep-lat/0209146 [hep-lat].

[87] G. Aarts and I.-O. Stamatescu, "Stochastic quantization at finite chemical potential," *JHEP* **09** (2008) 018, arXiv:0807.1597 [hep-lat].

[88] G. Guralnik and C. Pehlevan, "Effective Potential for Complex Langevin Equations," *Nucl. Phys.* **B822** (2009) 349–366, arXiv:0902.1503 [hep-lat].

[89] **AuroraScience** Collaboration, M. Cristoforetti, F. Di Renzo, and L. Scorzato, "New approach to the sign problem in quantum field theories: High density QCD on a Lefschetz thimble," *Phys. Rev.* **D86** (2012) 074506, arXiv:1205.3996 [hep-lat].

[90] P. de Forcrand, "Simulating QCD at finite density," *PoS* **LAT2009** (2009) 010, arXiv:1005.0539 [hep-lat].

[91] P. Steinbrecher, "The QCD crossover at zero and non-zero baryon densities from Lattice QCD," arXiv:1807.05607 [hep-lat].

[92] S. Borsanyi *et al.*, "Calculation of the axion mass based on high-temperature lattice quantum chromodynamics," *Nature* **539** (2016) no. 7627, 69–71, arXiv:1606.07494 [hep-lat].

[93] F. Karsch, "Lattice QCD at high temperature and density," *Lect. Notes Phys.* **583** (2002) 209–249, arXiv:hep-lat/0106019 [hep-lat].

[94] A. Bazavov *et al.*, "The QCD Equation of State to $\mathcal{O}(\mu_B^6)$ from Lattice QCD," *Phys. Rev.* **D95** (2017) no. 5, 054504, arXiv:1701.04325 [hep-lat].

[95] W. Weise, "Nuclear chiral dynamics and phases of QCD," *Prog. Part. Nucl. Phys.* **67** (2012) 299–311, arXiv:1201.0950 [nucl-th].

[96] K. Fukushima and C. Sasaki, "The phase diagram of nuclear and quark matter at high baryon density," *Prog. Part. Nucl. Phys.* **72** (2013) 99–154, arXiv:1301.6377 [hep-ph].

[97] M. G. Alford, "Color superconducting quark matter," *Ann. Rev. Nucl. Part. Sci.* **51** (2001) 131–160, arXiv:hep-ph/0102047 [hep-ph].

[98] Y. Akiba *et al.*, "The Hot QCD White Paper: Exploring the Phases of QCD at RHIC and the LHC," arXiv:1502.02730 [nucl-ex].

[99] J. O. Andersen and M. Strickland, "Resummation in hot field theories," *Annals Phys.* **317** (2005) 281–353, arXiv:hep-ph/0404164 [hep-ph].

[100] N. Haque, A. Bandyopadhyay, J. O. Andersen, M. G. Mustafa, M. Strickland, and N. Su, "Three-loop HTLpt thermodynamics at finite temperature and chemical potential," *JHEP* **05** (2014) 027, arXiv:1402.6907 [hep-ph].

[101] N. Haque, "Quark mass dependent collective excitations and quark number susceptibilities within the hard thermal loop approximation," *Phys. Rev.* **D98** (2018) no. 1, 014013, arXiv:1804.04996 [hep-ph].

[102] N. Su, "A brief overview of hard-thermal-loop perturbation theory," *Commun. Theor. Phys.* **57** (2012) 409, arXiv:1204.0260 [hep-ph].

[103] E. Braaten and A. Nieto, "Effective field theory approach to high temperature thermodynamics," *Phys. Rev.* **D51** (1995) 6990–7006, arXiv:hep-ph/9501375 [hep-ph].

[104] K. Kajantie, M. Laine, K. Rummukainen, and Y. Schroder, "The Pressure of hot QCD up to $g^6 \ln(1/g)$," *Phys. Rev.* **D67** (2003) 105008, arXiv:hep-ph/0211321 [hep-ph].

[105] A. Vuorinen, "Quark number susceptibilities of hot QCD up to $g^6 \ln g$," *Phys. Rev.* **D67** (2003) 074032, arXiv:hep-ph/0212283 [hep-ph].

[106] A. Vuorinen, "The Pressure of QCD at finite temperatures and chemical potentials," *Phys. Rev.* **D68** (2003) 054017, arXiv:hep-ph/0305183 [hep-ph].

[107] A. Ipp, K. Kajantie, A. Rebhan, and A. Vuorinen, "The Pressure of deconfined QCD for all temperatures and quark chemical potentials," *Phys. Rev.* **D74** (2006) 045016, arXiv:hep-ph/0604060 [hep-ph].

[108] R. Bellwied, S. Borsanyi, Z. Fodor, S. D. Katz, A. Pasztor, C. Ratti, and K. K. Szabo, "Fluctuations and correlations in high temperature QCD," *Phys. Rev.* **D92** (2015) no. 11, 114505, arXiv:1507.04627 [hep-lat].

[109] M. Laine and M. Vepsalainen, "Mesonic correlation lengths in high temperature QCD," *JHEP* **02** (2004) 004, arXiv:hep-ph/0311268 [hep-ph].

[110] F. Karsch, K. Redlich, and A. Tawfik, "Hadron resonance mass spectrum

and lattice QCD thermodynamics," *Eur. Phys. J.* **C29** (2003) 549–556, arXiv:hep-ph/0303108 [hep-ph].

[111] F. Karsch, K. Redlich, and A. Tawfik, "Thermodynamics at nonzero baryon number density: A Comparison of lattice and hadron resonance gas model calculations," *Phys. Lett.* **B571** (2003) 67–74, arXiv:hep-ph/0306208 [hep-ph].

[112] S. Ejiri, F. Karsch, and K. Redlich, "Hadronic fluctuations at the QCD phase transition," *Phys. Lett.* **B633** (2006) 275–282, arXiv:hep-ph/0509051 [hep-ph].

[113] F. Karsch, "Conserved charge fluctuations at vanishing and non-vanishing chemical potential," *Nucl. Phys.* **A967** (2017) 461–464, arXiv:1706.01620 [hep-lat].

[114] R. Hagedorn, "Statistical thermodynamics of strong interactions at high-energies," *Nuovo Cim. Suppl.* **3** (1965) 147–186.

[115] R. Dashen, S.-K. Ma, and H. J. Bernstein, "S Matrix formulation of statistical mechanics," *Phys. Rev.* **187** (1969) 345–370.

[116] R. Venugopalan and M. Prakash, "Thermal properties of interacting hadrons," *Nucl. Phys.* **A546** (1992) 718–760.

[117] **HotQCD** Collaboration, A. Bazavov *et al.*, "Fluctuations and Correlations of net baryon number, electric charge, and strangeness: A comparison of lattice QCD results with the hadron resonance gas model," *Phys. Rev.* **D86** (2012) 034509, arXiv:1203.0784 [hep-lat].

[118] A. Bazavov *et al.*, "Additional Strange Hadrons from QCD Thermodynamics and Strangeness Freezeout in Heavy Ion Collisions," *Phys. Rev. Lett.* **113** (2014) no. 7, 072001, arXiv:1404.6511 [hep-lat].

[119] A. Bazavov *et al.*, "The melting and abundance of open charm hadrons," *Phys. Lett.* **B737** (2014) 210–215, arXiv:1404.4043 [hep-lat].

[120] **Hadron Spectrum** Collaboration, R. G. Edwards, N. Mathur, D. G. Richards, and S. J. Wallace, "Flavor structure of the excited baryon spectra from lattice QCD," *Phys. Rev.* **D87** (2013) no. 5, 054506, arXiv:1212.5236 [hep-ph].

[121] S. Capstick and N. Isgur, "Baryons in a Relativized Quark Model with

Chromodynamics," *Phys. Rev.* **D34** (1986) 2809. [AIP Conf. Proc.132,267(1985)].

[122] D. Ebert, R. N. Faustov, and V. O. Galkin, "Mass spectra and Regge trajectories of light mesons in the relativistic quark model," *Phys. Rev.* **D79** (2009) 114029, arXiv:0903.5183 [hep-ph].

[123] V. Vovchenko, A. Motornenko, P. Alba, M. I. Gorenstein, L. M. Satarov, and H. Stoecker, "Multicomponent van der Waals equation of state: Applications in nuclear and hadronic physics," *Phys. Rev.* **C96** (2017) no. 4, 045202, arXiv:1707.09215 [nucl-th].

[124] V. Vovchenko, P. Alba, M. I. Gorenstein, and H. Stoecker, "van der Waals Interactions and Hadron Resonance Gas: Role of resonance widths modeling on conserved charges fluctuations," *EPJ Web Conf.* **171** (2018) 14006, arXiv:1711.09863 [nucl-th].

[125] R. V. Gavai and S. Gupta, "The Critical end point of QCD," *Phys. Rev.* **D71** (2005) 114014, arXiv:hep-lat/0412035 [hep-lat].

[126] M. Cheng *et al.*, "The QCD equation of state with almost physical quark masses," *Phys. Rev.* **D77** (2008) 014511, arXiv:0710.0354 [hep-lat].

[127] A. Bazavov, H. T. Ding, P. Hegde, F. Karsch, C. Miao, S. Mukherjee, P. Petreczky, C. Schmidt, and A. Velytsky, "Quark number susceptibilities at high temperatures," *Phys. Rev.* **D88** (2013) no. 9, 094021, arXiv:1309.2317 [hep-lat].

[128] H. T. Ding, S. Mukherjee, H. Ohno, P. Petreczky, and H. P. Schadler, "Diagonal and off-diagonal quark number susceptibilities at high temperatures," *Phys. Rev.* **D92** (2015) no. 7, 074043, arXiv:1507.06637 [hep-lat].

[129] S. Borsanyi, Z. Fodor, J. N. Guenther, S. K. Katz, K. K. Szabo, A. Pasztor, I. Portillo, and C. Ratti, "Higher order fluctuations and correlations of conserved charges from lattice QCD," *JHEP* **10** (2018) 205, arXiv:1805.04445 [hep-lat].

[130] S. Borsanyi, Z. Fodor, S. D. Katz, S. Krieg, C. Ratti, and K. Szabo, "Fluctuations of conserved charges at finite temperature from lattice QCD," *JHEP* **01** (2012) 138, arXiv:1112.4416 [hep-lat].

[131] S. Mukherjee, P. Petreczky, and S. Sharma, "Charm degrees of freedom in

the quark gluon plasma," *Phys. Rev.* **D93** (2016) no. 1, 014502, arXiv:1509.08887 [hep-lat].

[132] W. H. Press, S. A. Teukolsky, W. T. Vetterling, and B. P. Flannery, *Numerical Recipes in C (2Nd Ed.): The Art of Scientific Computing*. Cambridge University Press, Cambridge, England, 1992.

[133] R. V. Gavai and S. Gupta, "Fluctuations, strangeness and quasi-quarks in heavy-ion collisions from lattice QCD," *Phys. Rev.* **D73** (2006) 014004, arXiv:hep-lat/0510044 [hep-lat].

[134] M. G. Alford, A. Kapustin, and F. Wilczek, "Imaginary chemical potential and finite fermion density on the lattice," *Phys. Rev.* **D59** (1999) 054502, arXiv:hep-lat/9807039 [hep-lat].

[135] D. T. Son and M. A. Stephanov, "QCD at finite isospin density," *Phys. Rev. Lett.* **86** (2001) 592–595, arXiv:hep-ph/0005225 [hep-ph].

[136] K. Splittorff, D. T. Son, and M. A. Stephanov, "QCD - like theories at finite baryon and isospin density," *Phys. Rev.* **D64** (2001) 016003, arXiv:hep-ph/0012274 [hep-ph].

[137] D. B. Kaplan and A. E. Nelson, "Strange Goings on in Dense Nucleonic Matter," *Phys. Lett.* **B175** (1986) 57–63.

[138] J. A. Pons, S. Reddy, P. J. Ellis, M. Prakash, and J. M. Lattimer, "Kaon condensation in proto neutron star matter," *Phys. Rev.* **C62** (2000) 035803, arXiv:nucl-th/0003008 [nucl-th].

[139] M. Stuke, D. J. Schwarz, and G. Starkman, "WIMP abundance and lepton (flavour) asymmetry," *JCAP* **1203** (2012) 040, arXiv:1111.3954 [astro-ph.CO].

[140] C. Domb and M. F. Sykes, "On the Susceptibility of a Ferromagnetic Above the Curie Point," *Proceedings of The Royal Society A: Mathematical, Physical and Engineering Sciences* **240** (1957) 214–228.

[141] G. Mercer and A. Roberts, "A Centre Manifold Description of Contaminant Dispersion in Channels with Varying Flow Properties," *SIAM Journal on Applied Mathematics* **50** (1990) no. 6, 1547–1565.

[142] F. Karsch, B.-J. Schaefer, M. Wagner, and J. Wambach, "Towards finite density QCD with Taylor expansions," *Phys. Lett.* **B698** (2011) 256–264, arXiv:1009.5211 [hep-ph].

[143] S. Datta, R. V. Gavai, and S. Gupta, "Quark number susceptibilities and equation of state at finite chemical potential in staggered QCD with Nt=8," *Phys. Rev.* **D95** (2017) no. 5, 054512, arXiv:1612.06673 [hep-lat].

[144] Z. Fodor, M. Giordano, J. N. Guenther, K. Kapas, S. D. Katz, A. Pasztor, I. Portillo, C. Ratti, D. Sexty, and K. K. Szabo, "Searching for a CEP signal with lattice QCD simulations," in *27th International Conference on Ultrarelativistic Nucleus-Nucleus Collisions (Quark Matter 2018) Venice, Italy, May 14-19, 2018*. 2018. arXiv:1807.09862 [hep-lat].

[145] R. V. Gavai and S. Gupta, "QCD at finite chemical potential with six time slices," *Phys. Rev.* **D78** (2008) 114503, arXiv:0806.2233 [hep-lat].

[146] V. Vovchenko, J. Steinheimer, O. Philipsen, and H. Stoecker, "Cluster Expansion Model for QCD Baryon Number Fluctuations: No Phase Transition at $\mu_B/T < \pi$," *Phys. Rev.* **D97** (2018) no. 11, 114030, arXiv:1711.01261 [hep-ph].

[147] R. Bellwied, S. Borsanyi, Z. Fodor, J. Günther, S. D. Katz, C. Ratti, and K. K. Szabo, "The QCD phase diagram from analytic continuation," *Phys. Lett.* **B751** (2015) 559–564, arXiv:1507.07510 [hep-lat].

[148] M. D'Elia, G. Gagliardi, and F. Sanfilippo, "Higher order quark number fluctuations via imaginary chemical potentials in $N_f = 2 + 1$ QCD," *Phys. Rev.* **D95** (2017) no. 9, 094503, arXiv:1611.08285 [hep-lat].

[149] C. Bonati, M. D'Elia, F. Negro, F. Sanfilippo, and K. Zambello, "Curvature of the pseudocritical line in QCD: Taylor expansion matches analytic continuation," *Phys. Rev.* **D98** (2018) no. 5, 054510, arXiv:1805.02960 [hep-lat].

[150] Z. Fodor and S. D. Katz, "Critical point of QCD at finite T and mu, lattice results for physical quark masses," *JHEP* **04** (2004) 050, arXiv:hep-lat/0402006 [hep-lat].

[151] M. A. York and G. D. Moore, "Exploring the Phase Diagram with Taylor Series: Epic Voyage or Just Another Bad Trip," arXiv:1106.2535 [hep-lat].

[152] B. B. Brandt and G. Endrodi, "Reliability of Taylor expansions in QCD," arXiv:1810.11045 [hep-lat].

[153] V. Vovchenko, A. Pasztor, Z. Fodor, S. D. Katz, and H. Stoecker, "Repulsive

baryonic interactions and lattice QCD observables at imaginary chemical potential," *Phys. Lett.* **B775** (2017) 71–78, arXiv:1708.02852 [hep-ph].

[154] H. T. Elze, W. Greiner, and J. Rafelski, "The Relativistic Ideal Fermi Gas Revisited," *J. Phys.* **G6** (1980) L149–L153.

[155] M. Laine and M. Meyer, "Standard Model thermodynamics across the electroweak crossover," *JCAP* **1507** (2015) no. 07, 035, arXiv:1503.04935 [hep-ph].

[156] **HotQCD** Collaboration, A. Bazavov *et al.*, "Equation of state in (2+1)-flavor QCD," *Phys. Rev.* **D90** (2014) 094503, arXiv:1407.6387 [hep-lat].

Danksagung

Zuallererst möchte ich mich bei Prof. Dietrich Bödeker dafür bedanken, dass er mich erst bei der Bewerbung um ein Stipendium und dann während der letzten Jahre unterstützt hat. Danke für die Möglichkeit an so vielen interessanten Konferenzen und Schulen teilnehmen zu dürfen und für die interessanten Diskussionen.

Ich danke auch Prof. Dominik J. Schwarz für interessante Diskussionen und dafür, diese Arbeit zu begutachten.

Danke an Alex und Dennis für die netten Gespräche bei Kaffee und Wein. Nochmals Danke an Dennis fürs Korrekturlesen. Danke an meine Mittagsessens-Crew von E5 (und Patric) und alle lieben Menschen von D6/E6 für die tolle Zeit. Herzlichen Dank an Gudrun und Susi für die organisatorische Unterstützung. Ich bedanke mich auch beim Sonderforschungsbereich CRC-TR 211 'Strong-interaction matter under extreme conditions' für interessante Vorträge und Treffen.

Mille grazie a Giuseppe, Lorenzo und Isabel für die schöne gemeinsame Zeit im Büro. Ein ganz großer Dank nochmal an Isabel, für deine Unterstützung und fürs Korrekturlesen der Arbeit.

Danke meinen (Physiker und Nicht-Physiker) Freunden für eure Unterstützung und Ablenkungen.

Besonders großer Dank geht an meine Eltern, die mich immer mein Ding haben machen lassen und mich bei allem unterstützt haben. Ein Dank von Herzen geht an meinen Verlobten Arne. Für alles und noch mehr. Und insbesondere dafür, dass du mich in stressigen Zeiten ertragen hast!

Zum Schluss möchte ich mich herzlich bei der Studienstiftung des deutschen Volkes dafür bedanken, dass sie es mir finanziell ermöglicht hat, diese Promotion zu verfolgen und auch für das interessante ideelle Programm.

Declaration

I hereby affirm that this dissertation represents my own work and has not been previously submitted to any examination office. All resources used have been referenced.

Bielefeld, 21 December 2018

Die Wissenschaft ist eine wunderbare Sache, wenn man nicht seinen Lebensunterhalt damit verdienen muss.

— Albert Einstein